Physics from the Gamma-Ray Spectra of Blazars

HARRIS, JONATHAN,DANIEL

Physics from the Gamma-Ray Spectra of Blazars

Jonathan Daniel Harris

Abstract

Blazars are numerous and often bright sources of cosmic γ-rays with several hundred such objects currently detected in this regime. However, there are several outstanding issues surrounding them. For example, it is uncertain exactly where in the kiloparsec-scale blazar jet γ-rays are produced and what the physical mechanisms responsible for the emission are. This thesis is an investigation in the physics and astronomy that can be learnt from studying the γ-ray energy spectra of blazars. Two studies are presented analysing bright blazars with the *Fermi*-Large Area Telescope (LAT). From the smooth spectral curvature seen in many of the objects and the lack of sharp spectral breaks it is concluded that the emission region is likely beyond the radius of the broad line region of 0.1 pc. It is seen that nearby confusing objects can lead to apparent breaks being observed in the spectra. However, a light curve analysis is performed of the bright blazar 3C 454.3 and it is seen that spectral breaks do sometimes occur when the object is in high flux states. From the shift in the peak of the γ-ray emission it is concluded that the high flux states are caused by an increase in the Lorentz factor of the emission region or by changes in the population of electrons in the emission region, but the origin of the breaks remains unexplained. Finally, a study is presented examining the effect that hypothetical axions or axion-like particles (ALPs) would have on the spectra if these particles should exist. It is found that under the right conditions a sudden flux boost could appear in the spectrum at a few TeV. The chances of the future Cherenkov Telescope Array (CTA) detecting the effects of photon-ALP mixing in AGN spectra is considered through simulated observations. These effects potentially present themselves in the spectra two ways: firstly the aforementioned flux boost and secondly due to the fact that the existence of ALPs could mitigate the pair absorption that γ-rays undergo when they traverse intergalactic space. It is concluded that CTA will have good prospects of either detecting these effects or else, if no effect is seen, setting limits on the mass and coupling constant that ALPs could have.

Physics from the Gamma-Ray Spectra of Blazars

Jonathan Daniel Harris

A thesis submitted to the University of Durham in accordance with the regulations for admittance to the Degree of Doctor of Philosophy.

Department of Physics University of Durham September 2014

Contents

List of Figures

List of Tables

Declaration

The work described in this thesis was undertaken between 2010 and 2014 while the author was a research student under the supervision of Prof. Paula M. Chadwick and Dr. T. J. Lowry McComb and Dr. Michael K. Daniel in the Department of Physics at the University of Durham. This work has not been submitted for any other degree at the University of Durham or any other university.

Parts of this work have appeared in the following papers:

- Harris, Jonathan; Daniel, Michael K. and Chadwick, Paula M. "Identifying Breaks and Curvature in the Fermi Spectra of Bright Flat Spectrum Radio Quasars." The Astrophysical Journal 761, no. 1 (2012): 2.

- Harris, Jonathan; Chadwick, Paula M. and Daniel, Michael K. "An investigation into the spectral properties of bright Fermi blazars." Monthly Notices of the Royal Astronomical Society 441, no. 4 (2014): 3591-3599.

- Harris, Jonathan and Chadwick, Paula M. "Photon-axion mixing within the jets of Active Galactic Nuclei and prospects for detection." Journal of Cosmology and Astroparticle Physics, JCAP10(2014)018.

All figures were produced by the author, unless otherwise stated.

Acknowledgements

I owe thanks to a lot of people for help throughout my PhD, but there are a few people I would like to thank in particular. Firstly, my wife Jeni for her constant support for my study. Secondly, the people who supervised my work (principally Paula), proofread this thesis (Paula) and gave their help and advice and criticisms to earlier drafts (Paula again). I would also like to thank Nikki Peceur and Max Knötig for generally keeping me sane.

And finally I would like to thank the following people for their help when writing papers, either for their ideas or careful reading of early drafts: Chris Done, Juri Poutanen, Shangkari Balenderan, Thomas Armstrong, Emma Gardner, Jim Hinton, Richard White, and Jonathan Davis.

I never loved to imitate, but always to invent: this has been the case in all the sciences I have studied. Hence many of my errors.

Humphry Davy

Chapter 1

Introduction and an Overview of γ-Ray Astronomy

1.1 Introduction

Active galactic nuclei can launch powerful and luminous jets that extend several kiloparsecs outwards from the central, supermassive black hole. If one of these jets is aligned at such an angle that we, on the Earth, look almost directly down the jet, beaming effects can greatly increase the luminosity even further. It is these objects which we call 'blazars' and which are the central topic of study for this thesis. Within the jets, charged particles are accelerated to close to the speed of light, leading to radiation being emitted across the whole electromagnetic spectrum, including the γ-ray regime which is concentrated on in this work. Ground-based and space-based detectors have facilitated the study of blazars in the γ-ray regime for over half a century but fundamental concepts such as exactly how and where γ-ray emission occurs are still debated. This thesis is an effort to join and contribute to this debate by analysing the γ-ray spectra of these objects. Furthermore, the precise spectra of blazars in high energy (HE) γ-rays is needed to understand the spectra in very high energy (VHE) γ-rays where absorption effects in intergalatic space complicate observations. At these frequencies the photons have energies far higher than anything regularly produced on Earth and provide an important chance to understand new physics. One proposal is that hypothetical axion particles could alter the spectra of blazars at very high energies and the final part of this thesis examines the prospects for the next generation of ground-based γ-ray telescopes to detect these alterations.

The rest of this chapter provides a brief overview of the field of the field of γ-ray

astronomy and the related field of cosmic ray astronomy from a historical perspective. Past and present space-based and ground-based telescopes are reviewed along with the number and nature of γ-ray sources detected. Particular attention is given to the *Fermi*-Large Area Telescope (LAT) which provides much of the data for the original work of this thesis and it is seen that several hundred blazars have been detected by this instrument. Finally, a brief look ahead is given to the Cherenkov Telescope Array (CTA), which is a next-generation ground-based array currently in its preparatory phase.

In Chapter 2 modern instruments and how they work are discussed in more detail. Particular attention is given to the LAT which operates on the principle of tracking e^-/e^+ pairs created by incident HE γ-rays. The principles of analysing LAT data to detect and characterise sources are given here. Next a brief overview of Cherenkov radiation is given; Cherenkov radiation produced in the Earth's atmosphere is utilised by ground-based telescopes to detect cosmic γ-ray sources. In order to do so, modern telescopes rely on imaging the light pool of Cherenkov radiation produced, which is discussed here. Finally, a look is given to current leading ground-based telescopes: H.E.S.S., MAGIC and VERITAS as well as a look at the future CTA.

Chapter 3 covers the particle acceleration mechanisms and radiation mechanisms relevant to understanding the observations of AGN jets. Firstly, diffusive shock acceleration is covered as a proposed method of creating a power law spectrum of high energy particles in the jet. Next, the Thomson cross section of the electron is derived and this is then applied to understand inverse Compton scattering of low energy photons to γ-ray energies. After this the characteristics of cyclotron radiation are derived by treating electrons in a B-field as quantum harmonic oscilators. This is then generalised to the case of synchrotron radiation. Then π^0 decay is considered as means of producing γ-rays.

In Chapter 4 AGN are covered in more detail: what they are and what radiation they emit along with their different classifications and how these are related to the angle an object is viewed from. Focus is then turned to the γ-ray emission of AGN jets. We look at what we can say about the size and location of the γ-ray emission region and discuss the different possible emission mechanisms for γ-rays, broadly speaking leptonic models and hadronic models.

In Chapter 5 we introduce the extragalactic background light (EBL), which is the diffuse light present throughout the universe. Since γ-ray photons can be annihilated

through photon-photon absorption, the existence of the EBL means that the universe has an optical depth for γ-rays. Higher energy γ-rays suffer more absorption and so the spectra of distant objects become softened. As we see, there is some tension between existing models of the EBL and the hardness of observed AGN spectra, given the current understanding of emission mechanisms. As a solution to this, the hypothetical axion particle is introduced. One property of axions is that in a B-field they couple to photons. This means that potentially γ-rays emitted from a distant AGN could convert into axions and travel through the EBL unabsorbed before reconverting to γ-rays in the Milky Way's B-field. This has been proposed as one solution to the tension between AGN observations and EBL models.

Chapter 6 begins by introducing the Akaike Information Criterion (AIC) as a method of comparing models being used to fit data. Starting with the definition of information entropy, we derive the AIC and show how it can be used in astrophysical observations.

In Chapter 7 a research project into the spectral properties of bright LAT blazars is presented. 9 FSRQ type blazars are analysed for evidence of breaks and curvature in their spectra and a discussion is given on what the results tell us about the emission region of γ-rays in AGN jets.

In Chapter 8 a further research project is presented. In some ways it is an extension of the project presented in the preceding chapter and again examines a sample of blazars for evidence of breaks and curvature in the spectra. The sample of objects has been expanded to include more blazars of both FSRQ and BL Lac types. Since this project was carried out later, a new LAT instrument response function (IRF) is used and the effect using different IRFs has on the results is compared. The effect that nearby, confusing sources have on the identified spectral shapes is also investigated. Additionally, a light curve analysis is performed on the bright FSRQ type blazar 3C 454.3 and the results examined to see what they tell us about the emission mechanism in this object.

Finally, in Chapter 9, a third research project is presented. The effect that photon-axion mixing within AGN could have on the emitted spectrum is considered. Then simulated observations of 3 blazars with CTA are carried out and the prospects for CTA to detect the effects of axions in the spectra, or else to set limits on the axion parameter space, are calculated.

A brief summary and look forward is given at the end of the thesis.

1.2 Cosmic Rays and γ-Rays

Around the turn of the 20th century it was noted that if a piece of apparatus was electically charged, the charge would gradually leak away. This suggested that the air was being continuously ionised, setting up the conditions for charge leakage. Originally it was thought that the source of this ionisation was radiation from radium in the Earth's crust (59). However, although experiments performed up church towers and the Eiffel Tower determined that the rate of leakage dropped, the fall-off was not as sharp as had been predicted. This led to measurements being taken at even higher altitudes: firstly in balloon-borne experiments, starting with Albert Gockell who concluded in 1911 that the source of the ionisation was in part coming from outside the Earth's atmosphere (72). Further balloon-borne experiments were carried out by Victor Hess and culminated (in terms of altitude) with Werner Kölhorster whose flights reached $9\ \mathrm{km}$ (117). These initial experiments were followed by aeroplane-borne experiments (117) and expeditions in the Rocky Mountains (107) and by the 1930s Arthur Compton had instigated a worldwide and fairly systematic cosmic ray survey, including expeditions to a height of around $6\ \mathrm{km}$ in the Himalayan mountains and unmanned balloons sent as high as $27\ \mathrm{km}$ (35). The data collected from these experiments supported Gockell's conclusion that there was a source of ionisation outside the Earth's atmosphere.

At first, it was widely believed that this ionising source was electromagnetic radiation and these so called cosmic rays were placed at the high frequency end of the electromagnetic spectrum (51). However, in the late 1920s evidence from ionisation (cloud) chambers and coincidence detectors suggested that the vast majority of the ionisation was due to massive particles and not photons. This hypothesis found further support when it was realised that the varying intensity of cosmic rays with the Earth's latitude could be understood if they were charged particles deflecting in the Earth's magnetic field (52). Despite this the name 'cosmic ray' stuck and later it would shift to its modern definition: cosmic rays refer to massive particles while high energy cosmic photons are known by the same name as their Earthbound counterparts: γ-rays.

Cosmic rays are highly energetic ($E \gtrsim 1\ \mathrm{GeV}$) particles, primarily hydrogen nuclei, and are observed to have an energy spectrum that is reasonably well described by a power law (see Figure 1.1). This suggests that cosmic rays and high energy ($E \gtrsim 1\ \mathrm{MeV}$)

γ-rays may share common origins. γ-ray sources are usually seen to have power law energy spectra and, as we shall see later, this can arise from the upscattering of low energy photons by a population of charged particles with a power law spectrum. Despite some well-educated guesses, over 100 years after their discovery the origin of cosmic rays is still shrouded in uncertainty. In a large part, this is due to the fact that the majority of cosmic rays are charged particles (there is a small neutron flux (81) and of course a large flux of neutrinos (12) which only rarely interact) and so their paths are bent by B-fields, obscuring the direction of their origin. In fact, up to the very highest energies where there are very few events, the arrival directions of cosmic rays are seen to be completely isotropic. (The gyroradius of a charged particle in a B-field is proportional to its velocity, so at the very highest energies the amount of curvature the particle undergoes is very small.) On the other hand, since photons are not deflected by B-fields, γ-rays retain information on their origin when they are detected. In this way, γ-rays can give important insights into the objects and environments in which cosmic rays are produced.

The objects producing γ-rays are observed to be many and varied, but studying them presents unique challenges. The Earth's atmosphere is opaque to γ-rays since when the photon enters the atmosphere it will quickly interact with atmospheric particles to produce an e^-/e^+ pair, annihilating the γ-ray. As we shall see in the following chapter, if a γ-ray has a very high energy (VHE- see Table 1.1) the atmospheric particle shower it initiates can be detected on the ground from the Cherenkov radiation it produces. However, the development of this technology into a workable state was a slow and painful process and was hampered by the inability to distinguish γ-ray events from the much more numerous and isotropic cosmic ray initiated airshowers. It would not be until 1972 that the Whipple telescope detected the first γ-ray source in the form of the Crab Nebula. To this day, the Crab Nebula remains the one of the brightest and most important γ-ray sources.

The other strategy to detect γ-rays is to get above the Earth's atmosphere. The first satellite to detect radiation above $30\ \mathrm{MeV}$ was Explorer XI, launched in 1961. Unfortunately several technical problems reduced the scientific output of the mission, and only 31 cosmic γ-ray events were recorded. The next space-borne γ-ray telescope was aboard OSO-3, launched in 1967. This operated by detecting e^-/e^+ pairs produced by incident γ-rays, a technique which will be discussed in greater detail in the following chapter.

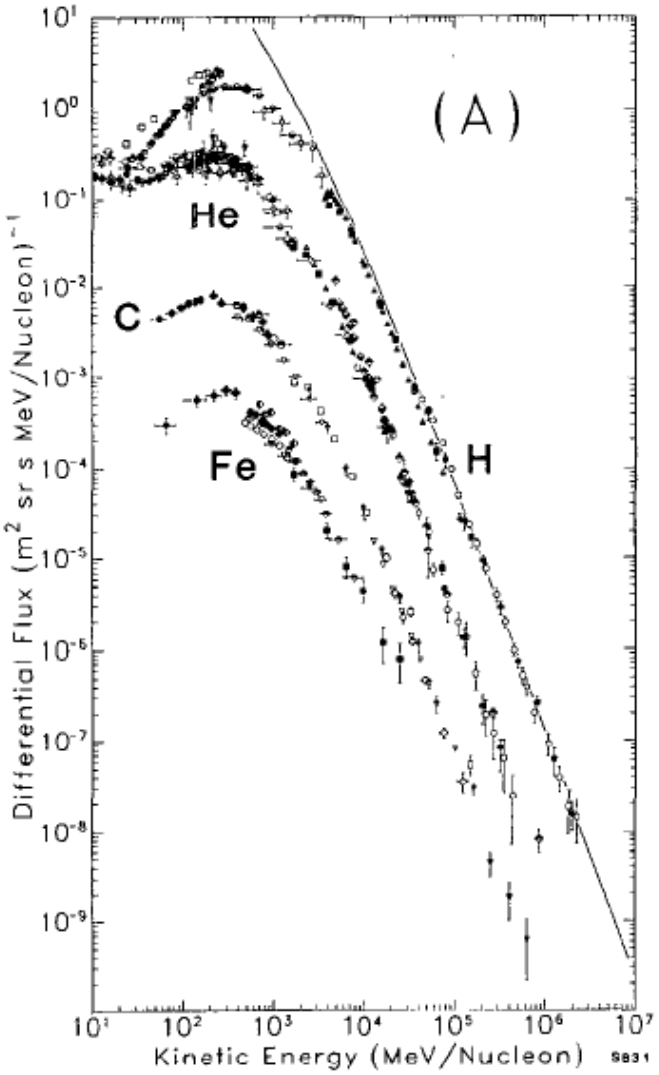

Figure 1.1: The composition and energy spectra of cosmic rays measured at Earth. The solid line shows the hydrogen spectrum extrapolated into interstellar space by removing solar effects. Not shown is the electron/positron component which is about 2% of the total particle flux. Image credit (140)

Table 1.1: Nomenclature for different energy bands.

Name [a]	Abbreviation	Energy Range	Notes
Low Energy	LE	< 20 MeV	Below the threshold for pair production.
High Energy	HE	20 MeV-500 GeV	Above threshold for pair production. Generally accessible to satellite detectors.
Very High Energy	VHE	500 GeV-100 TeV	Produces Cherenkov light in the atmosphere. Generally accessible to ground based telescopes.
Ultra High Energy	UHE	> 100 TeV	Higher than current γ-ray observations. Cosmic Rays are observed at these energies.

[a] This table is only approximate, and different authors use different definitions. These definitions will be used throughout this thesis.

This method, lacking any ability to focus the incoming radiation, has fairly poor angular resolution compared to other fields of astronomy. Still, OSO-3 was able to detect a significant γ-ray flux from the Milky Way. The next γ-ray satellite, SAS-2, was launched in 1972 and operational for 1 year. In that time it detected 3 point sources: the Crab pulsar and 2 other pulsars. In 1975 COS-B was launched and became the first γ-ray satellite to detect persistent extragalactic sources, including one source associated with the blazar 3C 273. COS-B's catalogue of 25 point sources was rapidly expanded on by EGRET, a detector aboard the Compton Gamma Ray Observatory which was launched in 1991 and operated between roughly 30 MeV and 20 GeV. The third EGRET catalog (75) contained 271 sources, including 93 sources associated with blazars. However, in a more recent analysis (46) which utilised an improved instrument response function and background models the number of sources was revised down to 188. Source association was not reanalysed in that work making the number of blazars detected by EGRET unclear. Currently orbiting satellites with γ-ray detectors onboard are *AGILE* (145), sensitive between ≈ 30 MeV and 50 GeV, and *INTEGRAL* (151), sensitive between the lower energy range of ≈ 0.1 MeV to 10 MeV (and both of these satellites also have hard X-ray detectors onboard).

The current state of the art in γ-ray satellites, the *Fermi* satellite, was launched in 2008. It carries on board 2 instruments. The first of these is the Gamma-ray Burst Monitor

(GBM) which views the whole sky and is sensitive between $\approx 8\ \mathrm{keV}$ to $40\ \mathrm{MeV}$ (104). As the name suggests, the GBM's primary purpose is to detect transient γ-ray bursts. The second instrument is a pair-production detector called the Large Area Telescope (LAT) which operates at roughly $30\ \mathrm{MeV}$ to $300\ \mathrm{GeV}$. As well as expanding on the energy range of earlier launched *AGILE*-GRID detector, the LAT offers improved source localisation and larger effective area (as can be seen by comparing reference (145) to the data given in the following chapter).

With rare exceptions, the LAT operates in sky scanning mode, repeatedly imaging the whole sky in roughly 3 hour cycles. An all sky image of LAT events is shown in Figure 1.2. Most striking is the diffuse emission from the Milky Way, produced mostly from the interactions of Galactic cosmic rays with nucleons and low energy photons (114). A diffuse background can also be seen, which is thought to be due to unresolved point sources such as AGN and star forming galaxies (3); despite the many advances pair production detectors have made over the decades the angular resolution is still a drawback and the LAT's 68% containment angle is as large as 3° at low energies. In 2012 the LAT 2 year point source catalog (2FGL) was published (114). AGN, which are of particular relevance to this thesis, are the most numerous class of object detected by the LAT, with 917 sources in the 2FGL associated with AGN, 894 of which are associated with blazars, the brightest of which are clearly visible in Figure 1.2. Only 7 non-active galaxies were detected using the LAT (including the Magellanic Clouds and M31). In terms of Galactic sources, only a handful of supernova remnants have firm detections in the 2FGL owing to their diffuse nature. Also detected are 11 globular clusters and 69 pulsar wind nebulae. Roughly 100 pulsars have been detected using the LAT, which are also published in a separate and more up to date catalog (7). At the end of 2013, a new pointing strategy was adopted which gave more coverage of the Galactic centre. This change was decided on in order to increase the instrument's sensitivity to young pulsars in the inner Galaxy, to compliment multiwavelength campaigns of the G2 gas cloud complex, and to improve sensitivity to any spectral lines from dark matter in the Galactic centre. (See (103) and the *Fermi* website http://fermi.gsfc.nasa.gov/ssc/proposals/alt_obs/obs_modes.html).

While this development of satellite detectors was happening, groud based Cherenkov telescopes also continued to evolve. The current methods will be discussed in more detail in the next chapter, but we shall summarise them here. There were 2 main advances

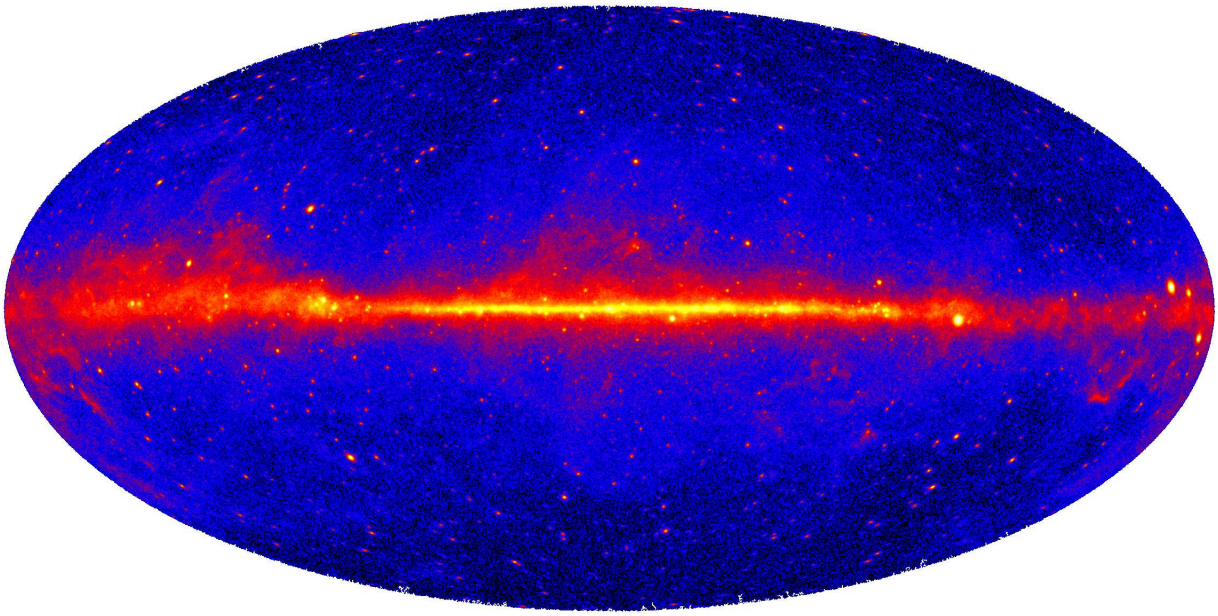

Figure 1.2: All sky map of five years of *Fermi* events above 1 GeV. Brighter colours indicate more events. The thick band of the Milky Way aross the middle is visible as is the Crab Nebular and several other pulsar wind nebulae close to the galactic plane and several blazars far removed from the Galactic plane. Image credit NASA/DOE/*Fermi* Lat Collaboration

in the technology to discuss, the first of which was imaging cameras. This allowed each airshower to be characterised in order to determine from its shape whether it was initiated by a γ-ray or a cosmic ray. This technology was first used with an upgrade to the Whipple telescope. Other early Cherenkov telescopes with imaging cameras were the Crimea telescope, which detected 3C 66a in 1997 (112) and later detected BL Lacertae for the first time at VHE (113), and the Durham telescope, which detected PKS 2155-304 in 1998 (48).

The second was the development of stereoscopic arrays of more than 1 telescope which allowed the position of the air shower in the sky, and therefore the γ-ray's point of impact, to be more precisely determined. This technology was first used on the HEGRA telescopes which detected, among other objects, M87 (20) and the supernova remnant Cassiopeia A (19).

Combining these 2 technologies to create Imaging Atmospheric Cherenkov Telescopes (IACT) arrays offers several complementary advantages compared to satellite-

based detectors. Due to the nature of the air showers they detect, IACTs have a higher energy sensitivty threshold and typically operate at $100\ \mathrm{GeV}$-TeV energies, as opposed to the MeV-$100\ \mathrm{GeV}$ energies of satellite detectors. IACTs also have a far larger effective area and better angular resolution.

Currently, the field is dominated by 3 arrays of telescopes. In the northern hemisphere there is VERITAS, a 4 telescope system operating in the U.S.A., and MAGIC, a 2 telescope system operating on La Palma. In the southern hemisphere is H.E.S.S. operating in Namibia which recently added a fifth telescope of particularly large collecting area to the array, lowering its energy threshold to $50\ \mathrm{GeV}$ (91). As of the 28^{th} of June 2014, there are 149 published TeV sources in TeVCat[1], 54 of which are blazars. There is some overlap between objects detected with ground-based instruments and objects detected with space-based instruments, especially among the very brightest sources (e.g. the Crab pulsar wind nebula, and the blazars PKS 2155-304 and 3C 279). However, due to the difference in energy ranges, objects that are detected by ground based instruments are usually not detected, or detected only weakly, by space based instruments and vice versa.

Presently finishing its preparatory phase is the next generation IACT, the Cherenkov Telescope Array (CTA). This will actually consist of 2 arrays, a smaller one in the northen hermisphere and a larger one in the southern hemisphere where the galactic plane is visible. The southern array will consist of around 60 telescopes and have a sensitivy from a few tens of GeV to over $100\ \mathrm{TeV}$ (11). The sensitivty of CTA, in various proposed layouts, has been extensively characterised through Monte Carlo simulations. CTA will be discussed more extensively in the following chapter.

[1] http://tevcat.uchicago.edu/

Chapter 2

Observational Techniques and Instruments

2.1 Introduction

In this chapter I will explain the observational techniques of modern space-based and ground-based γ-ray astronomy and the physics underlying them. I will start by discussing the *Fermi*-LAT, which is a space-borne pair-production telescope used extensively for work in this thesis. Next, I will discuss how VHE γ-rays incident on the Earth's atmosphere can create a flash of Cherenkov light and how modern imaging atmospheric Cherenkov telescopes (IACTs) can use Cherenkov light to detect and localise γ-rays. Finally I will introduce the Cherenkov Telescope Array (CTA), which is a next generation IACT of particular relevance to this thesis.

2.2 The *Fermi*-Large Area Telescope

The LAT is the main instrument on board the *Fermi Gamma-Ray Space Telescope*, the other being the Gamma-ray Burst Monitor (GBM). The *AGILE*-GRID detector (145) and the old *Compton*-EGRET detector operate on the same principles as the LAT. A detailed description of the LAT can be found in (32) with important updates given in (14). A schematic of the instrument is shown in Figure 2.1.

Briefly, the instrument works in the following manner. When a γ-ray is incident upon the LAT it first travels through the plastic anti-coincidence shielding. This shielding allows photons through mostly unhindered but charged particles interact and produce a

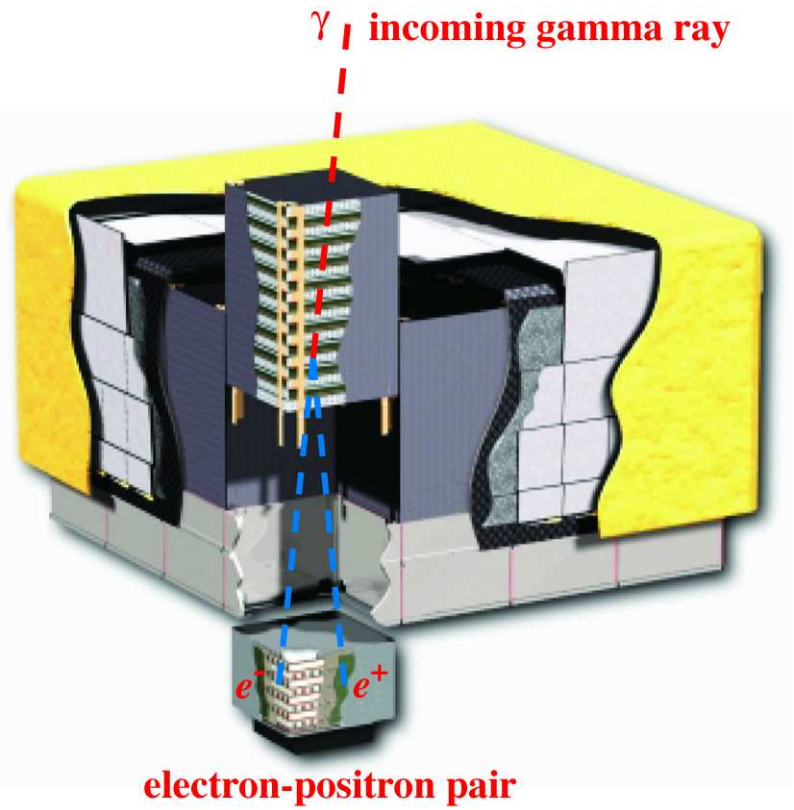

Figure 2.1: Schematic of the LAT. Image credit (32).

flash of light. In this way, the shielding provides the first means of discriminating γ-rays from the large background of cosmic rays. Inside the shielding, the detector consists of 16 towers containing alternating tungsten foils, which convert γ-rays to e^-/e^+ pairs, and silicon foils, to track these pairs. In the silicon strips the charged particles cause small ionisation currents that enable their paths to be tracked. Eventually, the charged particles are incident on a caesium iodide calorimeter at the base of the tower which measures the particles' energies. The effective area of the instrument is energy dependent, as shown in Figure 2.2, and is 0.8-0.9 m^2 between 1 GeV and 100 GeV.

From examining the particle tracks in the silicon detectors and by measuring their energies, the original γ-ray's energy and angle of incidence can be reconstructed through comparison with Monte Carlo simulations of events. Comparison to simulated events also allows the LAT to discriminate between γ-ray events and cosmic ray events, which give rise to characteristically different tracks. The instrument's point spread function (psf) is dependent on the energy of the γ-ray and is shown in Figure 2.3. As can be seen,

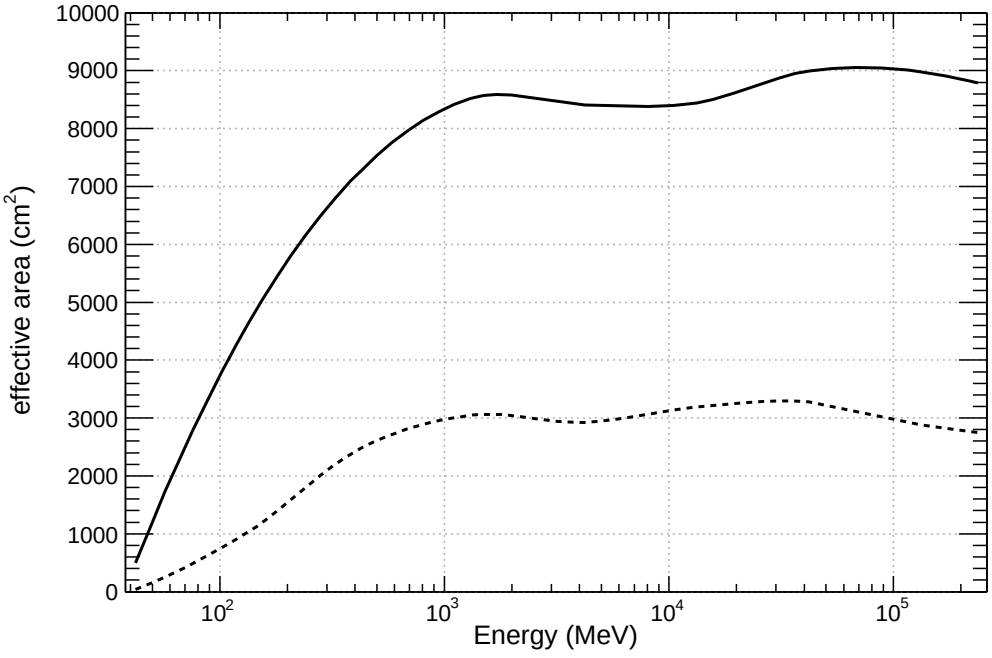

Figure 2.2: Effective area of the LAT at normal incidence (solid curve) and 60° off-axis (dashed curve). Image credit (32).

the psf is $< 0.1^\circ$ for events with energy above 10 GeV but is $\approx 3^\circ$ for events with energy of 100 MeV. This means that the LAT's ability to localise the position of a source is a function of the source's spectral index as shown in Figure 2.4. It can be seen that the localisation after 1 year's survey is typically around 0.01°. For this reason, LAT sources can be localised to far better precision if they can be identified or associated with known sources at other wavebands. This is typically done by matching variations in the flux seen by the LAT with those seen in one or more other wavebands (114).

The LAT's capability to detect an incident photon with a given set of properties (energy, incident angle, etc.) is known as the instrument response function (IRF) and defines the detector's characteristics such as its effective area and psf. 2 different IRFs were used in the original work of this thesis, known as Pass6 and Pass7. The newer Pass7 IRF was updated to take into account information collected during inflight operation. The differences between this and Pass6, described in reference (14), are quantitative rather than qualatitive, for example the effective area as a function of energy is changed. These differences can have a large impact on data analysis, as we shall see in Chapter 8.

With rare exceptions, the LAT operates in sky scanning mode, and its sky coverage

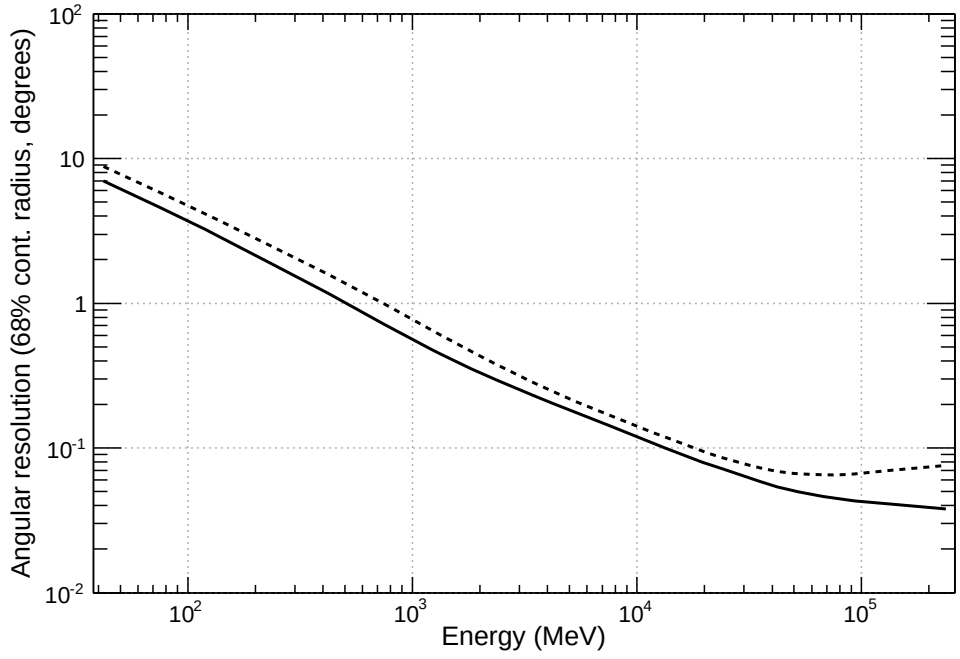

Figure 2.3: The point spread function of the LAT. The y-axis shows the 68% confidence containment radius for an event at normal incidence (solid curve) and 60° off-axis (dashed curve). Image credit (32).

as a function of time is shown in Figure 2.5. This mode of operation makes the LAT an excellent tool to monitor the variability of sources.

2.3 Data reduction for the LAT

2.3.1 Likelihood Analysis

In this section we will go through the standard analysis of a *Fermi*-LAT point source. We are assuming that we have identified a target source and wish to know if it is a γ-ray emitter and, if so, what its spectrum looks like. Similar analyses can be performed for a blind search where a target has not been identified, see e.g. reference (2).

All of the event data recorded by the LAT are available for public use [1]. The first step in data reduction is to specify a region of interest (ROI) on the sky. Because the psf is large, a fairly sizable ROI is usually required, typically $\approx 10^\circ$ around the target object,

[1] http://fermi.gsfc.nasa.gov/ssc/data/

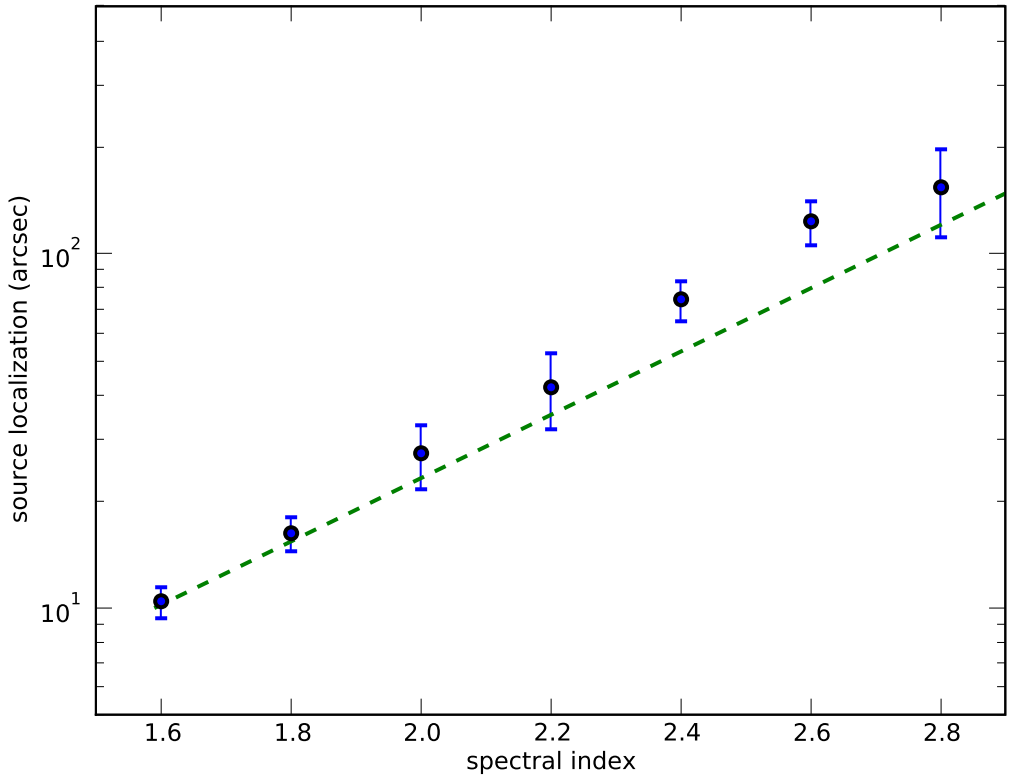

Figure 2.4: The 68% confidence on source localisation radius in a one year survey for a source with an integral flux of 10^{-7} ph cm^{-2} s^{-1} above 100 MeV. Image credit (32).

and known sources within or just outside the ROI will be included in the eventual model fitting. Time and energy cuts are also applied to the events, depending on the job at hand. Time intervals when the instrument's zenith angle is $\lesssim 100^\circ$ are not used, to avoid γ-ray contamination from the Earth. Each event is given an 'event class' depending on how cleanly the event was reconstructed in the detector. The minimum event class to be included in the analysis is also specified at this point. Specifying a higher event class usually increases the signal to noise ratio but obviously reduces the amount of data overall. At this stage, if the source of interest is thought to be sufficiently bright, the data can be placed into energy bins to speed up the analysis. Doing so will increase the speed of the analysis but information is lost in the binning.

Now that the time intervals of interest have been specified, the spacecraft's pointing direction over this period is reconstructed. Given this pointing history, and knowing the

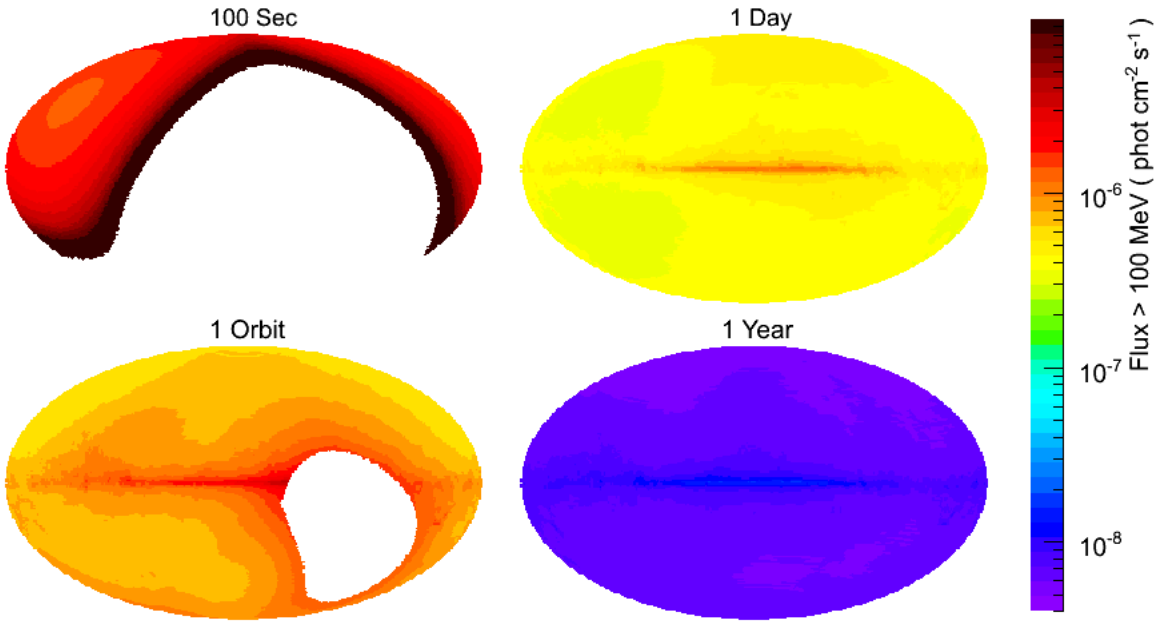

Figure 2.5: The LAT's sky coverage. Each map shows the sensitivity for exposures of various timescales in an Aitoff projection of Galactic coordinates. Image credit (32).

IRF, the exposure of each point on the sky is then calculated.

At this point a model can be fitted to the data. Diffuse models are published for the isotropic background, the Milky Way [2] and a handful of known diffuse sources [3]. Known point sources are modelled as phenomenological spectral shapes (e.g. a power law or a power law with an exponential cut off) and parameters can be fixed to previously published values or left as free parameters, depending on how bright the source is and how close it is to the target source. Similarly, a phenomenological spectral shape is chosen for the target and generally the parameters are left free. The model is then fitted to find values for the free parameters which maximise the likelihood of the data coming from the model. This is done by comparing the predicted detected number of photons that the model produces at each point in the sky as a function of energy to the observed number of photons. A variety of minimisation routines are provided in the *Fermi* analysis software and NEWMINUIT [4] is used for the work in this thesis. An example of a

[2] http://fermi.gsfc.nasa.gov/ssc/data/access/lat/BackgroundModels.html

[3] Included in the 2FGL.

[4] An implementation of MINUIT:

http://lcgapp.cern.ch/project/cls/work-packages/mathlibs/minuit/home.html

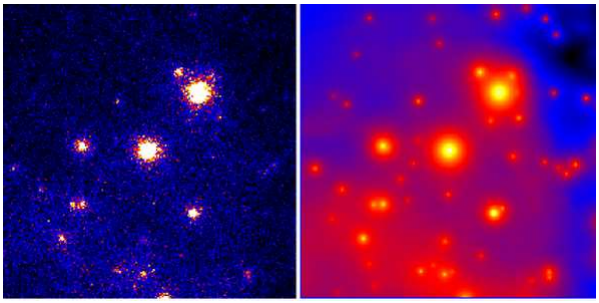

Figure 2.6: The LAT view of the region around blazar 3C 279. Brightness indicates the photon counts recorded by the LAT (left) and the photon counts from a model (right). This image is from the *Fermi* website's binned likelihood tutorial http://fermi.gsfc.nasa.gov/ssc/data/analysis/scitools/binned_ likelihood_ tutorial.html.

model prediction and actual data for the region around the blazar 3C 279 is shown in Figure 2.6.

Each source included in the model has a test statistic (TS). This is defined from the ratio of the log-likelihood of a model without including the source (L_0, the log-likelihood of a null-hypothesis) with the log-likelihood of the model with the source included (L_1):

$$TS = -2 \ln \frac{L_0}{L_1}. \tag{2.1}$$

This expression is the likelihood ratio test statistic, which is asymptotically χ^2 distributed. The TS value of a source in a model is useful in determining if a source has been significantly detected above the background with $\sigma \approx \sqrt{TS}$.

The result of such an analysis is that the significance of the target source has been determined along with the best fit values of the spectral parameters. The analysis could be re-run with a different spectral shape assumed for the target. The likelihood of the two models could then be compared to determine which, if either, is a better description of the data. This sort of model comparison will be discussed more extensively in Chapter 6.

2.3.2 Simulated Observations

In doing the research for this thesis, it was necessary several times to perform simulated LAT observations in order to validate analysis techniques. These simulations were done with the standard tool *gtobssim*, which enacts Monte Carlo simulations of the LAT. This

section describes how *gtobssim* functions.

gtobssim requires 2 inputs. The first is a model of the target source or sources along with any nearby sources which might be expected to have an effect on the analysis. This model contains the celestial coordinates for each source and defines a spectrum for each source. The second requirement is a pointing history for the spacecraft, i.e. the position and orientation of the LAT at each instant. This can either be a file that details the LAT's actual pointing history over a period of time or it can be a simulated pointing history. Given that the LAT has so far spent almost all of its time in survey mode, the exact pointing history used is normally not too important for observations longer than about a day.

When *gtobssim* is started, it creates a sphere around the LAT, representing the celestial sphere, and places the sources from the model file at the relevant points. The program then 'polls' each source to determine, based on the spectra in the model file, when the next photon will be emitted, which source emits it, and what the photon's energy is. The LAT's position and orientation at that moment is then determined. Whether the LAT detects the emitted photon, and if so the energy and location that the LAT determines the photon to have, is based on the LAT's calculated effective area, psf, and energy resolution. (A more thorough simulation tool called *gleam* is available, where each photon event is propagated through the detector.) After this, the sources are polled for the next photon and the cycle is repeated until a specified end time is reached.

At the end of this simulation is a list of events in the same format as actual LAT data. These events can then be analysed in the usual fashion, described in the previous subsection. The benefit of course is that the source parameters returned from the analysis can be compared to the input parameters to evaluate how accurate and precise the analysis is.

2.3.3 Aperture Photometry

Instead of performing an analysis on a large ROI, it is possible to peform a spectral analysis using a very small ROI around an object, typically 1°, in a procedure called aperture photometry. The flux in several energy bins is calculated directly by taking the number of photons within the ROI and correcting for the exposure of each bin taking the IRF into account. By using a small ROI it is assumed that the signal-to-noise will

be kept sufficiently high that the contribution from the background can be neglected. Alternatively, the photon counts from background regions can be subtracted from each energy bin before the exposure correction.

Although simple to do, this technique has the drawback that it does not take into account photons from the target source that are reconstructed to fall outside the small ROI or photons from a confusing source that do fall within the ROI. This is a particular problem at lower energies where, as we saw, the point spread function is quite large, often several degrees. Additionally, the background from diffuse sources will not be well-modelled in this approach. Because of these problems, it is not advisable to use aperture photometry to determine the spectra of sources. However, it can be a useful tool to provide illustrations of spectral fits determined from a full likelihood analysis, and the spectrum of 3C 454.3 is given as an example of this in Figure 2.7. Note that as the energy increases the flux becomes successively lower and no flux is recorded above $\approx 30\ \mathrm{GeV}$, despite 3C 454.3 being a very bright source and of average spectral hardness. The low number of photons detected is expected given that, as we saw earlier in the chapter, the LAT's effective area is $\approx 0.9\ \mathrm{m}^2$ at these energies. Above these energies, ground-based telescopes with a much larger effective area can be employed which operate by detecting of flashes of Cherenkov radiation.

2.4 Cherenkov Radiation and Extensive Air Showers

Ground based γ-ray telescopes are sensitive to higher energies than are accessible to the LAT and other space-based detectors. They operate by detecting flashes of Cherenkov radiation created when a VHE γ-ray enters the atmosphere. This section will outline the physics of how this Cherenkov radiation, or Cherenkov light, is produced.

When a γ-ray enters the atmosphere it quickly interacts with a massive particle in the atmosphere via the exchange of a virtual photon. This creates an e^-/e^+ pair, annihilating the γ-ray in the process. This initial pair of secondary particles produces a cascade of further particles: the leptons emit photons via bremsstrahlung and these photons can create further e^-/e^+ pairs. These processes repeat until enough energy has been lost that the photons can no longer pair create. (In fact at a few GeV it becomes likely they will ionise atoms rather than create new lepton pairs.) A schematic of such a shower

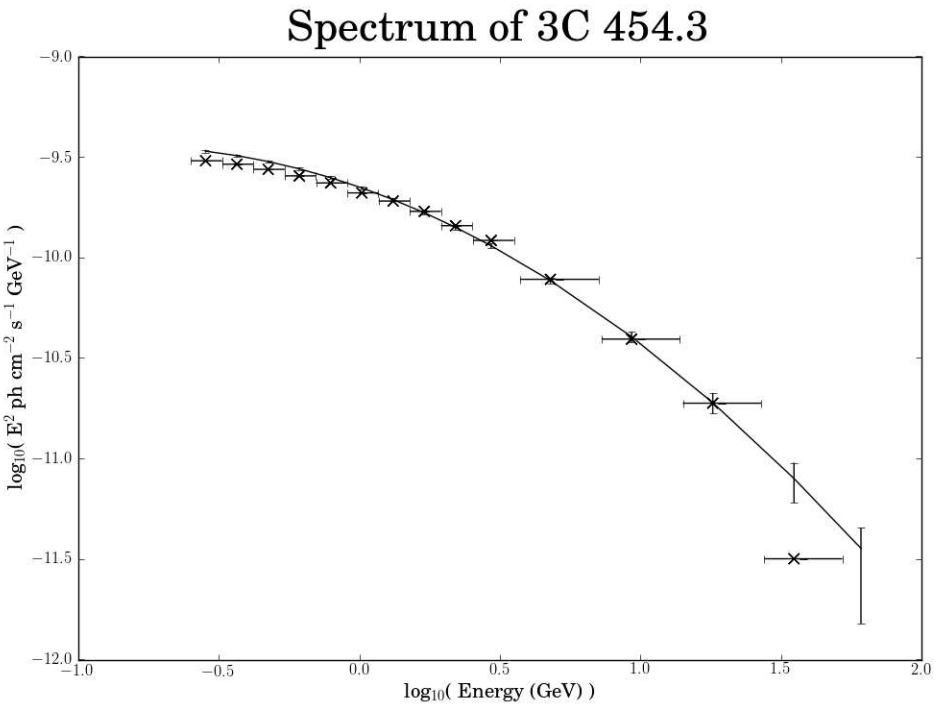

Figure 2.7: The best fit log-parabola model to the *Fermi*-LAT data 3C 454.3 and aperture photometry data points.

is shown in Figure 2.8. This multitude of particles created by the impact of the γ-ray is called an extensive air shower. Hadronic cosmic rays that enter the atmosphere also initiate extensive air showers through their interaction with atmospheric particles, and distinguishing γ-ray events above this hadronic background has been a major challenge to ground based γ-ray astronomy (see the next subsection).

When the initial particle strikes the atmopshere from above, conservation of momentum dictates that the air shower particles will be travelling downwards with a great speed, potentially greater than the speed of light in the atmosphere. The atmosphere is a dielectric medium, and whenever a charged particle moves through it a dipole is induced in its vicinity, which is then relaxed once the particle is past. As with all moving charges, the relaxation of the atmospheric particles after the passage of a charged particles emits an electromagnetic wave. If the particle were slow moving, the relaxation of the atmospheric particles would individually produce an electromagnetic wave but these would intefere with each other destructively. On the other hand, if the charged

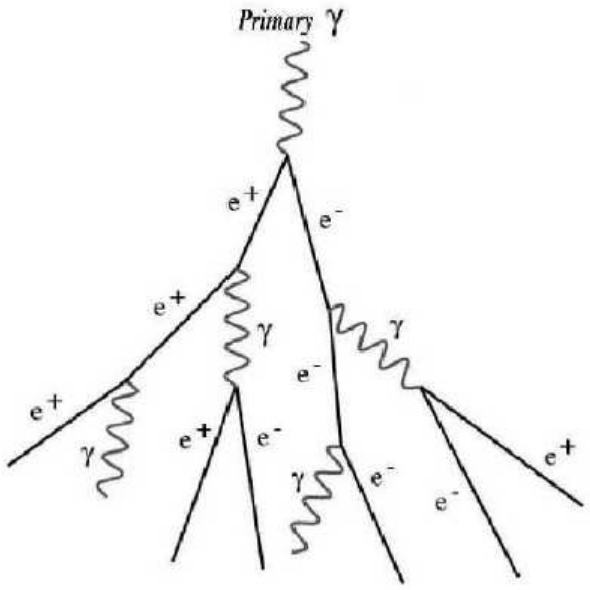

Figure 2.8: Schematic of the evolution of an air shower initiated by a VHE γ-ray incident on the atmosphere. The particles lose energy through pair production and bremsstrahlung. Image credit: Sam Nolan (118).

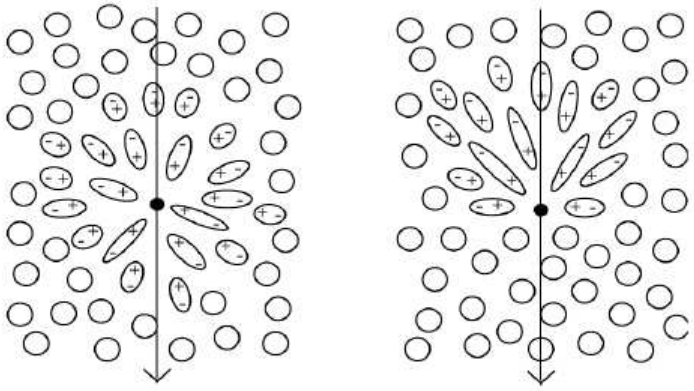

Figure 2.9: Dipole induced in particles in the atmosphere as a charged particle propagates along the direction of the arrow. Left: The charged particle is slow moving. Right: The particle is fast moving. Image credit: Sam Nolan (118).

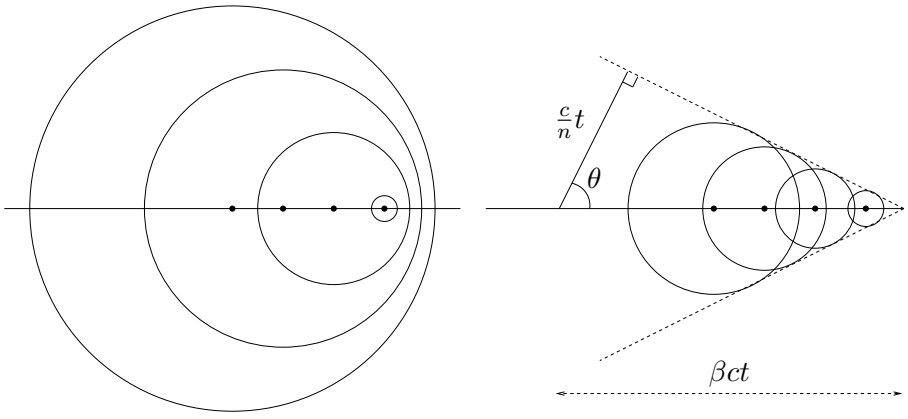

Figure 2.10: Left: For a slow moving particle, as each charged particle (solid dots) in the atmosphere relaxes it emits radiation in a sphere. These spheres interfere destructively. Right: For a fast moving particle, the radiation from each particle inteferes constructively along the dashed line. This radiation has an angle θ relative to the fast moving particle's propagation. Image credit: Jean-Philippe Lenain (95).

particle is travelling faster than the speed of light in the atmosphere, then the relaxation of the atmospheric particles happens in a coherent manner. This causes a wavefront of electromagnetic radiation to be produced in the wake of the fast-moving particle. This process is illustrated in Figure 2.9 and the geometry of the emitted wavefront is shown in Figure 2.10.

The light emitted in this way is called Cherenkov light after Pavel Cherenkov. The spectrum of the emitted light is described by the Frank-Tamm relation which gives the number of photons at a given frequency over at path of length dx travelled by a particle of charge q as (90):

$$\frac{dE}{d\nu} \approx \frac{q^2}{4\pi}\mu\nu\left(1 - \frac{c^2}{v^2 n^2}\right) dx, \tag{2.2}$$

where n is the index of refraction of the dielectric medium and μ is its permeability. It can be seen from this that most of the energy output is at higher frequencies ν. Since the atmosphere quickly becomes opaque at UV frequencies, in practice most of the Cherenkov light in the atmosphere is emitted in the visible blue regime.

Given the relativistic expression for kinetic energy,

$$E_K = \left(\frac{1}{\sqrt{1 - \frac{v^2}{c^2}}} - 1\right) mc^2, \tag{2.3}$$

and knowing that the electron rest mass is $m_e = \frac{511\ \mathrm{keV}}{c^2}$, we can quickly see that a γ-ray with initial energy of $E_\gamma > 20\ \mathrm{MeV}$ will produce particles that emit Cherenkov radiation. (However, as we will see in the next section, the threshold for Cherenkov telescopes is significantly higher since more than the bare minimum of Cherenkov radiation is required for a detection.)

Cherenkov emission is very faint. The emission from cosmic rays is only 10^{-4} of the night sky background and γ-rays are far outnumbered by cosmic rays. However, the particles constituting an extensive air shower collectively emit a relatively bright flash which lasts a couple of ns, the time taken for the air shower particles propagate to the ground. It is this flash of Cherenkov light which can be detected by Cherenkov telescopes (64). Over the ns timescale of a Cherenkov flash the night-sky background is relatively low, providing excellent signal to noise. The rapid response times required (as well as the small number of incident photons) means that Cherenkov telescope cameras utilise photomultiplier tubes for their pixels, since CCDs, which are more common in other areas of astronomy, would take too long in their readout time.

2.5 Imaging Atmospheric Cherenkov Telescopes

One of the main problems with which Cherenkov telescopes must contend is separating the γ-ray signal from the large background of hadronic cosmic rays. The air showers produced by γ-rays evolve in a characteristically different manner from air showers produced by hadrons. However, since there is no way to track the air shower particles directly as they propagate, all of the information must be gained from the shape of the Cherenkov light pool that reaches the ground. The evolution of air showers of different origins and their resulting light pools have been the subject of Monte Carlo simulations for several decades. Modern examples of a simulated γ-ray shower and a simulated hadron shower and their resulting light pools are shown in Figure 2.11. While the two light pools are evidently very different, in order to distinguish between them in real observations it is necessary to characterise the shape of the light pool and this of course means that the telescope camera must be capable of creating an image.

As shown in Figure 2.12, the light pool from an air shower falling onto a multi-pixel camera will form an ellipse. Once the light pool has been imaged, the ellipse can be

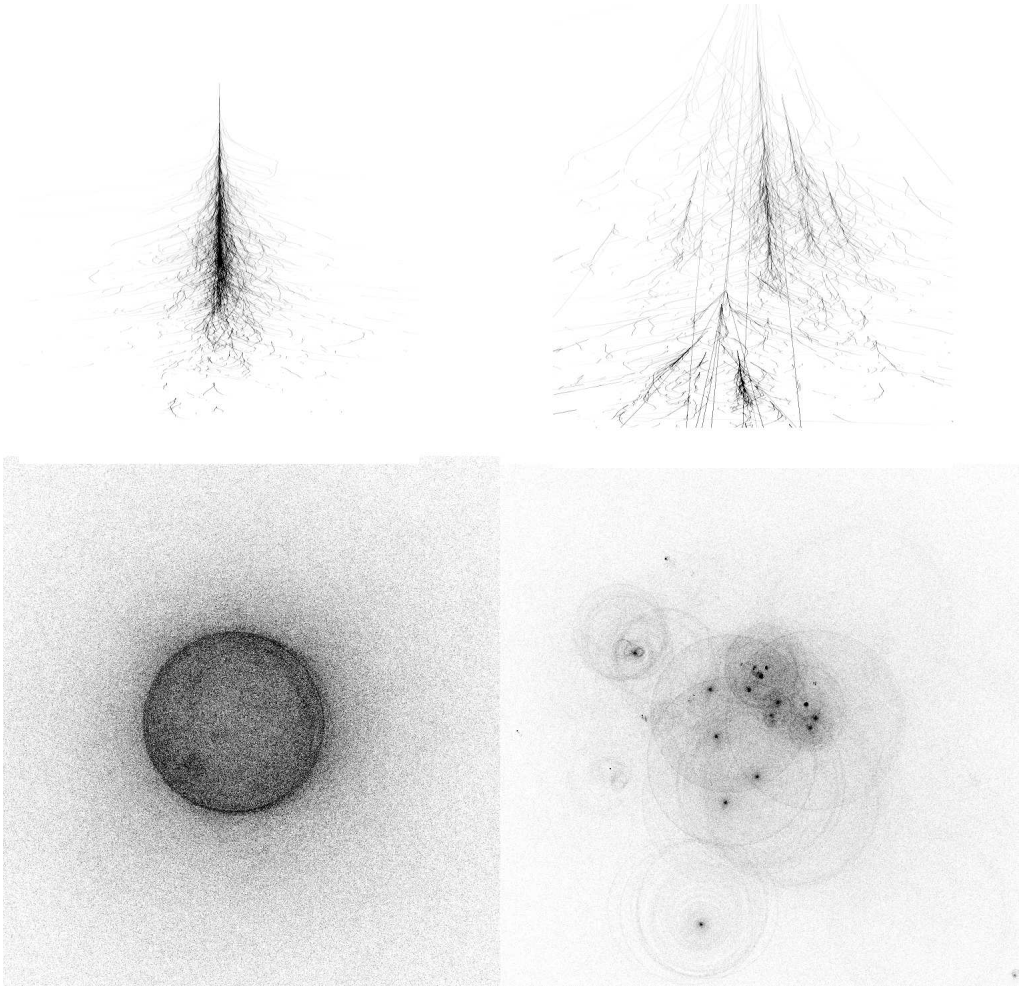

Figure 2.11: Cross section and top-down view of the Cherenkov light pool of $300\ \mathrm{GeV}$ photon (left) and a $1\ \mathrm{TeV}$ proton (right) to illustrate the difference between photon and hadron initiated showers. Image credit: Konrad Bernlöhr.

characterised based on its image moments such as its width, length and angle from the source's position in the camera. These characteristics are known as Hillas parameters and are shown in Figure 2.13. Since γ-ray showers and hadronic showers evolve differently through the atmosphere they have characteristically different distributions of Hillas parameters and these are well known from Monte Carlo simulations, the results of which have been compiled into look up tables. A shower image can be quickly classified as γ-ray or hadronic in origin by applying selection cuts on its Hillas parameters. Modern techniques now yield a background rejection rate of $> 99\%$ (60).

Stereoscopic observations utilising multiple telescopes improve γ/hadron separa-

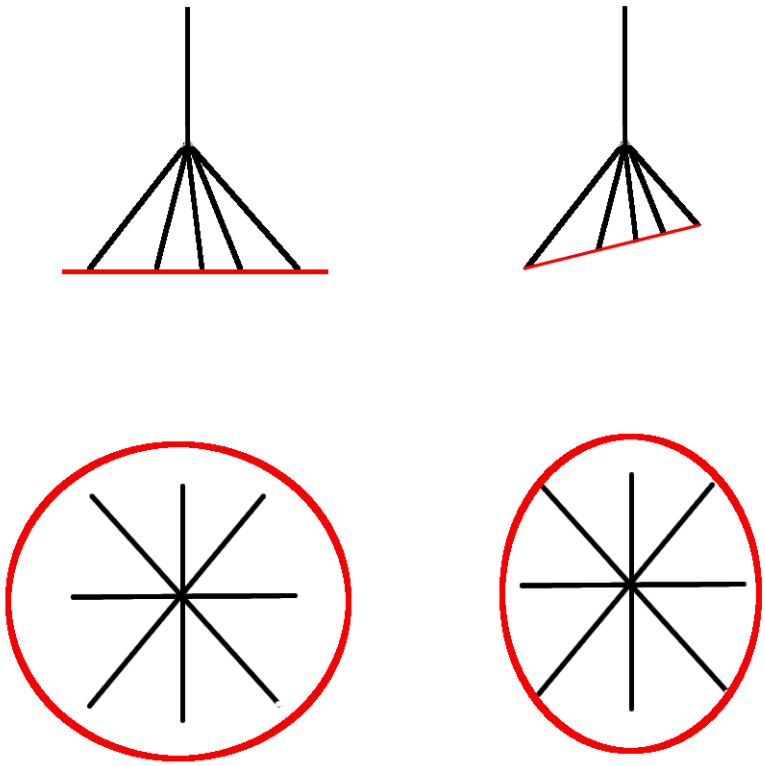

Figure 2.12: Schematical cross section and top-down view of a shower that shows how circular or elliptical images are seen in the camera plane depending upon the angle between the shower axis and the image axis. Photon paths of an air shower are shown in black and the outline of primary mirror (which is parallel to the image plane) is shown in red.

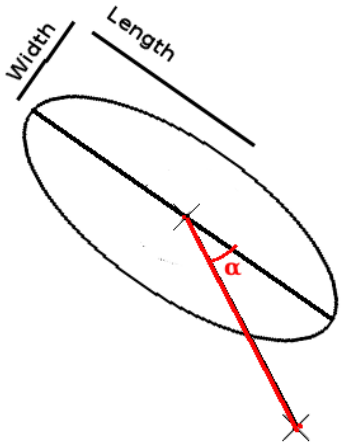

Figure 2.13: The moments that characterise a shower image in the camera. Width, length and angle α from the source's position in the camera image.

tion. This is done by defining quantities called the mean scaled width (MSCW) and mean scaled length (MSL). The MSCW is defined as (18):

$$MSCW = \frac{1}{N_{tel}} \sum_{i=1} \frac{\mathrm{width_i}}{< \mathrm{width_i} >}, \tag{2.4}$$

where N_{tel} is the number of telescopes that were triggered, $\mathrm{width_i}$ is the measured width in the i^{th} telescope and $< \mathrm{width_i} >$ is the expected width of a γ-ray event in the i^{th} telescope from the Monte Carlo look up table. The expected length and width of the image is dependent on the shower's energy. The MSCL can be similarly defined. An event is then rejected if the observed value of MSCW or MSCL differs from the expected value by more than a chosen amount.

Stereoscopic observations are also a boon to source localisation. The origin of the shower in the camera image will lie somewhere on the major axis of the ellipse. With 2 images of the same airshower in different cameras, the origin of the shower on the image can be placed where the major axes cross one another. In practice, it is usually desirable to have more than 2 telescopes for stereoscopic observations (24) which is why VERITAS and H.E.S.S. Phase I consist of 4 telescopes. (H.E.S.S. Phase II saw the addition of a fifth telescope, larger than the other 4, but this was done primarily to lower the energy threshld to ≈ 0.05 TeV (91) rather than to improve the spatial resolution.) The specifications of the current leading imaging atmospheric Cherenkov telescopes (IACT) arrays are shown in Table 2.1, typically they have angular resolutions for individual

Table 2.1: Specifications of existing IACT arrays.

Array	Number of Telescopes	Energy Range (approximate)	Energy Resolution	Primary Mirror Diameter	Altitude
H.E.S.S. I[a]	4	0.1-60 TeV	16% @ 0.4 TeV	12 m	1.8 km
VERITAS[b]	4	0.15-30 TeV	15% @ 1 TeV	12 m	1.3 km
MAGIC II[c]	2	0.06-20 TeV	14% @ 1 TeV	17 m	2.2 km

[a](22)
[b](78) and www.veritas.sao.arizona.edu
[c](50)

events on the order of 0.1° (78) (50), which compares very favourably to space-borne γ-ray telescopes, as we saw earlier in the chapter. Ground-based telescopes also yield an advantage over space-borne telescopes in terms of their effective areas. Firstly, very large and therefore sensitive telescopes can be constructed and, secondly, the Cherenkov light pool typically spreads over a diameter of $200\ \mathrm{m}$ and a telescope anywhere within this has a chance of detecting the flash. The effective area is usually calculated using Monte Carlo simulations. Many events are simulated over a large area and the effective area at a given energy is then calculated as the simulation area multiplied by the fraction of events which pass selection cuts, and are therefore deemed to be detected. IACTs typically have an effective area of $\approx 10^5\ \mathrm{m}^2$ at energies around $1\ \mathrm{TeV}$ (22) (compared to the typical LAT effective area which, as we saw earlier in the chapter, is around $0.8\ \mathrm{m}^2$).

2.6 Cherenkov Telescope Array

The next generation of IACT is called the Cherenkov Telescope array (CTA). It is currently finishing its preparatory phase, with scientific observations planned to start in 2016 and an in-depth description can be found in reference (11). It is expected to deliver improvements over existing IACTs in all key areas: an extra decade in energy coverage, a factor of 10 improvement in sensitivity, and a factor of 5 improvement in angular resolution ($\approx 2\ \mathrm{arcmin}$ above $1\ \mathrm{TeV}$).

At the very highest γ-ray energies, $\gtrsim 10\ \mathrm{TeV}$, the Cherenkov light pool is relatively bright and can be detected by a telescope with a relatively small mirror area, but these events are very rare. Therefore the best strategy for observing these events is to have many small telescopes ($\sim$ 4-7 m primary mirror diameter) spread across a wide physical

area. At energies $\lesssim 100\ \mathrm{GeV}$, events are relatively frequent but faint. Therefore the best strategy is to have a few large telescopes ($\sim 24\ \mathrm{m}$). In the core energy range, between these two extremes, a compromise is required in the form of medium size telescopes ($\sim 12\ \mathrm{m}$).

CTA will actually consist of 2 arrays, one in the northern hemisphere and a larger one in the southern hemisphere. Together they will provide all-sky coverage. The capabilities of these arrays with various proposed telescope layouts has been well characterised through extensive Monte Carlo simulations, details of which can be found in (36). The layout for the southern array is currently expected to resemble proposed layout E, which is shown in Figure 2.14. This comprises of 4 large size telescopes, 23 medium size telescopes, and 32 small size telescopes. In the northern hemisphere, where the Galactic plane is less visible, the array will focus on observing extragalactic objects where the high energy part of the array (large size telescopes) is not required, as at these energies the γ-rays will be mostly absorbed by annihilation with the extragalactic background light (EBL), as we will see in Chapter 5. Conversely, there is much science on Galactic objects that CTA can do at its highest energies, e.g. studying the emission mechaisms of supernova remnants (131), which favours including high energy telescopes in the southern array.

CTA is of great relevance to this thesis, as one of its primary science drivers is the study of AGN and the EBL, and original work for this thesis has included simulations of CTA observations. The other primary science drivers for CTA are studying dark matter (which could annihilate or decay into γ-rays), pulsar wind nebulae and supernova remnants, cosmic ray production sites in the Milky Way and other galaxies, and searching for Lorentz invariance violation in the arrival dispersion of γ-rays of different energies.

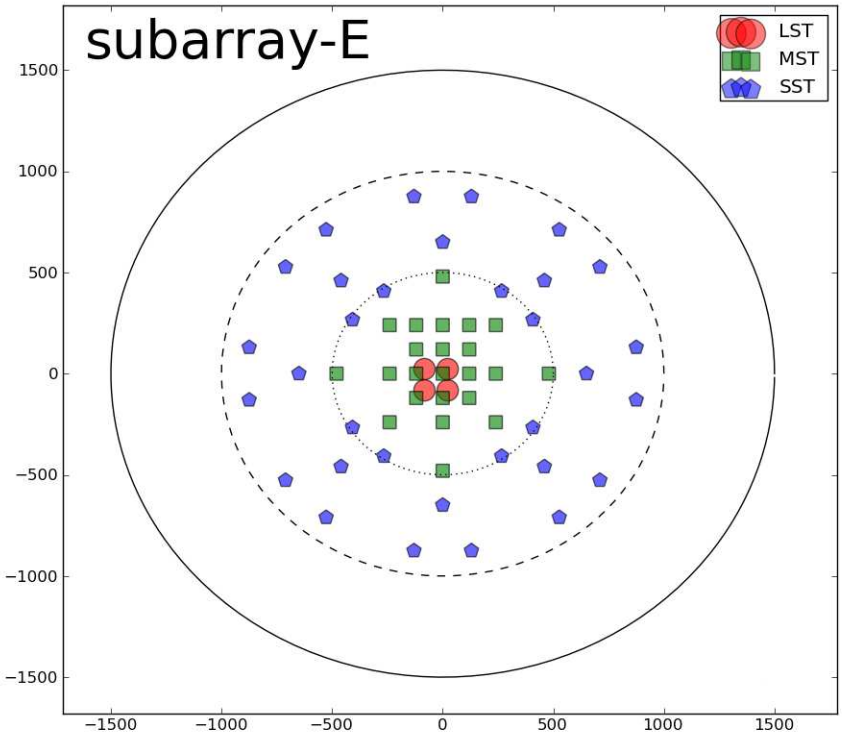

Figure 2.14: The proposed Subarray E for the CTA southern array. Scale in metres. Image credit: Thomas Armstrong.

Chapter 3

Particle Acceleration and Radiation Processes

3.1 Introduction

As we saw in the first chapter, a blazar is a class of AGN which has a jet closely aligned with the observer's line of sight. These objects are often bright in radio waves and γ-rays, with the emission from the jet thought to be dominant in these regimes. However, the exact processes by which blazars emit γ-rays are uncertain. In this chapter we shall briefly review the basic emission mechanisms for γ-rays that we will need for our later discussions, especially those discussions about the different emission models of blazars. At lower energies (radio through to X-ray), blazars are believed to emit synchrotron radiation: emission from fast moving charged particles within a B-field. The mechanism of γ-ray emission is less certain. Despite the high temperatures typical of blazar jets, a thermal origin from the γ-ray emission can be ruled out. High frequency peaked blazars (HBLs, see next chapter) are typically observed to have a peak in the γ-ray emission at around $1\ \mathrm{TeV} \approx 1.2 \times 10^{-16}\ \mathrm{cm}$ (125) and from Wien's law, if this emission were thermal, the emission region would require a temperature of around 2×10^{15} K, several orders of magnitude higher than the brightness temperaure of the region inferred from radio observations (97). (This is of course neglecting arguments as to how the material could maintain a Maxwellian distribution with such particle energies without cooling via other mechanisms such as the ones covered in this chapter.)

Several explanations exist for the γ-ray emission from blazars, which I will consider only briefly here since they will be discussed more thoroughly in the following chapter. One explanation is that high energy electrons and positrons in the jet inverse Compton scatter photons up to γ-ray energies. These low energy seed photons could be provided

by synchrotron emission from electrons and positrons in the jet, giving an especially good reason for examining this process in some detail, or could originate from outside of the jet. Alternatively, the γ-ray emission could be synchrotron emission of heavy, hadronic particles or the result of decaying π^0 particles.

All of these scenarios for γ-ray emission require the acceleration of particles to high energies and likewise this is required for the synchrotron emission seen at low energies. I will present here a scenario for accelerating particles in the jet, a class of Fermi acceleration called diffusive shock acceleration, which can produce particle spectra capable of explaining the observed emission. After this, I will cover in more detail the emission mechanisms introduced above: inverse Compton scattering, synchrotron radiation, and π^0 decay.

3.2 Diffusive shock acceleration

There are good reasons to believe that blazar jets contain shocks. Firstly, there is observational evidence for their existence, in the form of luminous knots in the jets (130). Secondly, jets are sources of sustained synchrotron emission but, as we will see presently, the observed power output of the jet dictates that the particles should rapidly cool and cease emission. Therefore, the particles need a constant source of acceleration. As shown by Anthony Bell (34), this acceleration can be provided by shock fronts. Bell's work demonstrated an acceleration mechanism that could occur in any shocked plasma, including AGN jets and other objects such as supernova remnants. This mechanism produces a distribution of particles with a spectral index of ≈ 2.5, which is in rough agreement with the observed indices of γ-ray sources, as we saw in Chapter 1, and with that of cosmic rays. In addition, the spatial isotropy of the cosmic ray spectrum in the sky requires a fairly universal mechanism for their production, which diffusive shocks could provide.

A schematic of Bell's work is shown in Figure 3.1. Bell started by considering what would happen to highly accelerated particles in the plasma which were able to overtake the shock. Since the particles were moving with respect to the plasma, they would lose energy by exciting Alfvén waves and constantly decelerate until they were at rest with respect to the plasma (154). This would mean that any particles that made it across the shock would be decelerating and therefore the shock would eventually overtake them.

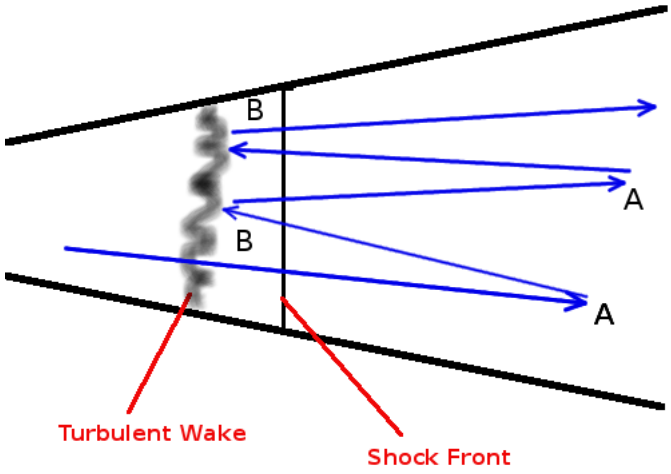

Figure 3.1: Schematic of diffusive shock acceleration. A shock front travels up the jet with a turbulent wake behind it. The movement of the shock front up the jet is negligible for the timescales discussed here. In blue is shown the track of a particle that initially over takes the shock front. At the points labelled 'A' the particle changes direction due to being decelerated by Alfvén waves. At the points labelled 'B' the particle changes direction due to being accelerated by the turbulent wake. The particle crosses and re-crosses the shock front many times before escaping.

The wake of the shock would be turbulent which would accelerate particles. The result is that particles would cross and recross the shock multiple times, caught between Alfvén waves on one side and the turbulent wake on the other. Bell showed that after multiple crossings, particles would on average gain energy from the shock (compared to their initial injection energy), resulting in a particle energy spectrum of

$$N(E) = \frac{v-1}{E_0}\left(\frac{E}{E_0}\right)^{-v}, \tag{3.1}$$

$$v = \frac{2v_2 + v_1}{v_1 - v_2} + \mathcal{O}\frac{v_1 - v_2}{c} \tag{3.2}$$

where E is energy, E_0 is the initial energy of the particles, v_1 and v_2 are the mean velocity of the particles upstream and downstream of the shock respectively (in the rest frame of the shock). Since $v_1 - v_2 \ll c$, the second term in Equation 3.2 is negligible.

Multiwavelength observations imply $v \approx 2.5$ (e.g. (122)), in rough agreement with the value of 2.5 required for the cosmic ray spectrum.

3.3 Derivation of the Thomson Cross Section

Two of the main emission mechanisms that are thought to be at work in blazar jets, synchroton emission and inverse Compton scattering, arise from the interaction of electrons with photons. The strength of this interaction is determined by the Thomson cross section, which can be treated as the classical cross section of the electron. We shall derive the Thomson cross section here, beginning by imagining a sinusoidal electromagnetic wave of the form

$$\underline{E}(t) = E_0 \sin(\omega_0 t)\underline{\hat{\epsilon}}, \tag{3.3}$$

incident upon a stationary electron of mass m_e. This causes the electron to scatter since the electromagnetic wave provides a force[1] (and therefore an acceleration $\underline{\dot{v}}$):

$$\underline{F} = m_e \underline{\dot{v}} = qE_0 \sin(\omega_0 t)\underline{\hat{\epsilon}}. \tag{3.4}$$

The information that the electron has moved is restricted to travelling at the speed of light. Therefore, after some amount of time, t, outside of a shell of radius $r = c \cdot t$ the electomagnetic field is unchanged, whereas inside the shell the field is shifted along with the electron, as shown in Figure 3.2. This assumes that the speed of the electron is non-relativistic and therefore sufficiently slow that the electromagnetic field within the shell can adapt to the electron's movement.

Let us assume that impact of the photon gives the initially stationary electron a change in velocity of dv. The electron's displacement at a given time is then $dv \cdot t$. Consider the E-field at an angle θ relative to the direction of the electron's movement. Whilst the E-field in the radial direction, E_r, is constant, the E-field orthogonal to this, E_θ, experiences a pulse as the shell passes over it during a time interval dt, as we see in Figure 3.3.

We now determine the strength of this pulse in the E_θ direction. We can see that,

$$E_\theta = dv \cdot t \cdot \sin\theta, \tag{3.5}$$

$$E_r = c \cdot dt, \tag{3.6}$$

[1]The Lorentz force, neglecting the much weaker magnetic component.

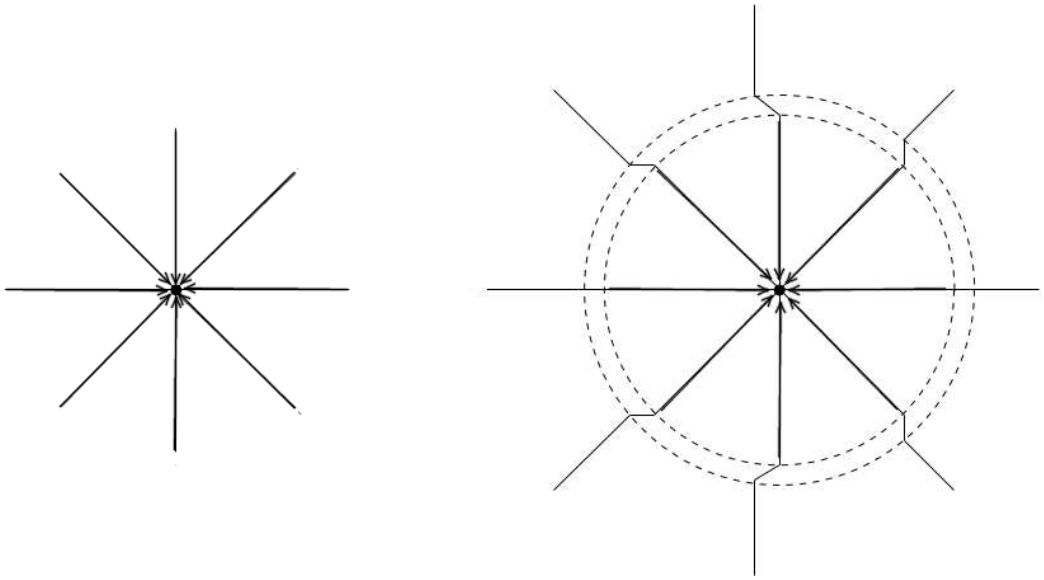

Figure 3.2: Left: The E-field around the electron before scattering. Right: The E-field around the electron after scattering, the dotted lines show the shell at radius $r = ct$. Image credit: Malcolm Longair via Jörn Wilms.

and therefore

$$\frac{E_\theta}{E_r} = \frac{dv \cdot t \cdot \sin\theta}{c \cdot dt}. \tag{3.7}$$

Additionally, from Coulomb's law we see that

$$E_r = \frac{q}{4\pi\epsilon_0}\frac{1}{r^2}. \tag{3.8}$$

Using this, as well as $r = c \cdot t$ and $\frac{dv}{dt} = \dot{v}$ we get,

$$E_\theta = \frac{q}{4\pi\epsilon_0 r c^2}\dot{v} \cdot \sin\theta. \tag{3.9}$$

Therefore, the Poynting flux of the pulse, the flow of energy per unit area per unit time, is

$$S = \frac{\epsilon_0 c}{2}E_\theta^2 = \frac{q^2}{32\pi^2 c^3 \epsilon_0 r^2}\dot{v}^2 \sin^2\theta. \tag{3.10}$$

The change in power directed through a given solid angle, $d\Omega$ is

$$dP(\theta) = Sr^2 d\Omega, \tag{3.11}$$

$$dP(\theta) = \frac{q^2}{32\pi^2 c^3 \epsilon_0}\dot{v}^2 \sin^2\theta d\Omega. \tag{3.12}$$

By integrating over solid angle, we find the total power emitted,

$$P = \int_{4\pi} \frac{q^2}{32\pi^2 c^3 \epsilon_0}\dot{v}^2 \sin^2\theta d\Omega. \tag{3.13}$$

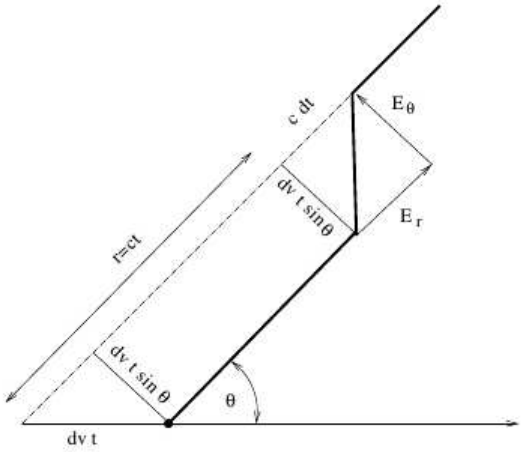

Figure 3.3: Geometry of the E-field around the shell at radius $r = ct$. Image credit: Malcolm Longair via Jörn Wilms.

$$P = \int_{2\pi}\int_{\pi} \frac{q^2}{32\pi^2 c^3 \epsilon_0}\dot{v}^2 \sin^3\theta d\theta d\phi. \tag{3.14}$$

$$P = \int_{2\pi} \frac{4}{3}\frac{q^2}{32\pi^2 c^3 \epsilon_0}\dot{v}^2 d\theta d\phi. \tag{3.15}$$

$$P = \frac{q^2}{12\pi c^3 \epsilon_0}\dot{v}^2. \tag{3.16}$$

Using first Equation 3.4 and then Equation 3.10 we find

$$P = \frac{q^4 E_0^2}{12\pi c^3 m_e^2 \epsilon_0} = \frac{q^4 S}{6\pi c^4 m_e \epsilon_0}. \tag{3.17}$$

If we consider the change in power in a given direction as the incident energy flux times the amount scattered into the angle,

$$dP(\theta) = S d\sigma(\theta), \tag{3.18}$$

then σ is the angle-dependent cross-section. The total power scattered through all angles is

$$P = S\sigma. \tag{3.19}$$

By setting this equal to Equation 3.17 we find the expression for the Thomson cross section:

$$\sigma_T = \frac{q^4}{6\pi c^4 \epsilon_0 m_e^2}. \tag{3.20}$$

3.4 Inverse Compton Scattering

In our above derivation of the Thomson cross section, we saw that an incident photon can impart energy to an electron. The reverse process, where an electron imparts energy to a photon, also happens, and is known as inverse Compton scattering. Inverse Compton scattering is an important process in high energy astronomy, since it is one of the main mechanisms for the production of γ-ray photons. For this process to happen, the electron must first be accelerated to very high energies, which in the case of AGN happens in shock fronts in the jet, as we saw in the previous section.

Let us consider a non-relativistic electron in a field of low energy photons. Given the previous discussion, it is straightforward to work out the amount of power the electron will impart to the photon field. By substituting the energy density of the field, U_{rad}, into Equation 3.19, we find the inverse Compton power is

$$P_c = \sigma_T c U_{rad}. \tag{3.21}$$

If we now consider the electron to be moving through the photon field at relativistic speeds, we need to consider the fact that the energy density in the rest frame of the electron will be different from the energy density in the observer frame (although the total power scattered is Lorentz invariant). Quantities in the electron's rest frame are denoted with a prime,

$$P_c = \sigma_T c U'_{rad}. \tag{3.22}$$

To convert the energy density into the primed frame, we need to consider that both the photon density N and the photon frequency ν will change:

$$U'_{rad} = N' h\nu' = N\left(\gamma(1+\beta\cos\theta)\right) h\nu \left(\gamma(1+\beta\cos\theta)\right) = U_{rad}\left(\gamma(1+\beta\cos\theta)\right)^2. \tag{3.23}$$

As we can see, the expression for U'_{rad} depends upon the angle θ between the electron and any given photon. If we assume that U_{rad} is isotropic in the observer frame, we can recover the expression in the electron's frame by integrating over all angles:

$$U'_{rad} = \int_{2\pi}\int_{\pi} U_{rad}\left(\gamma(1+\beta\cos\theta)\right)^2 \sin\theta d\theta d\phi, \tag{3.24}$$

$$U'_{rad} = \frac{4}{3} U_{rad}\left(\gamma^2 - \frac{1}{4}\right). \tag{3.25}$$

We can substitute this into Equation 3.22 to get the amount of power from inverse Compton scattering:

$$P_c = \frac{4}{3}\sigma_T c U_{rad}\left(\gamma^2 - \frac{1}{4}\right), \tag{3.26}$$

It is customary to subtract from this Equation 3.21, the power scattered by a stationary electron in the radiation field, to find the net power gain from inverse Compton scattering:

$$P_c = \frac{4}{3}\sigma_T c \beta^2 \gamma^2 U_{rad}. \tag{3.27}$$

Now that we have an expression for the power a single electron produces through inverse Compton scattering, we can go on to derive the characteristic frequency at which this power is radiated, i.e. the characteristic frequency of photons after being scattered. The total photon scattering rate is (38)

$$\frac{dN}{dt} = \sigma_T c n, \tag{3.28}$$

where n is the photon number density. Since

$$P_c = E_C \frac{dN}{dt}, \tag{3.29}$$

where E_C is the average energy of a photon after scattering, when $\beta \approx 1$ it follows from Equation 3.27 that

$$E_c = \frac{4}{3}\gamma^2 \frac{U_{rad}}{n} = \frac{4}{3}\gamma^2 E_0, \tag{3.30}$$

where E_0 is the average energy of a photon before scattering. Equivalently, in terms of frequency,

$$\nu_c = \frac{4}{3}\gamma^2 \nu_0, \tag{3.31}$$

from which we can determine the following expressions, which we shall use later:

$$\gamma = \left(\frac{3}{4}\frac{\nu_c}{\nu_0}\right)^{\frac{1}{2}}, \tag{3.32}$$

and

$$\frac{d\gamma}{d\nu_c} = \frac{\nu_c^{-\frac{1}{2}}}{2}\left(\frac{3}{4\nu_0}\right)^{\frac{1}{2}}. \tag{3.33}$$

We are now in a position to determine the spectrum radiated by the inverse Compton scattering of multiple electrons in a monochromatic radiation field. We shall look at the

case of a population of electrons that have a power law distribution in Lorentz factor, or equivalently in their energy:

$$N_e = K\gamma^{-p}. \tag{3.34}$$

The emissivity (the power per unit solid angle produced in unit volume) radiated in a small frequency interval, $d\nu_C$, is[2] (67)

$$\epsilon_C d\nu_C = \frac{1}{4\pi} P_c(\gamma) N_e(\gamma) d\gamma, \tag{3.35}$$

i.e. the emissivity is the number of electrons with Lorentz factor γ multiplied by the power each one radiates, with the factor of 4π dividing the total power into unit solid angles. We can proceed to change this into a more informative expression if we first rearrange the equation,

$$\epsilon_C = \frac{1}{4\pi} P_c(\gamma) N_e(\gamma) \frac{d\gamma}{d\nu_C}, \tag{3.36}$$

and then substitute in Equations 3.21, 3.33 and 3.34. After some rearrangement we get

$$\epsilon_C = \frac{1}{4\pi} \sigma_T c U_{rad} \frac{4}{3} \gamma^{2-p} K \frac{1}{2} \left(\frac{3}{4}\right)^{\frac{1}{2}} \nu_C^{-\frac{1}{2}} \nu_0^{-\frac{1}{2}}. \tag{3.37}$$

By substituting in Equation 3.32 we finally get

$$\epsilon_C = \frac{1}{8\pi} \sigma_T c \frac{U_{rad}}{\nu_0} \left(\frac{4}{3}\right)^{\alpha} K \left(\frac{\nu_C}{\nu_0}\right)^{-\alpha} = \frac{1}{8\pi} \sigma_T c \frac{U_{rad}}{\nu_0} K \gamma^{-2\alpha}, \tag{3.38}$$

where $\alpha \equiv \frac{p-1}{2}$. We therefore see that if there is a power law distribution of electrons in a photon field, the inverse Compton emission also has a power law distribution.

3.4.1 The Klein-Nishina regime

The expression for the Thomson cross section, σ_T, is only valid for the non-relativistic regime, where the initial energy of the photon is $\frac{h\nu}{m_e c^2} = x \ll 1$. The complete expression derived using relativistic quantum mechanics is called the Klein-Nishina cross section and is given as (87)

$$\sigma_{KN} = \frac{3\sigma_T}{4} \left(\frac{1+x}{x^2} \left(\frac{2(1+x)}{1+2x} - \frac{1}{x} \ln(1+2x) \right) + \frac{1}{2x} \ln(1+2x) - \frac{1+3x}{(1+2x)^2} \right). \tag{3.39}$$

In the very high energy regime, when $x \gg 1$, this expression reduces to

$$\sigma_{KN} \approx \frac{3\sigma_T}{8x} \left(\ln(2x) + \frac{1}{2} \right), \tag{3.40}$$

[2] Ghisellini has an additional factor of $m_e c$ in his expression, which seems to be an error.

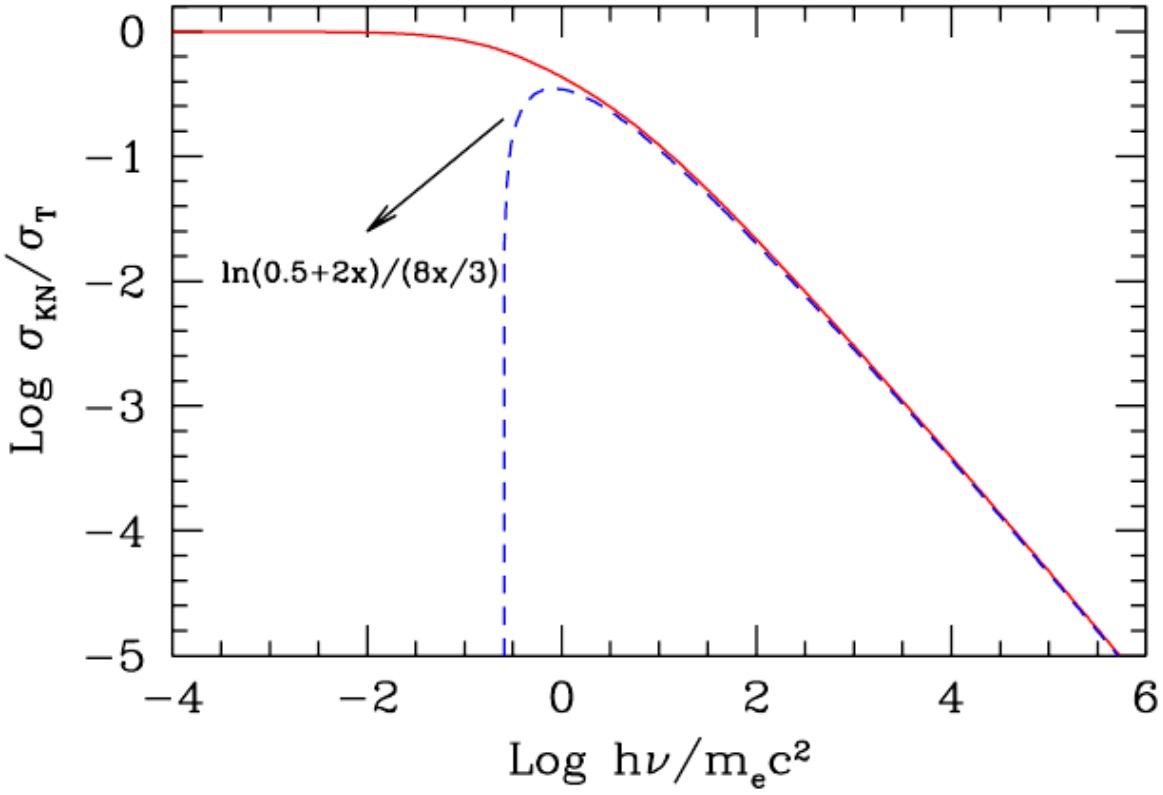

Figure 3.4: The Klein-Nishina cross section for scattering. The dashed blue line shows the approximation given in Equation 3.40. Image credit Gabriele Ghisellini (67).

and it can be seen that as energy increases into the Klein-Nishina regime the cross section for scattering becomes smaller, as is shown in Figure 3.4.

3.5 Cyclotron Radiation

Cyclotron radiation is the name given to the radiation emitted by a charged particle moving at non-relativistic speeds in a B-field. For clarity, I will assume the charged particle is an electron, which is the scenario most commonly encountered in this thesis, but the following discussion is easily generalised to other particles. Cyclotron radiation is not encountered much in this thesis, but is a precursor for its relativistic counterpart synchrotron radiation, which is a very common and important radiation process in high energy astrophysics.

Landau levels describe the wave functions of particles (in this case electrons) in a B-

field. We will derive them here and show how they lead to the emission of radiation at a characteristic frequency. We begin with the Hamiltonian for electrons in a B-field,

$$H = \frac{1}{2m}\left(|\hat{p}_x + \hat{p}_y + \frac{e}{c}\underline{A}|\right)^2, \tag{3.41}$$

where $\hat{p}$ is the momentum operator and A is the electromagnetic vector potential. By defining the Landau gauge as

$$\underline{A} = B(-y, 0, 0) = -By\underline{\hat{x}}, \tag{3.42}$$

we get

$$H = \frac{1}{2m}\left(p_x - \frac{e}{c}By\right)^2 + \frac{1}{2m}p_y^2. \tag{3.43}$$

Since $p_x = -i\hbar\frac{\partial}{\partial x}$ etc.,

$$E\psi = H\psi = \frac{1}{2m}\left(-i\hbar\frac{\partial}{\partial x} - \frac{eB}{c}y\right)^2\psi + \frac{1}{2m}\left(-i\hbar\right)^2\frac{\partial^2\psi}{\partial y^2}, \tag{3.44}$$

$$H\psi = -\frac{\hbar^2}{2m}\frac{\partial^2\psi}{\partial x^2} + \left(\frac{i\hbar}{m}\frac{eB}{c}y\right)\frac{\partial\psi}{\partial x} + \frac{1}{2m}\left(\frac{eB}{c}y\right)^2\psi - \frac{\hbar^2}{2m}\frac{\partial^2\psi}{\partial y^2}. \tag{3.45}$$

Since this expression is independent in x and y (no $x \cdot y$ terms), we can separate the solution as $\psi(x, y) = \phi_x(x)\phi_y(y)$. Here, $\phi_x(x)$ has the usual plane wave solution of the Shrödinger equation,

$$\phi_x(x) = e^{ik_x x}, \tag{3.46}$$

$$\frac{\partial\phi_x(x)}{\partial x} = ik_x e^{ik_x x}, \tag{3.47}$$

$$\frac{\partial^2\phi_x(x)}{\partial x^2} = -k_x^2 e^{ik_x x}, \tag{3.48}$$

and the equivalently for $\phi_y(y)$. By dividing both sides of Equation 3.45 by $\phi_x(x)$ we get,

$$H\phi_y(y) = \left(\frac{\hbar^2 k_x^2}{2m}\right)\phi_y(y) - \left(\frac{\hbar k_x}{m}\frac{eB}{c}y\right)\phi_y(y) + \frac{1}{2m}\left(\frac{eB}{c}y\right)^2\phi_y(y) - \left(\frac{\hbar^2}{2m}\right)\frac{\partial^2\phi_y(y)}{\partial y^2} \tag{3.49}$$

$$H\phi_y(y) = -\left(\frac{\hbar^2}{2m}\right)\frac{\partial^2\phi_y(y)}{\partial y^2} + \frac{1}{2m}\left(\hbar k_x - \frac{eB}{c}y\right)^2\phi_y(y) \tag{3.50}$$

We can get the solutions to this equation by comparing it to the well known Hamiltonian of a quantum harmonic oscillator, H_{QHO}, with the position operator $\hat{y}$ shifted by a quantity y_0,

$$H_{QHO} = \frac{\hat{p}_y^2}{2m} + \frac{1}{2}mw^2\left(\hat{y} - y_0\right), \tag{3.51}$$

which has the solutions,

$$\psi_n = \sqrt{\frac{1}{2^n n!}} \left(\frac{mw}{\pi\hbar}\right)^{\frac{1}{4}} e^{-mw\frac{(y-y_0)^2}{2\hbar}} H_n\left(\frac{mw}{\hbar}(y-y_0)\right), \tag{3.52}$$

where $H_n(y)$ are the Hermite polynomials.

To do this comparison, let us first rearrange Equation 3.50,

$$H\phi_y(y) = -\left(\frac{\hbar^2}{2m}\right)\frac{\partial^2\phi_y(y)}{\partial y^2} + \frac{1}{2m}\left(\frac{-eB}{c}\right)^2\left(-\frac{\hbar c k_x}{eB} + y\right)^2 \tag{3.53}$$

$$H\phi_y(y) = -\left(\frac{\hbar^2}{2m}\right)\frac{\partial^2\phi_y(y)}{\partial y^2} + \frac{1}{2}m\left(\frac{eB}{mc}\right)^2\left(y - \frac{\hbar c k_x}{eB}\right)^2, \tag{3.54}$$

and we see that Equation 3.52 is a solution where,

$$\psi_n = \phi_y(y), \tag{3.55}$$

$$y_0 = \frac{\hbar c k_x}{eB}, \tag{3.56}$$

$$w = \frac{eB}{mc}. \tag{3.57}$$

The quantum harmonic oscillator has energy levels of

$$E_n = \left(n + \frac{1}{2}\right)\hbar w. \tag{3.58}$$

This means that the electron can raise or lower energy levels by respectively absorbing or emitting a photon of energy

$$E_\gamma = \Delta n \hbar w = \frac{\Delta n}{2\pi} h w, \tag{3.59}$$

or equivalently of frequency

$$\nu_\gamma = \frac{\Delta n}{2\pi} w = \frac{\Delta n e B}{2\pi m c}. \tag{3.60}$$

Of course, the primary means of absorption and emission is between the ground state and the first excited state, $\Delta n = 1$. In practice, absorption and subsequent emission is so rapid that the electron effectively scatters the photon (158). Therefore, we see that the electron scatters photons of the B-field with a characteristic frequency $\nu_{cy} = \frac{eB}{2\pi mc}$ which is called the cyclotron frequency. Equation 3.60 is valid for particles other than electrons, providing suitable substitions for the particle's charge and mass are made. It can be seen that for a given B-field strength, heavier particles radiate at lower frequencies.

3.6 Synchrotron Radiation

We now consider synchrotron radiation which, as mentioned earlier, is similar to cyclotron radiation but with the electron moving at relativistic speeds with respect to the observer. Due to do Doppler boosting, the radiation scattered from the B-field increases in frequency:

$$\nu_s = \frac{\nu_{cy}}{\gamma} = \frac{eB}{2\pi\gamma m_e c}. \tag{3.61}$$

As with cyclotron radiation, this expression is valid for particles other than electrons if suitable substitutions for charge and mass are made.

We can determine several properties of synchrotron radiation very easily by analogy with those found for inverse Compton scattering derived earlier. The two processes are essentially the same, but for synchrotron radiation the energy density of the radiation field is the energy density of the B-field, $U_B = \frac{B^2}{8\pi}$. We can easily write expressions for the total power a single electron emits via synchrotron radiation:

$$P_s = \frac{4}{3}\sigma_T \gamma^2 c U_B, \tag{3.62}$$

and the synchrotron emissivity from a large number of electrons distributed in energy by a power law with index n,

$$\epsilon_s = \frac{1}{4\pi}\sigma_T c \frac{U_B}{\nu_0} \frac{\left(\frac{4}{3}\right)^\alpha}{2} K \left(\frac{\nu_s}{\nu_0}\right)^{-\alpha}, \tag{3.63}$$

where $\alpha \equiv \frac{p-1}{2}$. Again we find a power law energy spectrum, with the index related to the index of the electron energy spectrum.

For a given source, the ratio of the inverse Compton emissivity to the synchrotron emissivity is simply given by the ratio of the external radiation field's energy density to the B-field's energy density:

$$\frac{\epsilon_C}{\epsilon_s} = \frac{U_{rad}}{U_B}, \tag{3.64}$$

and of course the same relationship is true for the observed flux.

As we shall see in greater detail in the following chapter, the synchrotron self-Compton (SSC) scenario of AGN jets is where a single population of photons both emits synchrotron radiation and inverse Compton scatters the radiation to higher energies. We can find the emissivity in this case by starting with Equation 3.38 and recognising that if

the seed photons are the synchrotron emission, then $\nu_0 = \nu_s$ and the energy density of the synchrotron emission is (67)

$$U_{rad} = 4\pi \frac{3R}{4c} \epsilon_s, \tag{3.65}$$

$\frac{3R}{4c}$ being the light crossing time for the source, with R being its radius. This yields

$$\epsilon_{ssc} = \sigma_T R \frac{\epsilon_s}{\nu_s} \frac{\left(\frac{4}{3}\right)^{\alpha-1}}{2} K \left(\frac{4\gamma^2}{3}\right)^{-\alpha} = \sigma_T c \frac{2\pi R \gamma m \epsilon_s}{eB} \frac{\left(\frac{4}{3}\right)^{\alpha-1}}{2} K \left(\frac{4\gamma^2}{3}\right)^{-\alpha}. \tag{3.66}$$

Since $\epsilon_s \propto K$, we see that $\epsilon_{ssc} \propto K^2$.

As well as providing seed photons for upscattering, synchrotron emission can also contribute directly to the γ-ray flux if the radiating particles are highly accelerated protons. This will be covered in more detail in the following chapter but, put briefly, protons can become accelerated to higher energies than electrons since the cooling time for the more massive particles is longer. In order to undergo such accelerations large B-fields would be required and in these sorts of environments other emission processes will also become important, such as emission from π particles, which we shall cover presently, that are produced via the interaction of the accelerated protons with photons.

3.7 π Emission

One further mechanism for producing γ-rays which deserves mention is the decay of π^0 particles. As discussed in (41), it has been proposed that within AGN jets π^0s could be created through the interaction of accelerated protons with photons,

$$p + \gamma \rightarrow p + \pi^0. \tag{3.67}$$

The π^0s would then decay directly into two γ-rays:

$$\pi^0 \rightarrow \gamma\gamma, \tag{3.68}$$

contributing to the AGN's γ-ray emission. These γ-rays may not escape directly from their emission region. There would likely be a high density of photons in that area, for example the synchrotron emission of electrons co-accelerated with the protons. The γ-rays and low energy photons could then interact to create e^-/e^+ pairs, which could then emit synchrotron radiation which could potentially create further e^-/e^+ pairs. Through

synchrotron emission and pair production, the energy of the original γ-rays cascades down to lower energies (for further details see reference (110)).

π^0 decay process occurs very rapidly. The mean lifetime for a π^0 is only 2×10^{-16} s (142), which means that in order to produce a steady emission of γ-rays, π^0s must be constantly created. If protons are accelerated to high enough energies in AGN to produce γ-rays via this mechanism, then the AGN will also be a source of UHE cosmic rays (133). Proton-photon interaction can also create charged π particles. These would be expected to be present if protons were accelerated to high energies, along with their decay products: e^-, e^+ and μ particles, which would emit synchrotron radiation below γ-ray energies, and neutrinos. We will examine these cascades and their emission in slightly more detail in the next chapter.

Chapter 4

AGN Classification and Blazar Emission Models

4.1 Introduction

Although the original research of this thesis concerns only blazars, it is obviously necessary to place these objects in a wider context. For this reason, this chapter will cover the modern picture of active galactic nuclei (AGN) and the diverse observational objects that are understood within the framework of the unified AGN model, the idea that many seemingly different classes of objects are in fact very similar objects viewed from different angles. We will then go on to discuss the size and location of the γ-ray emission region within AGN jets and cover the possible γ-ray emission mechanisms.

4.2 The Unified Model AGN Classification

A small fraction of galaxies is observed to consist of active galaxies with high luminosity in some part of the electromagnetic spectrum (83). These were first discovered in the radio waveband in the 1950s, although it was not immediately evident what these bright objects were. Rapid variability observed in some of them meant that the region dominating the luminosity could be no larger than the size of the solar system, ruling out nuclear fusion as the source of the luminosity since this would require the region to be far denser than was credible. In 1969 Donald Lynden-Bell suggested that the luminosity could be powered by accretion onto a compact object (98).

In the modern view, it is now understood that this compact object is a supermassive black hole (the term *black hole* had been coined only a few years before Lynden-Bell's paper) in the centre of the galaxy, leading to these objects being named active galactic nuclei. The disc of accreted material is highly luminous, and in fact the accretion disc is

the primary and dominant source of luminosity in AGN that lack a jet. Surrounding the black hole are two clumpy regions of material: the broad line region (BLR) and, further out, the narrow line region (NLR). The whole system is surrounded by a dusty torus, as shown in Figure 4.1.

The luminosity of the accretion disc can be understood as the infalling matter being heated by friction and radiating thermally. Observationally, this is seen as a bump in the blue part of the optical specrum (the *big blue bump*) with significant emission in the UV and X-ray bands. The emission from the accretion disc heats the BLR, NLR and dusty torus, which then reradiate this energy.

The BLR has its namesake broad emission lines because, compared to the NLR, it is close to the central black hole. The material that composes the BLR therefore has large Keplerian velocities which broaden the emission lines. Even so, it is inferred that the BLR is composed of individual clouds and their relative motions further broaden the lines, otherwise the calculated BLR temperature would be around 10^{10} K, at which point the atoms would be ionised and not produce any lines (137). Despite this extra broadening, the temperature of BLR clouds is still inferred to be high, typically on the order of 10^4 K. This is because of the BLR's proximity to the central black hole which means it receives a large amount of heat from the accretion disc. The high temperature of the BLR material means that collisions between gas particles are more frequent, quickly de-exciting the gas. This is not true of the cooler NLR, where the relatively infrequent collisions allow gas particles to exist in 'forbidden' states, leading to the observation of forbidden emission lines in the NLR.

The thick, dusty torus, further out, absorbs the radiation of the accretion disc and re-emits it predominantly in the infrared regime. As well the radiation it emits, the dusty torus has very important effects on AGN observations due to the radiation that it obscures. If the object is viewed side-on to the dusty torus, which we define as a large viewing angle, then only emission from the dusty torus and the NLR is seen, the rest of the object being blocked by the dusty torus. As we see in Figure 4.1, this type of object is known as a Seyfert II galaxy. As the viewing angle is decreased the BLR becomes visible and the object is known as a Seyfert I galaxy. Finally, at smaller viewing angles, radiation directly from the accretion disc is visible and this is known as a quasar.

The next major consideration for AGN classification is the amount of radio emission.

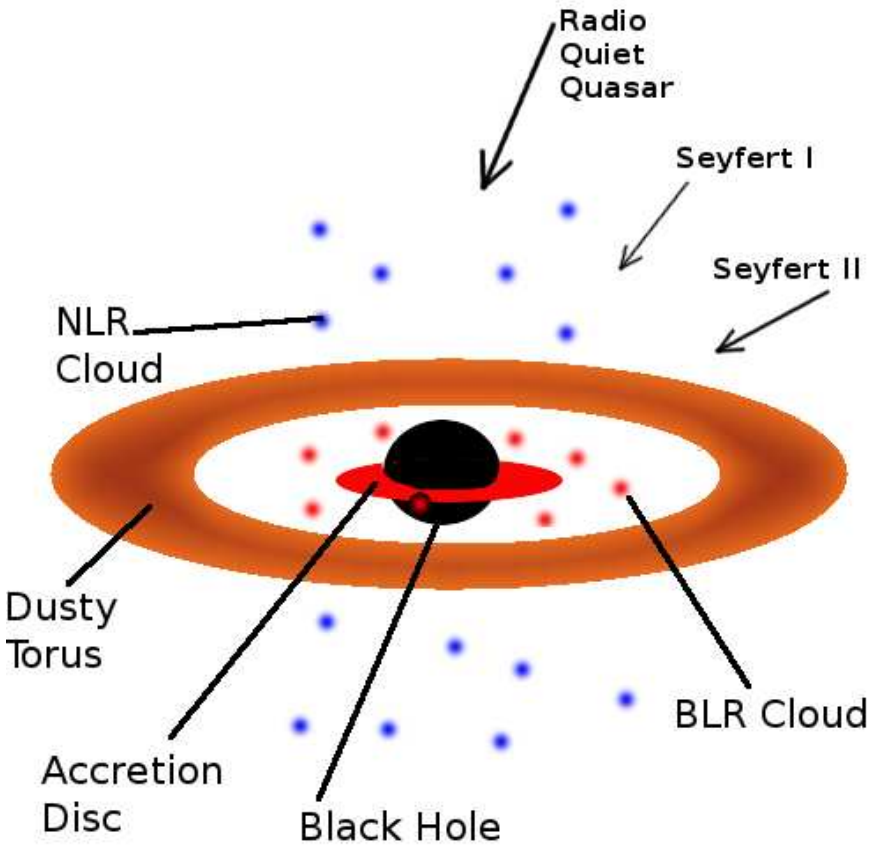

Figure 4.1: Schematic of the unified model of AGN. Different radio quiet object types and their viewing angles are also shown with arrows.

The objects described so far are the so-called radio quiet objects. If the ratio of the flux at 5 GHz to the flux in the optical B band, $\frac{F_{5\mathrm{GHz}}}{F_B}$, is greater than 10, then the object is considered radio loud. This radio loudness is generally attributed to the existence of a jet in the object, although some objects without a jet can meet the aforementioned definition and some objects with a jet are still classed as radio quiet (39). About 10% of AGN have relativistic jets which produce non-thermal radio emission, and these objects are on average 1000 times brighter in the radio band than radio quiet AGN. Whether an object is radio loud is thought to depend on several factors: having a large spin, having a large accretion rate, and having a geometrically thin accretion disc. These factors are products of the object's accretion and merger history (149).

The classification of an object is different if it is radio loud: quasars are simply classified as radio loud quasars as opposed to being classified as a radio quiet quazars.

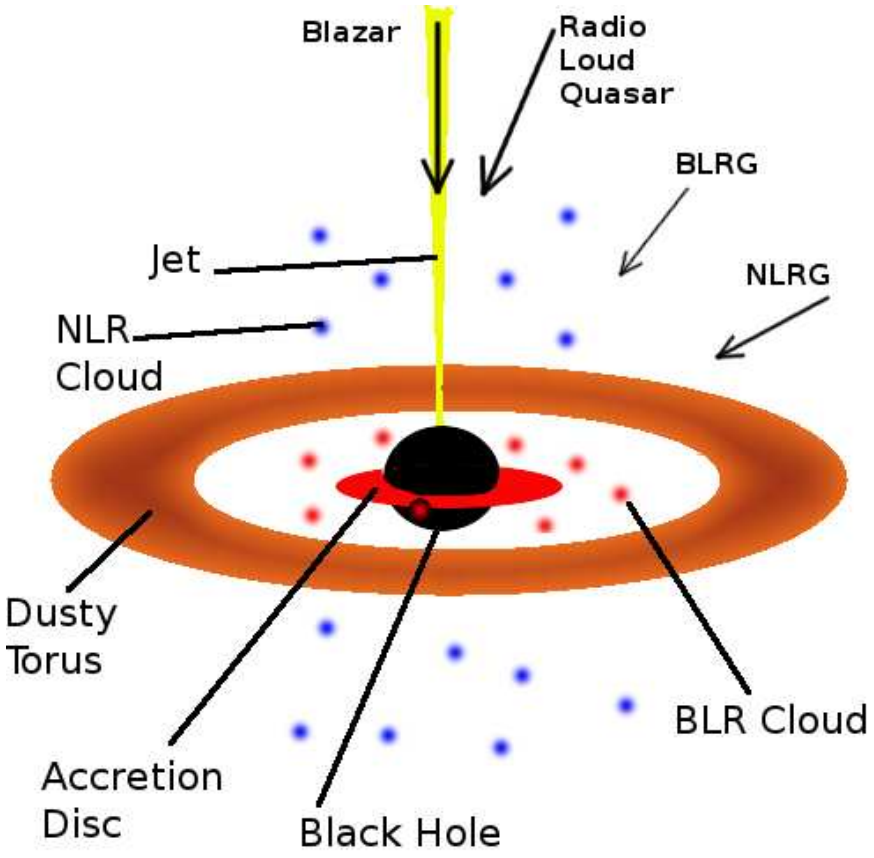

Figure 4.2: Schematic of the unified model of AGN. Different radio loud object types and their viewing angles are also shown with arrows.

Seyfert I galaxies become broad line region galaxies (BLRGs), and Seyfert II galaxies become narrow line region galaxies (NLRGs) or LINERS (low-ionisation nuclear-emission-line regions). The latter objects resemble NLRGs with faint lines, although it is debatable whether these objects are actually AGN (157). An object being viewed with with a small angle to the jet axis is classified as a blazar. The unified model of radio loud objects is shown in Figure 4.2

Radio loud AGN can be further split into two observational groups. In Fanaroff-Riley I (FR I) galaxies the brightest emission from the radio jet is close to the core, while in Fanaroff-Riley II (FR II) galaxies the brightest emission is seen from lobes where the radio jet terminates. Examples of an FR I and an FR II galaxy are shown in Figure 4.3. The cause of this difference is believed to be the amount of kinetic energy contained in the jet.

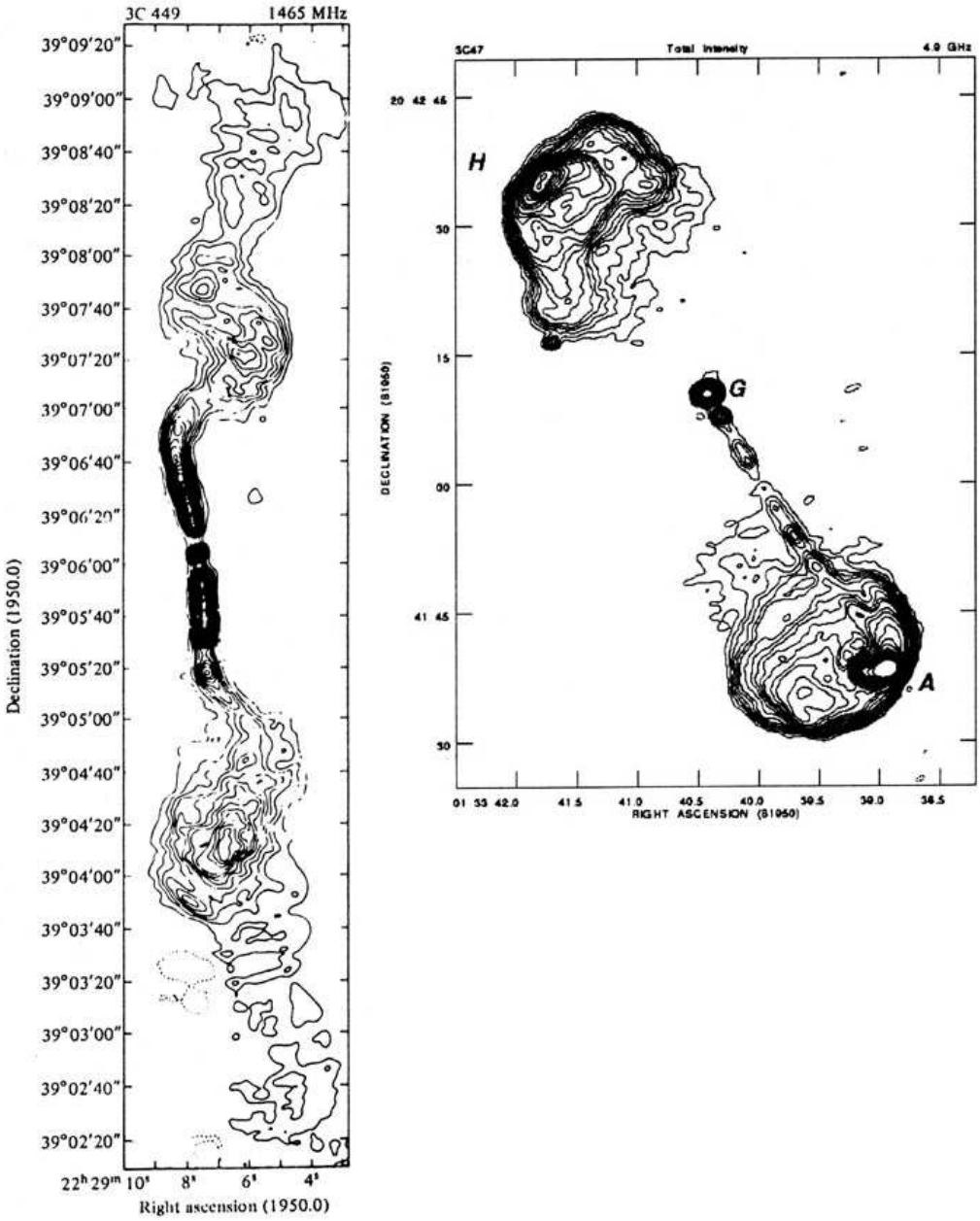

Figure 4.3: Left: Example of a Fanaroff-Riley I galaxy, 3C 449. Right: Example of a Fanaroff-Riley II galaxy, 3C 47. Image credits, (121), (42) via http://ned. ipac. caltech. edu/

Most relevant to this thesis are blazars where the viewing angle is very small. As we shall see in the following section, blazars can be very powerful emitters of both radio waves and γ-rays. The emission is especially bright since the jet travels towards the observer at relativistic speeds and therefore the radiation becomes beamed and Doppler boosted.

Blazars can be further subdivided into two classes. Firstly, there are BL Lacertae type objects (BL Lacs) in which emission from the BLR is weak or not observed. These objects are thought to be FR I galaxies viewed at a small angle. Secondly, there are flat spectrum radio quasars (FSRQs) which do have appreciable emission from the BLR and are thought to be FR II galaxies viewed at a small angle (108). In addition, there are also steep spectrum radio quasars (SSRQs), defined such that the spectral index of the radio emission $\alpha > 0.5$. These are thought to be the same objects as FSRQs but viewed at slightly larger angles.

The broad picture given above has changed little since the 1970s, and seems unlikely to undergo paradigm shifts. The most significant change in recent years is the idea that the dusty torus probably has a clumpy structure which leads to the object classification being a *probabilistic* function of viewing angle (57). For example, it may be possible to view an object at large angles and directly see the BLR or accretion disc if, by chance, none of the clumps forming the dusty torus intersects the line of sight.

4.3 γ-ray Emission from Blazars

Blazars emit radiation right across the electromagnetic spectrum. On a plot of $\log(\nu)$ against $\log(\nu L_\nu)$, where L is the luminosity, blazars are characterised by a twin-peaked shape (see Figure 4.4). The low energy peak occurs at radio through to X-ray energies and the high energy peak, where observed, is at γ-ray energies (62). In FSRQs, this synchrotron peak frequency, ν_s, tends to be lower than in BL Lacs. Indeed, for FSRQs the synchrotron peak tends to be observed in the infrared and has never been observed above optical frequencies. The wider spread in synchrotron peak frequencies ν_s in BL Lacs leads to them being subdivided into low-synchrotron peaked BL Lacs (LBLs) with 10^{14} Hz $< \nu_{\rm s} < 10^{15}$ Hz and high-synchrotron peaked BL Lacs (HBLs) with $\nu_s > 10^{15}$ Hz (71). (These numbers are only approximate, and different authors use different defi-

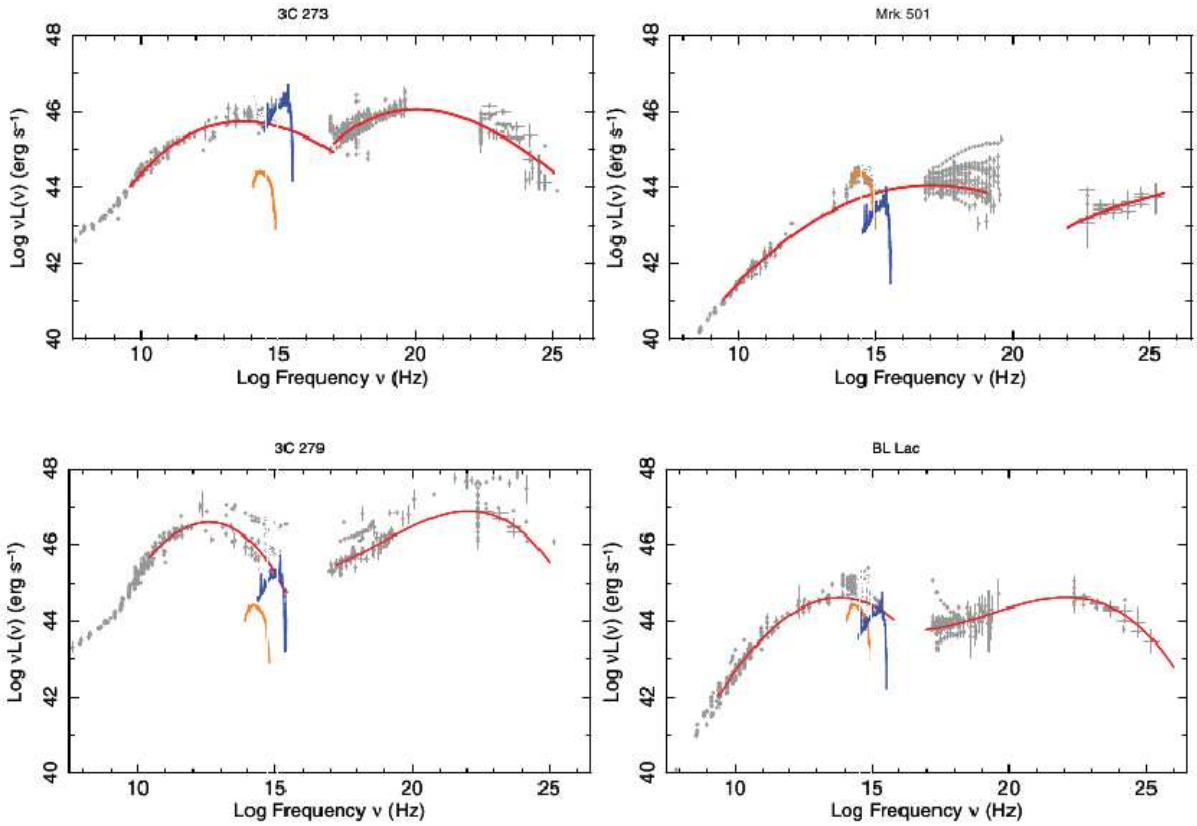

Figure 4.4: Example SEDs of four representative blazars, objects in the left column are FSRQs and objects in the right column are BL Lacs. The red lines are non-thermal emission, blue lines are emission from the disc and BLR, and orange lines are emission from the host galaxy. Image credit (71).

nitions, with some also defining intermediate-peaked BL Lacs.) The low energy (synchrotron) peak and the high energy peak correlate with one another (62). In their 1998 study, Giovanni Fossati et al. (62) also assert that the greater the intrinsic luminosity of a blazar (based on either its radio or bolometric luminosity), the lower its synchrotron peak energy (the 'blazar sequence'). However this claim has been disputed by Paolo Giommi et al. (71) who claim that the blazar sequence is due to a selection effect. Essentially, they suggest that BL Lacs with high intrinsic luminosity and a high synchrotron peak energy evade being included in samples since the non-thermal jet emission tends to drown out emission lines, which makes it difficult to establish a redshift and therefore an intrinsic luminosity.

We now turn to the question of how blazars produce γ-ray emission. The first ques-

tion is whether the emission is leptonic or hadronic, i.e., is the γ-ray emission produced by leptons or hadrons? We saw in Chapter 3 how both cases could work in principle. In the leptonic scenario, low energy seed photons are provided by synchrotron emission or an external source and then high energy electrons and positrons in the jet inverse Compton scatter these seed photons to γ-ray energies. In the hadronic scenario, decaying π^0s or the synchrotron emission from high energy protons produces the γ-ray emission.

To be pedantic, the answer of course is that both processes play a role. As long as there is one electron and one proton accelerated to high energies in the jet then there will be both leptonic and hadronic emission, but it is sensible to ask which process dominates. Since the composition of the jet is still uncertain, the question cannot be answered definitively. Jets are known to be electrically neutral since they are not observed to attract charged objects, so we can at least be confident that electrons exist in the jet in large numbers and therefore some leptonic emission is expected. Leptonic models are presently favoured in the literature and have had broad success fitting multiwavelength observations. Some challenges remain, including explaining the variability timescales observed at γ-ray energies. The cooling timescales of the synchrotron and Compton processes (the time taken for electrons to radiate their energy away) is highly model dependent, since they are defined by the B-field and photon field that the electrons are in. Typically though the synchrotron cooling time is of the order of 1×10^4 s and the Compton cooling time is of the order of 1×10^6 s (136). The observed γ-ray variability of around 10 s requires detailed modelling to explain in an SSC scenario, taking into account both the geometry of the emission region and the varying, time-dependent cooling across it (e.g. (159)).

The very short timescale variability that is sometimes observed poses an even larger hurdle for hadronic models, given that proton synchrotron radiation, the dominant hadronic emission mechanism, has typical cooling times of several days (although lower under certain conditions, e.g. (17)). Efforts to solve this problem are compounded by the computational demands of modelling time variability in hadronic models (41). Variability could arise from causes other than radiatitive cooling, for example it could be due to changes in the viewing angle leading to a change in the Doppler beaming. There has also been interesting research showing that rapid variability can occur if a red giant star or similar object crosses the jet (33).

Before we look at leptonic and hadronic models in slightly more detail, we need to consider the size and location of the emission region within the jet.

4.3.1 Size of the Emission Region

We can set a lower limit on the size of the emission region from an argument about the opacity of the source (67). γ-rays can interact with a low energy photon to form an e^-/e^+ pair which annihilates the photons. In order that we can observe the high energy emission, the density of low energy photons at the emission region, u, must be low enough that the emission region does not become opaque. The optical depth of the emission region is

$$\tau(\epsilon) = \int_r \int_E \sigma_{\gamma\gamma}(\epsilon, E) u(E, r) dE dr, \tag{4.1}$$

where ϵ is the γ-ray energy, E is the low energy photon energy, r is the distance the γ-ray must travel to escape. $\sigma_{\gamma\gamma}$ is the photon-photon cross section which peaks at $\sigma_{\gamma\gamma} \approx 0.2\sigma_T$ when $\frac{\epsilon E}{m_e^2 c^4} \approx 4$ (58).

If we make the approximation that u is constant throughout the emission region of radius R and consider only the energy E that leads to maximum $\sigma_{\gamma\gamma}$ then we can say

$$\tau = 0.2\sigma_T u \frac{3R}{4}, \tag{4.2}$$

where $\frac{3R}{4}$ is the average distance for the γ-ray to travel to escape (67). In this case,

$$u = \frac{L'}{V} t_{esc}, \tag{4.3}$$

where L' is the rest frame luminosity of the emission region and V is the proper volume of the emission region. $t_{esc} = \frac{3R}{4c}$ is the average escape time for a low energy photon, for a given luminosity, if the escape time is longer then more photons will be within the source at a given instant. This gives

$$u = \frac{3L'}{4\pi R^3} \frac{3R}{4c} = \frac{9}{4} \frac{L'}{4\pi R^2 c}. \tag{4.4}$$

We can relate the observed luminoisty to the luminosity in the rest frame, $L' = \frac{L}{\delta^4}$, where δ is the Doppler factor with respect to the observer to get

$$u = \frac{9}{4} \frac{L}{4\pi \delta^4 R^2 c}. \tag{4.5}$$

We can relate u to the observed photon flux at low energy, F_{obs}, using $L = 4\pi d_L^2 F_{obs}$, where d_L is the object's luminosity distance from us.

$$u = \frac{9}{4}\frac{d_L^2 F_{obs}}{\delta^4 R^2 c}, \tag{4.6}$$

From Equation 4.2, this leads to

$$\tau = 0.2\frac{9}{4}\frac{3\sigma_T}{4}\frac{d_L^2 F_{obs}}{\delta^4 R c}, \tag{4.7}$$

and since we require $\tau < 1$ for all visible energies of ϵ,

$$R > 0.2\frac{9}{4}\frac{3\sigma_T}{4}\frac{d_L^2 F_{obs}}{\delta^4 c}. \tag{4.8}$$

For an example, let us take the archetypal object BL Lacertae which has has a low energy peak of $\nu F_\nu = 1 \times 10^{13}$ JyHz at 1×10^{14} Hz (41).

At 1×10^{14} Hz each photon has energy $E = 6.63 \times 10^{-20}$ J. This leads to a photon flux of

$$\frac{F_\nu}{E} = 7.1 \times 10^3 \text{ ph s}^{-1} \text{ cm}^{-2}. \tag{4.9}$$

BL Lacertae is at redshift $z \approx 0.07$ which corresponds to $d_L = 3 \times 10^8$ pc [1]. Substituting this into Equation 4.8 we get

$$R > \frac{3 \times 10^4}{\delta^4} \text{ pc}. \tag{4.10}$$

While the Doppler factor is an unknown, realistically $10 < \delta < 100$ leading to

$$R > 3 \times 10^{-4} \text{ pc}. \tag{4.11}$$

Blazars are highly variable objects, and variation of more than a factor of unity on minute timescales has been observed. This observed variability timescale t_{obs} lets us set an upper limit such that the size of the emission region is less than the light crossing time:

$$R \leq \frac{\delta c t_{obs}}{1+z}, \tag{4.12}$$

BL Lacertae has been observed to vary on time scales $t_{obs} = 15$ minutes (29). Then we can see an upper limit of

$$R \leq \delta 2.5 \times 10^{11} \text{ m} = \delta 8 \times 10^{-6} \text{ pc}. \tag{4.13}$$

[1] Ned Wright Cosmology calculator http://www.astro.ucla.edu/ wright/CosmoCalc.html

Table 4.1: Typical Emission Region Parameters for a Blazar

B-Field	δ	R	r
G		pc	pc
0.2	20	3×10^{-3}	5×10^{-2}

Typical parameters for the γ-ray emission region found in blazars (156). See text for explanations of the column headings.

And keeping our assumption that $10 < \delta < 100$, this leads to

$$R \leq 8 \times 10^{-4} \text{ pc}. \tag{4.14}$$

Combined with the upper limit we calculated, this tells us that the emission region is well constrained to be on the order of 10^{-4} pc. This assumes of course that the flaring emission and the quiescent emission come from the same region of the jet, which may not be true. Either way, this result tells us that a really quite small region can dominate the γ-ray emission. It is still uncertain what this region is. For simplicity it is usually assumed to be a blob-in-the-jet, i.e. a region of denser material that is injected for some reason. Other suggestions for this region include a boundary between structures within the jet (69) or a site of magnetic reconnection (70).

4.3.2 Location of the Emission Region

It is especially surprising that such a small region is responsible for the γ-ray emission when the size of the jet itself is considered. By definition, blazars are viewed at a small angle down the jet and the projection effect makes it hard to determine the size of the jet. However, arguments can be made about the jet size, most robustly by studying AGN viewed at large angles. A well-collimated jet extending tens of kpc is common, especially in FR II galaxies (74), whereas collimation in FR I galaxies is typically less than a few kpc (143). (There are, of course, exceptions, e.g. E1821+643 which is an FR I galaxy with jet extending ≈ 280 kpc (39).) These well-collimated regions tend to feed into large structures of kpc to several hundred kpc size such as plumes, lobes or hotspots (127).

So where in these massive structures is the γ-ray emission region located? As mentioned, Martin Rees (130) originally identified bright knots in the jet as shock fronts,

where we have reason to believe γ-ray emission could originate. It has been suggested that in M87 one of these knots, located $r = 120$-$200\ \mathrm{pc}$ from the central black hole, could dominate the TeV energy emission (49). At GeV energies, a recent paper modelled the emission region in PKS B1424-418 to be $r \approx 5$-$10\ \mathrm{pc}$ from the central black hole (147). The requirement that the emission region remain transparent to γ-rays also allows us to constrain the position of the emission region. As we saw in the previous subsection, if the density of low energy photons is great enough then the optical depth to γ-rays becomes very high. The region close to the central black hole would be rendered opaque due to the large amount of low energy photons from the accretion disc (and BLR where present). This generally requires the γ-ray emission region to be placed beyond the radius of the BLR ($0.1\ \mathrm{pc}$, (84)). We shall discuss this again in greater detail in Chapter 7 where we look for, and fail to find, evidence of absorption from BLR photons, leading us to the conclusion that the emission region is beyond the BLR.

In summary, it would appear that typically the γ-ray emission region is $\approx 10^{-4}\ \mathrm{pc}$ in size and located ≈ 0.1 - $200\mathrm{pc}$ from the central black hole. For context, the typical parameters for the γ-ray emission region of a blazar found in an observational study are shown in Table 4.1. The B-field strength in blazar jets are sometimes estimated to be much higher, on the order of 1 - $10\ \mathrm{G}$ (116) (68).

4.3.3 Leptonic models

Since the low energy peak in the SED is due to synchrotron emission from electrons in the jet, it is unavoidable that these synchrotron photons are also available as targets for inverse Compton upscattering by the same electron population. This type of emission process is known as the synchrotron self-Compton (SSC) model. Because the same population of electrons produces both the synchrotron and the inverse Compton emission, there are several observational links between the two energy bands that can be expected from this type of emission during flares. The exact trends depend upon the parameters that change to cause the flare, for example the B-field or the energy distribution of the electrons, but in general both the synchrotron and inverse Compton emission would be expected to vary together or with a slight time lag due to the light crossing time of the seed photons and the different cooling timescales in different wavebands. This modelling has been successfully applied to multiwavelength data (e.g. (102), (141)).

If another source of target photons exists other than the synchrotron photons, then these too can be inverse Compton scattered and contribute to, maybe even dominate, the γ-ray emission. This is called the external Compton (EC) model. Depending upon the site of γ-ray production, there are many external photon fields that could provide the seed photons: the accretion disc, the BLR, the dusty torus or the CMB. Due to the stronger emission observed from their BLRs, FSRQs are expected to have a higher contribution of EC emission compared to BL Lacs. This picture is also consistent with the fact that the high energy peak of FSRQs tends to be at lower energies than in BL Lacs: the additional target photons allow for more efficient cooling. In fact, it has been shown (40) that as the density of the external photon field increases, the high energy peak decreases proportionally.

4.3.4 Hadronic models

We can see from Equation 3.60 that for a particle as massive as a proton to emit synchrotron radiation, very large B-fields are required ($\approx$ 30-100 G (17) as opposed to values of $\approx$ 0.1 - 1 G which are more typical in leptonic models as we saw earlier). Although the requirement of large B-fields poses a theoretical hurdle, proton synchrotron radiation could account for γ-ray emission from blazars. This is because protons could be accelerated to higher energies than electrons. For all particles there is a synchrotron cutoff energy when the cooling time via synchrotron emission roughly equals the acceleration time for the particle. The cutoff for electrons appears at lower energies than for protons (17), because the cooling time for electrons ($\approx 10^3$ s in these B-fields) is far shorter than for protons ($\approx 10^5$ - 10^6 s). Still, the cutoff in the emitted synchrotron spectrum of electrons coaccelerated in large B-fields could be as high as ≈ 0.16 GeV (17)

Proton synchrotron radiation would be the main contributor to the TeV γ-ray emission in these hadronic models since other processes have longer cooling times (e.g. photomeson production has a cooling time of order 10^7 s (17)). But in such an extreme environment many processes must be considered that that would contribute across the electromagnetic spectrum. The simplest process is Bethe-Heitler pair production (109):

$$p + \gamma \rightarrow p + e^+ + e^-. \tag{4.15}$$

Another simple process is the interaction of a proton and a low energy photon to

produce a stable particle and a π particle:

$$p + \gamma \rightarrow p + \pi^0 \tag{4.16}$$

$$p + \gamma \rightarrow n + \pi^+. \tag{4.17}$$

Less straightforwardly, proton-photon interaction creates π particles of all charges along with unstable Δ particles (111) which decay into further π particles.

The neutral π^0 particles decay directly into γ-ray photons while the charged π particles undergo further decay (30):

$$\pi^+ \rightarrow \mu^+ + \nu_\mu \rightarrow e^+ + \nu_\mu + \bar{\nu}_\mu + \nu_e, \tag{4.18}$$

$$\pi^- \rightarrow \mu^- + \bar{\nu}_\mu \rightarrow e^- + \nu_\mu + \bar{\nu}_\mu + \bar{\nu}_e. \tag{4.19}$$

Synchrotron radiation from the μ particles contributes significantly to the high-energy peak while radiation from the electrons formed in these decays contributes to the low-energy peak along with the original electrons (41). The shape of the emitted spectrum will be defined not only by the directly emitted photons but also those emitted in the cascades resulting from pair production (110), as mentioned in the previous chapter.

As we can see, the end state of the π decay produces several neutrinos. The search for a neutrino flux from AGN by detectors like IceCube could provide much insight into the emission processes (31).

Chapter 5

Extragalactic Background Light and Axions

5.1 Introduction

In this chapter I will start by explaining what the extragalactic background light (EBL) is and how how it makes the universe opaque to VHE γ-rays via photon-photon absorption. We will see how some early VHE observations of extragalactic sources showed the universe to be more transparent than first imagined and discuss the current models of the EBL. I will then introduce axions and axion-like particles (ALPs), which are hypothetical particles which extend the standard model. The existence of ALPs could make the universe more transparent to VHE γ-rays by mitigating EBL absorption.

5.2 Extragalactic Background Light and its Effects

The EBL is the diffuse light present throughout intergalactic space. As we have already seen several times in this thesis, there is a chance of an interaction between a γ-ray and a low energy photon which will annihilate both photons and create an e^-/e^+ pair. Of course, there is nothing special to exclude the EBL photons from this process, so in travelling through intergalactic space a γ-ray has a chance of being annihilated with an EBL photon (66), thus giving the universe an optical depth to γ-rays. Since the chance of the annihilation ocurring is dependent on the energies of the photons involved, the optical depth is a function of both a γ-ray's energy and the density of the EBL as a function of energy (known as the EBL's shape) which is a function of redshift. The complete optical

depth is given as (21).

$$\tau(\epsilon, z) = \int_0^z dl(z) \int_0^\infty dE \sigma_{\gamma\gamma}(\epsilon, E) n(E, z), \tag{5.1}$$

where $dl(z) = cdt(z)$ is a proper line element, ϵ is the γ-ray energy, E is the EBL photon energy, $\sigma_{\gamma\gamma}$ is the photon-photon cross section and n is the EBL photon density. When the optical depths are calculated, for example in Chapter 9, we see that as a general rule τ increases with ϵ.

As it turns out, due to the shape of the EBL, it is infrared photons which provide most of the optical depth to γ-rays, with optical-UV photons also playing a significant role (21). Due to its lower photon energies, the dominant source of energy in the EBL, the CMB (76), does not play an important role in the absorption of γ-rays. Photons of infrared-UV energies primarily originate from stars, both by direct emission and reprocessed emission after absorption by dust (61). For a recent review on the subject of the EBL and its absorption of γ-rays see reference (56).

5.3 Modelling the EBL

Measuring the intensity of the EBL directly is challenging due to the fact is is very faint compared to foreground emission, principally the zodiacal light of the Sun reflecting on dust. Nevertheless, the team of the DIRBE instrument aboard the COBE satellite claimed tentative detection of the EBL around $3.5\ \mu\mathrm{m}$ (55). Lower limits on the EBL level can be obtained fairly straightforwardly using a method of galaxy counts. A relatively deep survey is performed to count the number of galaxies as a function of luminosity in an area of sky. The total light emitted from galaxies can then be found by integrating this luminosity function. This technique yields only a lower limit because it cannot guarantee that there are not fainter galaxies that evade detection and thus do not contribute to the integral. Similarly, if sources other than galaxies (e.g. Population III stars) were to contribute significantly to the EBL these would not be included in this method. By combining the direct DIRBE measurements with galaxy count limits and other data, a review was published in 2001 which described the spectrum of the EBL between 0.1 and $10^3\ \mu\mathrm{m}$ (76).

However, in 2006 the H.E.S.S. collaboration demonstrated that intergalactic space was more transparent to γ-rays than this EBL model implied (Aharonian et al., 2006) (21).

This claim was based the γ-ray spectra of two blazars, H 2356-309 and 1ES 1101-232. When the observed spectra were corrected for the effects of EBL absorption ('de-absorbed'), the intrinsic spectral indices that were inferred were extremely hard, $\Gamma_{int} < 1.5$. Given the understanding of particle acceleration within blazars (see Chapter 3), and measurements of the spectral indices of nearby blazars less affected by EBL absorption, such hard spectral indices were hard to credit. The conclusion was that the EBL model used was an overestimate, one likely explanation being that the direct EBL measurements by DIRBE were erroneous. In fact, the shape of the EBL inferred from the H.E.S.S. measurements was very close to the lower limits set by galaxy counts.

Since then there has been much work trying to characterise or set limits on the shape and intensity of the EBL, which is summarised in Figure 5.1. One technique, similar to that used by Aharonian et al. (2006), is to see what shapes can be used to de-absorb VHE blazar spectra and still obtain physically sensible results. (This technique was also used in Hauser and Dwek (2001), but at the time only a few, fairly local blazars had been measured.) Since the launch of *Fermi* additional constraints can be applied to these analyses by demanding that for a given source the de-absorbed VHE spectrum is consistent with the measured *Fermi* spectrum, which is at lower energy and therefore suffers less absorption. These approaches are useful but they do have to make some conservative assumptions. For example Orr, Krennrich and Dwek (2011) (115) and Meyer et al. (2012) (106) require that the VHE spectrum is softer than the *Fermi* spectrum, which is a reasonable assumption but there is no way of knowing just how much softer the VHE spectrum actually is. Ackermann et al. (2012) (13) examined the LAT spectra of 150 blazars that spanned the optically thin and thick regimes. The measured spectra from the optically thin regime were extrapolated into the optically thick regime and an EBL shape was found such that this extrapolation matched the observed spectrum. In this way a direct measurement was made of τ energies below 0.5 TeV.

Another approach is to base the EBL level on galaxy counts or surveys. Multiwavelength models are attached to each observed galaxy in order to calculate the total luminosity. These multiwavelength models are either based on local galaxies and then adjusted to the appropriate redshift by a phenomenological evolution (backward evolution method, e.g. Franceschini, Rodighiero and Vaccari (2008) (63)) or based on observations at the approriate redshift (e.g. Domínguez et al. (2011) (54)).

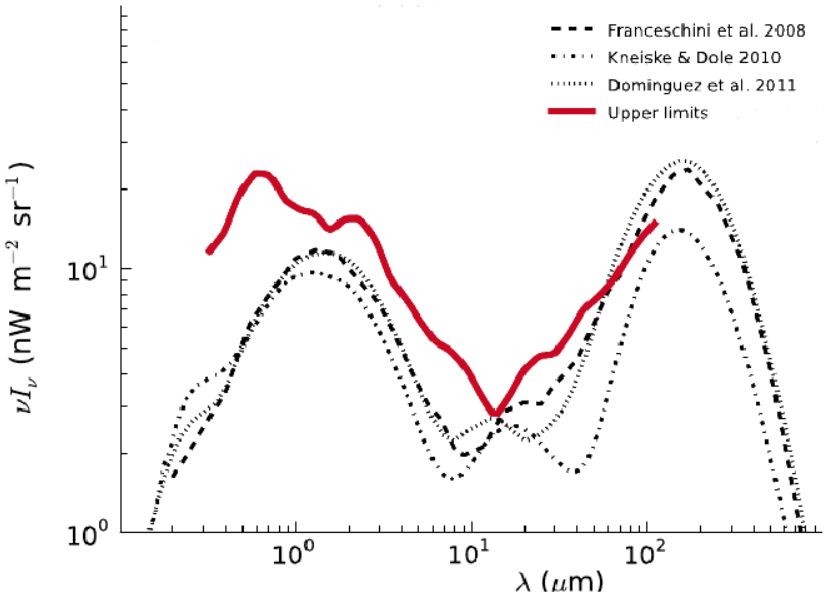

Figure 5.1: Upper limits from Meyer et al. (2012) (106) along with EBL models of Franceschini, Rodighiero and Vaccari (2008) (63), Kneiske and Dole (2010) (88) and Domínguez et al. (2011) (54). Image credit (106).

Finally, another method is to calculate the EBL from the amount of star formation observed in galaxies, which is in turn based on the observation of certain tracers for star formation such as $Lyman\ \alpha$. The emission from the inferred stellar populations is then calculated, see for example Kneiske, Mannheim and Hartmann (2002) (89). A similar work has been performed fitting to the lower limits of the star formation estimates (as opposed to the best star formation estimates), yielding a lower limit EBL model: Kneiske and Dole (2010) (88).

Broadly speaking, these various efforts at EBL modelling are in agreement, especially in the overall shape of the EBL, as can be seen in Figure 5.1, and in the values of τ as a function of energy, as can seen in Figure 5.2. However, some disagreement does exist. For example, the galaxy count models of Kneiske et al. (2002) (89), Franceschini, Rodighiero and Vaccari (2001) (63) and Domínguez et al. (2011) (54) are all in $> 3\sigma$ disagreement with the VHE based model of Orr, Krennrich and Dwek (2011) (115). However, that paper also claims the EBL level is consistent with the DIRBE measurement at

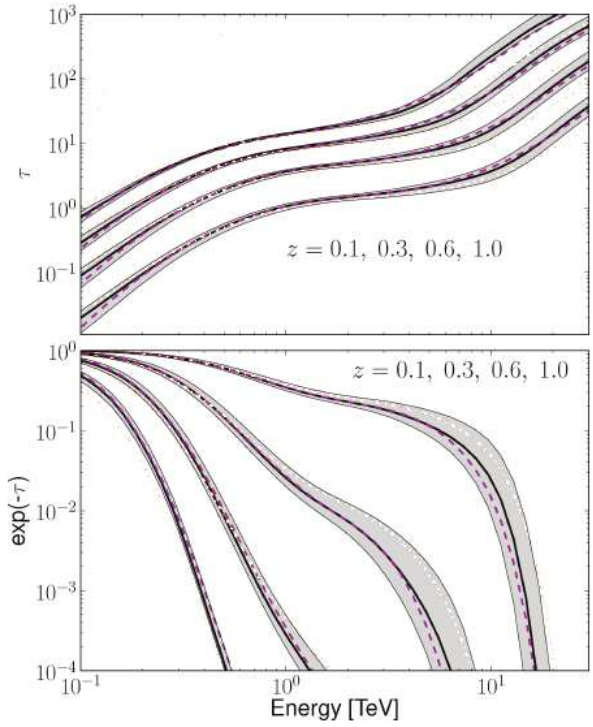

Figure 5.2: Upper panel: τ as a function of observed energy for several redshifts. Lower panel: flux attenuation as a function of observed energy for several redshifts. The black line is the model of Domínguez et al. (2011) (54) with the shadow region indicating the uncertainty (see reference). The dashed purple line is the model of Franceschini, Rodighiero and Vaccari (2008) (63). Image credit (54).

$3.5\ \mu\mathrm{m}$, which is in disagreement with other publications e.g. Aharonian et al. (2006) (21). Kneiske et al. (2002) (89) are in $> 2\sigma$ disagreement with the *Fermi* measurements of Ackermann et al. (2012) (13) and appear to be in disagreement with Meyer et al. (2012) (106), although the significance was not calculated.

Despite the relatively good agreement between the EBL models, confronting them with observations of distant blazars still yields some puzzling results. For example, applying the model of Franceschini, Rodighiero and Vaccari (2008) (63) to the object 1ES 1101-232 yields an intrinsic spectral index of $\Gamma \approx 1.6$ and models closer to Kneiske et al. (2002) (89) would yield indicies closer to $\Gamma = 1.0$ (94). Such results may indicate a problem with the EBL models, or may indicate unexpected physics in the emission mechanism. For example, it has been shown that an electron distribution that is Maxwellian (94) or has a low energy cut off (148) (85) can reproduce such hard intrinsic

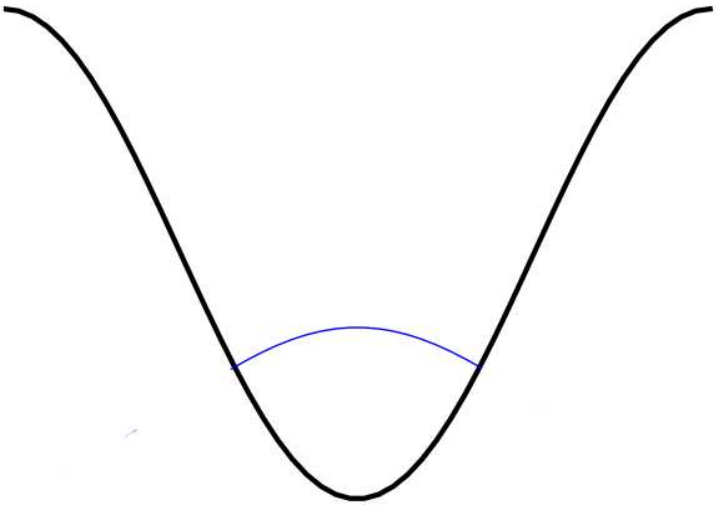

Figure 5.3: Single potential well (black) with the vacuum solution (blue).

spectra. Although these scenarios raise questions as to how plausible it is such an electron distribution can be produced and sustained, they show that at least in principle it is possible to explain the observed spectra with current EBL models. If this is the case then one challenge would be to explain why only distant blazars have such hard spectra. Another possible explanation for these discrepancies is the existence of the hypothetical axion particle, as we shall see in the following section.

5.4 Axions and their effects on the AGN Spectra

5.4.1 Instantons

I will now give a very brief introduction to instantons, which are necessary for understanding the motivation for axions. Imagine a single particle trapped in a potential well of the form given in Figure 5.3. If the particle is measured to be at $(x,t) = (x_0, t_0)$ then the probability for it to be found at some time dt later at (x_1, t_1) is given by the propagator

$$K(x_1, t_1; x_0, t_0) =< x_1|e^{-i\hbar H dt}|x_0 >= \int Dx e^{-iS/\hbar}, \tag{5.2}$$

where H is the Hamiltonian of the system. The action, S, and therefore also K, are dominated by transitions to the ground state which lead to the particle most probably

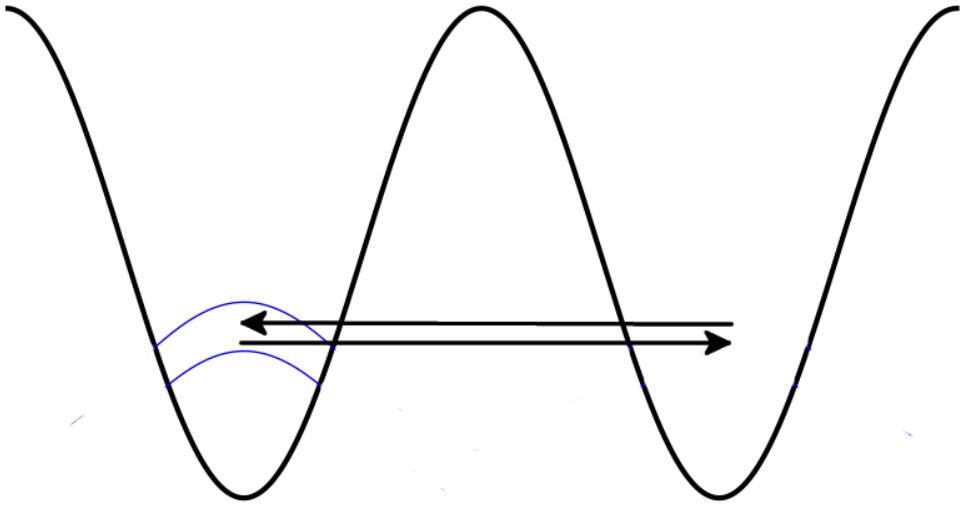

Figure 5.4: Double potential well (black). An instanton/anti-instanton path is shown with the arrows. The vacuum solution for the left hand well is split into two (blue).

being found in its lowest energy level, its vacuum solution, E_0:

$$E_0 = \frac{\hbar\omega}{2}. \tag{5.3}$$

Now let us consider what happens if the potential forms a double well, of the form shown in Figure 5.4. The propagator for paths where the particle starts and ends in the left hand well must also include paths where the particle travels to the right hand well as an instanton and travels back again as an anti-instanton. In fact, these instanton/anti-instanton movements could occur any odd number of times. The effect of including instantons in the propagator is that the previous vacuum solution is split into 2 (100), the true vacuum E_0 and a slightly higher energy level E_0', as shown in Figure 5.4, and given by

$$E_0 = \frac{\hbar\omega}{2} - \hbar R \cdot e^{-S/\hbar} \text{ and} \tag{5.4}$$

$$E_0' = \frac{\hbar\omega}{2} + \hbar R \cdot e^{-S/\hbar}, \tag{5.5}$$

where R is the ratio of the path integral including instantons to the constant path integral not including instantons. In fact, there are two true vacuums in this example, one corresponding to the particle in the left hand well and one in the right hand well,

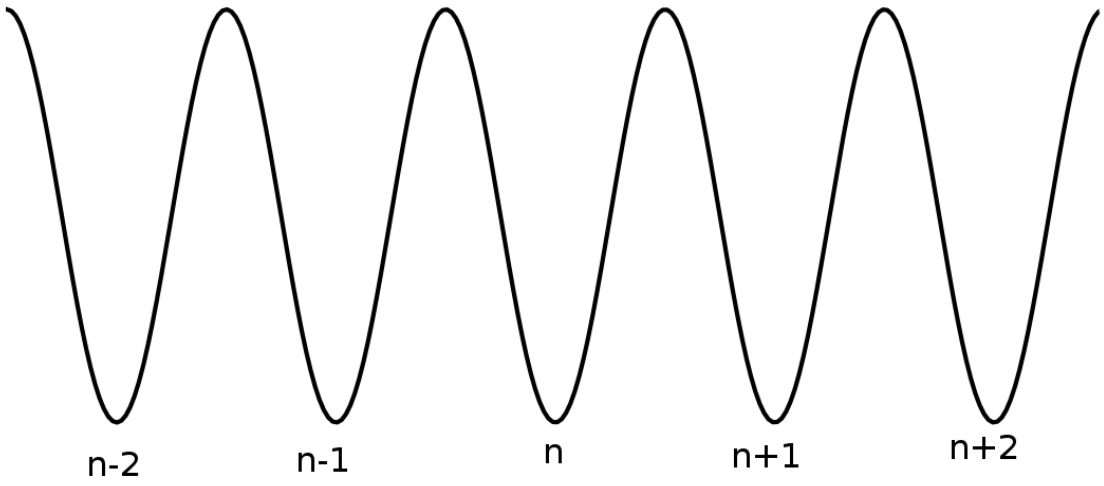

Figure 5.5: Schematic of the Lagrangian for the strong force.

both of which must be considered if we didn't already have knowledge (from the initial measurement) that the particle was in one well or the other.

5.4.2 Axions

The Lagrangian examined in the previous subsection had 2 true vacuums: the left hand well and the right hand well. The Lagrangian for the strong force has an infinite number of true vacuums (120). We can picture this as rather than having a double well we have a sine wave extending from negative to positive infinity within which each minimum can be labelled n, as shown in Figure 5.5. Moving from n to $n+1$ would change the phase of a wavefunction by an angle θ.

Since we now have instanton solutions between all of the different true vacuums, the effective Lagrangian $\mathcal{L}_E$ to be used in the propagator is given by (119):

$$\mathcal{L}_E = \mathcal{L} + i\theta \frac{g^2}{32\pi^2} F^{\alpha}_{\mu\nu} \bar{F}^{\alpha}_{\mu\nu}, \tag{5.6}$$

where g is a coupling constant and F is the gluon field strength tensor . The second term in this equation violates CP conservation, unless of course $\theta = 0$. However, as Roberto Peccei and Helen Quinn showed (120) CP invariance will arise naturally if the quarks interact with (and acquire their mass from) a new scalar field with $U(1)$ chiral symmetry. This in essence allows any value of θ to be treated as zero, since the terms associated with $\theta \neq 0$ are absorbed by a chiral rotation of the new field, which is of

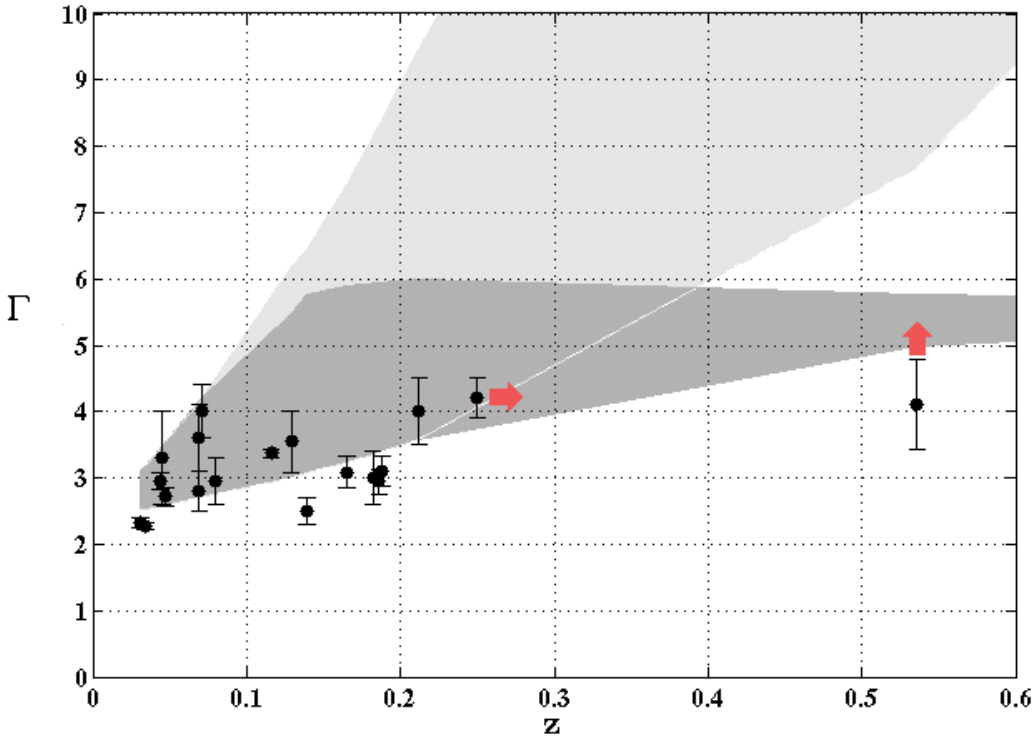

Figure 5.6: Observed spectral index Γ plotted against redshift z. Each point is the measured spectral index of a blazar at VHE. The light grey area shows the expected area for the data points given standard physics and the dark grey area shows the expected area for the data points in a scenario with photon-ALP mixing. Image credit (27).

course symmetric and therefore has no physical consequences (119). However, it was soon shown that instanton effects spontaneously break the $U(1)$ chiral symmetry that Peccei and Quinn had proposed. It is relatively straightforward to show (e.g. (73)) that generally[1] whenever a symmetry is broken it leads to particles called Nambu-Goldstone bosons, or pseudo-Nambu-Goldstone Bosons. In this case, Steven Weinberg (153) and Frank Wilczek (155) independently showed that Peccei and Quinn's proposal would lead to such a particle, dubbed an *axion*. Since under this model the quarks acquire their mass from interation with the axion field, the axion is also a Higgs boson (155).

5.4.3 Axion effects on γ-ray Spectra

It was pointed out in these papers that the axion would form a vertex with 2 photons. This means that in the presence of a B-field photons can oscillate into axions and vice versa (128). For QCD axions, discussed in the previous subsection, the photon-axion coupling constant g is related to the axion mass m_a, but this need not be the case for more generic axion-like particles (ALPs) (a recent review is given in (132)). Given current bounds on m_a, if axions exist then γ-ray photons could be expected to oscillate into axions. Broadly speaking, some γ-ray photons created in AGN jets are expected to convert into axions in the B-fields at and around the source, as we shall discuss in more detail later in the thesis. The mixed photon-axion beam then propagates through intergalactic space where the photons suffer the usual EBL attenuation but the axions do not (since they are not subject to photon-photon absorption). Photon-axion conversion will occur again when the beam enters the B-field of the Milky Way, resulting in some of the axions converting to γ-rays. In this way, a flux boost can be provided to the γ-ray spectrum since the effects of EBL absorption have been partially mitigated (139).

There is some evidence of such mitigation occuring. In 2012, a study (80) took a large sample of VHE detected blazars and first found a fit to the optically thin ($\tau < 1$) part of the spectrum of each object. This fit was then extrapolated into the optically thick ($\tau > 2$) regime and adjusted for EBL absorption. The lower limit EBL model (88) was used for this purpose. The result of this treatment showed that the data points in the optically thick regime scattered above the extrapolated fit with a significance of 4.2σ. This suggests that, even when a lower limit of the EBL is considered, there is more flux at the highest energies than would be expected from observations in the optically thin regime. The authors of the study note that photon-ALP mixing is one way to explain this anomaly.

One issue that has been raised is that this work has a potential inherent bias. The high energy part of an object's spectrum suffers from quite low photon numbers and there are natural Poisson fluctuations about the mean value at a given energy. It could be that if the object happens to fluctuate above its mean during the observation then it is detected but if the object happens to fluctuate below the mean it is too dim to be detected. This leads to a natural bias towards high energy data points that fluctuate above the mean.

[1] For an exception to this generalisation see e.g. (45)

Two arguments help answer this point, at least partially. Firstly, in (80) the authors re-run their analysis with the highest energy data point from each observation removed and find that the bias still persists at a 2.6σ level. Secondly, from the study's references, it can be seen that the spectra used do not have unusual residuals in the high energy part of the spectra.

A further hint at the existence of ALPs is given by studying the spectral index Γ of observed VHE sources. In general, we can say that the observed spectral index Γ_{obs} is related to the intrinsic spectral index Γ_{int} by (27)

$$\Gamma_{obs} = \Gamma_{int} + \tau. \tag{5.7}$$

Since τ increases with redshift, if there are no evolutionary effects in the redshift range in question then we expect Γ_{obs} to also increase with redshift. If photon-ALP mixing occurs at the source then the level of τ would be effectively reduced, and the increase of Γ_{obs} with redshift would be less. This is what was found in (27) and shown in Figure 5.6.

5.4.4 Phenomenology of Axions

In preparation for later work, I provide here the equations which describe photon-axion mixing. Following (128) and (79), we can take the Lagrangian for coupling between the electromagnetic field and the axion field as

$$\mathcal{L} = g\underline{E} \cdot \underline{B}a, \tag{5.8}$$

where $\underline{E}$ and $\underline{B}$ are the electric and magnetic fields respectively and a is the axion field.

Over a length s of plasma with approximately constant frequency and approximately constant magnetic field strength, the probability for a photon of energy E_γ to convert into an ALP (or vice versa) is[2]

$$P_0 = 2\left(\frac{\Delta_B}{\Delta_{osc}}\right)^2 \sin^2\left(\frac{\Delta_{osc} \cdot s}{2}\right). \tag{5.9}$$

[2]There is some disagreement as to the correct form of equation 5.9: see Ref (44) and references therein. If the choice here is incorrect then P_0 would increase by a factor of 2. This would not have a significant impact the work in this thesis.

Here Δ_B is a term relating to the transverse strength of the magnetic field B_T,

$$\Delta_B = 7.6 \times 10^{-2} \left(\frac{g}{5 \times 10^{-11}\ \mathrm{GeV}^{-1}} \right) \left(\frac{B_T}{10^{-6}\ \mathrm{G}} \right)\ \mathrm{kpc}^{-1}. \tag{5.10}$$

Δ_{osc} is the oscillation wave number,

$$\Delta_{osc} = \Big((\Delta_{CM} + \Delta_{pl} - \Delta_a)^2 + 4\Delta_B^2 \Big)^{\frac{1}{2}}\ \mathrm{kpc}^{-1}, \tag{5.11}$$

Δ_{CM} is the Cotton-Mouton term,

$$\Delta_{CM} = -4 \times 10^{-6} \left(\frac{B_T}{10^{-6}\ \mathrm{G}} \right)^2 \left(\frac{E_\gamma}{\mathrm{TeV}} \right)\ \mathrm{kpc}^{-1}, \tag{5.12}$$

Δ_{pl} is the plasma term,

$$\Delta_{pl} = 1.1 \times 10^{-10} \left(\frac{E_\gamma}{\mathrm{TeV}} \right)^{-1} \left(\frac{K}{10^{-3}\ \mathrm{cm}^{-3}} \right)\ \mathrm{kpc}^{-1}, \tag{5.13}$$

where K is the electron density of the plasma, and Δ_a is a term relating to the axion mass,

$$\Delta_a = 7.8 \times 10^{-3} \left(\frac{m_a}{10^{-8}\ \mathrm{eV}} \right)^2 \left(\frac{E_\gamma}{\mathrm{TeV}} \right)^{-1}\ \mathrm{kpc}^{1}. \tag{5.14}$$

Chapter 6

Information Theory and Model Comparison

6.1 Introduction

A major portion of this thesis is devoted to a comparison of different spectral fits to LAT data and simulated CTA data. Such comparisons are not straightforward, and this chapter discusses a method by which such comparisons can be made: the Akaike Information Criterion (AIC).

Let us imagine that we have some set of data drawn from a random variable X. These data could be anything, but for clarity and given the subject of this thesis, let us say they are a list of photon energies received from a coordinate on the sky. We want to know from what spectral energy distribution (SED) the photon energies were drawn. The general approach in the field is to proceed with model fitting: pick a spectral shape such as a power law or a log-parabola and attempt to find the best values for the free parameters to fit the data. Once the best fit for a particular model has been found we say that we know the likelihood, or more commonly the log-likelihood L, of a model given the data. (Finding the χ^2 of a model fit is usually not possible due to the relatively low photon numbers.) The problem then is how to compare multiple models in order to decide which is the best description and whether the difference between models is significant. The difference in likelihoods, or log-likelihood ratio, alone is not informative because even if a simple model in fact represented the true distribution, a more complex model (one with more free parameters) would be expected to provide a better likelihood simply by fitting noise. Therefore the test statistic (TS) of the log-likelihood ratio is employed: $-2 \ln \frac{L1}{L2}$. This TS is χ^2 distributed with degrees of freedom equal to the difference in free parameters of the two models, and therefore gives the confidence with which we can say

the difference in likelihoods was significant, and not a chance occurence.

The problem is the TS is only χ^2 distributed if the models are nested, i.e. one model is a special case of a more complex model and can be treated as a null-hypothesis. Determining if the difference in likelihoods is significant in non-nested models is difficult to compute (96). In this thesis we often want to compare the fit of a log-parabola to a broken power law and these two models are not nested.

In order to proceed we should realise that if we pick the wrong description of the true SED, say we use a log-parabola when the SED is a power law or we estimate the spectral index incorrectly, then we lose some information of the SED. If we had the complete information of the SED then we could perfectly predict, in a statistical manner, what photon energies we would observe from it. As we lose information our predictive ability worsens.

As we shall see in the following section, the amount of information lost when the probability density function $g(x)$ is used to represent the probability density function $f(x)$ is given by the Kullback-Leibler information quantity:

$$I_{KL} = \int \ln\left(\frac{f(x)}{g(x)}\right) f(x)dx. \tag{6.1}$$

In our example, f would be the true probability density function of the SED, and g is the probability density of the model we are using to represent it.

As it stands this isn't much help as g is unknown. However, in a series of papers Hirotogu Akaike demonstrated that the maximum likelihood of a model is a consistent, asymptotic estimator of the Kullback-Lieibler information of the model (see (25) and references therein). Akaike showed that the Kullback-Leibler information can be estimated as

$$-2L + 2k - K', \tag{6.2}$$

where k is the number of parameters in the model and K' is a constant that depends upon the true distribution.

K' is also unknown of course, but if we are interested in comparing candidate models it is evident that its value will be common to all of them and so we can discard it. Therefore we can define the Akaike Information Criterion (AIC) of a model m as

$$AIC_m = -2L_m + 2k_m. \tag{6.3}$$

Immediately we can say several things. Firstly, the larger the likelihood of a model given the data, the lower the AIC value for that model and therefore a lower AIC indicates a better model. Secondly, if two models have an equal likelihood, the model with more free parameters will have a worse AIC score. Thirdly, the difference in AIC score between multiple models easily distinguishes which one is better. If several models are being compared, it is practical to subtract the best AIC score from all of the models and quote this value:

$$\Delta AIC_m = AIC_m - AIC_{min}. \tag{6.4}$$

By definition, the best model of the group will have $\Delta AIC_m = 0$. A score of $\Delta AIC_m > 2$ is usually taken to be significant. This can be seen by comparing Equation 6.3 to a likelihood ratio test of models m and n, the TS of which,

$$-2 \ln \frac{m}{n}, \tag{6.5}$$

is asymptopically distributed as χ^2 (and therefore $\Delta AIC_m = 2$ corresponds to $\approx 85\%$ significance). In effect, the AIC test takes the number of free parameters into account when performing a likelihood ratio test with very little additional calculation. The AIC test is particularly well suited to work with LAT data, since the standard likelihood analysis program for the LAT, *gtlike*, gives the results of its fits in terms of likelihoods and the number of free parameters in a model is easily calculated. However, it should be noted that AIC tests are not part of a standard LAT analysis. The AIC test is a very general extension of the likelihood ratio test, and in this thesis it is applied to simulated CTA data as well as LAT data.

In the rest of the chapter we will examine the origins of the Kullback-Liebler information quantity and show a derivation of the AIC.

6.2 Information and Entropy

In order to understand where the Kullback-Liebler information quantity and the Akaike Information Criterion come from, we need to cover the basics of information theory. In 1948, Claude Shannon introduced the concept of information entropy (138). This quantity is a measure of how much uncertainty is inherent in a process. Imagine that there is a random variable X which has a probability density function $p(x)$. If $p(x)$ is fairly

uniformly distributed then there would be a lot of uncertainty in what the value of the next event drawn from the distribution would be and we would say that the system has high entropy. Conversely, if $p(x)$ was sharply peaked around a particular value then we would have a high expectation that the next value we draw would be close to the peak and we would say that the system has low entropy.

Let's start by considering a discrete probability function. We have a process with n different outcomes each with a probability p_i of occurring. As he wrote in his 1948 paper (138), Shannon demanded that the definition of entropy, H, statisfied the following 3 conditions:

1. H is continuous in p_i.

2. If all p_i are equal, $p_i = \frac{1}{n}$, then H is a monotonic increasing function of n. With equally likely events there is more uncertainty when there are more possible events.

3. If a choice [can] be broken down into two successive choices, the original H should be the weighted sum of the individual values of H. The meaning of this is illustrated in Figure 6.1. At the left we have 3 possibilities, $p_1 = \frac{1}{2}$, $p_2 = \frac{1}{3}$, $p_3 = \frac{1}{6}$. On the right we first choose between two possibilities each with probability $\frac{1}{2}$, and if the second occurs make another choice with probabilities $\frac{2}{3}$, $\frac{1}{3}$. The final results have the same probabilities as before. We require, in this special case, that

$$H\left(\frac{1}{2}, \frac{1}{3}, \frac{1}{6}\right) = H\left(\frac{1}{2}, \frac{1}{2}\right) + \frac{1}{2}H\left(\frac{2}{3}, \frac{1}{3}\right). \tag{6.6}$$

This leads to the entropy being defined as

$$H = -K \sum_{i=1}^{n} p_i \log p_i, \tag{6.7}$$

where K is a positive constant, which we shall neglect. The choice of base for the logarathim is likewise unimportant for the definition.

The information of a system can be defined as the negative of the entropy, $I = -H$, and therefore is a measure of the amount of predictability in the system:

$$I = \sum_{i=1}^{n} p_i \log p_i. \tag{6.8}$$

We can see from this that $I \leq 0$, with 0 being the maximum information we can have. If we consider the form of the above equation, we can see that it is the weighted sum of

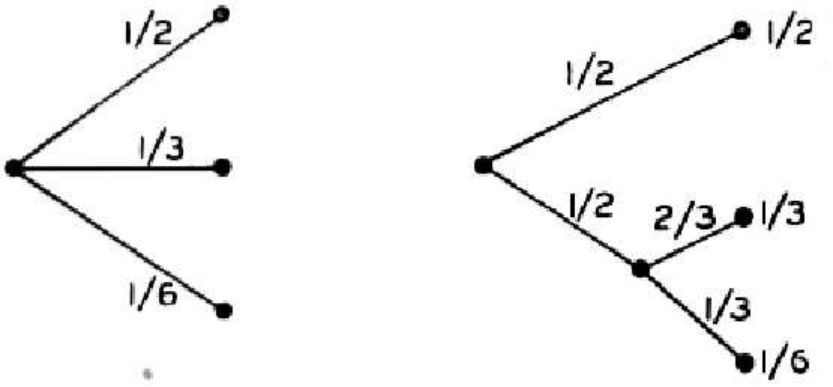

Figure 6.1: Decomposition of a choice from three probabilities. Image credit Claude Shannon (138).

$\log p_i$ and we shall call this term the *certainty*. Therefore, each element i contributes an amount to the total information based on its certainty and weighted by the probability of that element being drawn from the distribution. So, if an element is rarely drawn (p_i very low) its contribution to the information carries less weight than if an element is often drawn (p_i very high).

What happens if we try and use a model probability distribution q in place of p, perhaps because q is mathematically simpler to work with? For each element, the certainty we previously had, $\log p_i$, is degraded by a negative certainty $\log q_i$,

$$\text{Certainty Lost}_i = \log p_i - \log q_i = \log \frac{p_i}{q_i}. \tag{6.9}$$

Just as p_i weights the contribution of each element's certainty to the total information, so too it weights the contribution of each element's certainty lost to the total information lost:

$$\text{Information Lost} = \sum_{i=1}^{n} p_i \log \frac{p_i}{q_i}. \tag{6.10}$$

Note the use of p_i in Equation 6.10. This makes sense if we consider an element i which has $p_i = 0$, i.e. it does not contribute to the information at all. It therefore does not matter if q_i approximates the element very badly, it will not affect the information we have on the true distribution.

While the preceding discussion was not very rigorous, Equation 6.10 was proved by Solomon Kullback and Richard Liebler in 1951 (92). The quantity described in Equation 6.10 is therefore termed the Kullback-Liebler information quantity, I_{KL}. Amongst

its properties is that $I_{KL} \geq 0$ which, given that $I \leq 0$, demonstrates that I_{KL} is negative information, or information loss.

Equations 6.8 and 6.10 can of course be generalised to continuous distributions:

$$I = \int p(x) \log p(x) dx, \tag{6.11}$$

$$I_{KL} = \int p(x) \log \frac{p(x)}{q(x)} dx. \tag{6.12}$$

6.3 Derivation of the AIC

We now ready to derive the AIC. To start with, we give the Taylor expansion of a multivariate function $g(y, z)$ around (a, b):

$$\begin{aligned} g(y,z) =& g(a,b) + g_y(a,b)(y-a) + g_z(a,b)(y-b) + (y-a)' g_{yz}(z-b) + \\ & \frac{1}{2!}\left(g_{yy}(a,b)(y-a)^2 + g_{zz}(a,b)(z-b)^2\right), \end{aligned} \tag{6.13}$$

where subscripts represent a derivative with respect to that value and the prime indicates the transpose.

We apply this to the value of I_{KL} between a model defined by the true parameter vector, θ^*, and the maximum likelihood estimate value in a k-dimensional parameter space, $\hat{\theta}_k$. (We start here the convention of using * to denote a true parameter and $\hat{}$ to denote an estimated parameter.)

$$g = I_{KL}(\theta^*, \hat{\theta}_k) = \int \ln \frac{f_{\theta^*}}{f_{\hat{\theta}_k}} f_{\theta^*}. \tag{6.14}$$

We expand around the position of the parameter vector $\hat{\theta}_k$ in the parameter space of θ^*. In this case, y and z are both axes of the parameter space of θ^*: $y = \theta_m$, $z = \theta_n$ and a and b are both components of the vector $\hat{\theta}_k$: $a = \hat{\theta}_k \cdot \theta_m$, $b = \hat{\theta}_k \cdot \theta_n$.

Since $\hat{\theta}_k$ is the value for θ_k which minimises the information loss, or at least close to it, we can treat it as a turning point of the function I_{KL} and therefore all first derivatives of I_{KL} at this point are zero: $g_y = g_z = 0$. Furthermore, since $\hat{\theta}_k$ will be close to θ^*,

$$\ln \frac{f_{\theta^*}}{f_{\hat{\theta}_k}} f_{\theta^*} \approx \ln 1 f_{\theta^*} = 0, \tag{6.15}$$

and therefore

$$g(a, b) = 0. \tag{6.16}$$

Therefore, to first order in $(\theta_* - \hat{\theta}_k)$ we have

$$I_{KL}(\theta^*, \hat{\theta}_k) = (\theta_* - \hat{\theta}_k)' I_{yz} (\theta_* - \hat{\theta}_k), \tag{6.17}$$

where

$$I_{yz} = \ln \frac{f_{\theta^*}}{f_{\hat{\theta}_k}} \int \left[\left(\frac{\partial f}{\partial \theta_m} \frac{1}{f} \right) \left(\frac{\partial f}{\partial \theta_n} \frac{1}{f} \right) \right]_{\theta=\theta^*} f_{\theta^*} dx \tag{6.18}$$

is the $(m, n)^{th}$ element of the Fisher information matrix and a dash indicates a transpose. As Akaike showed (25), this derivation remains valid for a larger number of dimensions.

Ultimately we are trying to find the expected value of $I_{KL}(\theta^*, \hat{\theta}_k)$ when we use our maximum likelihood estimate $\hat{\theta}_k$. Since $\hat{\theta}_k$ is restricted to a parameter space of dimension k, the difference between the true value of the parameter and our estimate is given by the difference between the true value and the true value in the restricted space k **plus** the difference between the true value in the restricted space k and what we estimate this value to be:

$$\theta^* - \hat{\theta}_k = (\theta^* - \theta_k^*) + (\theta_k^* - \hat{\theta}_k), \tag{6.19}$$

and therefore

$$I_{KL}(\theta^*, \hat{\theta}_k) = (\theta^* - \theta_k^*)' I_{yz} (\theta^* - \theta_k^*) + (\theta_k^* - \hat{\theta}_k)' I_{yz} (\theta_k^* - \hat{\theta}_k) \tag{6.20}$$

$$= A + B. \tag{6.21}$$

We can see from this that A is a bias parameter, representing the information lost due to the model we are using having a different parameter space to the true distribution. B is a variance parameter, representing the information lost due to not being able to estimate the most likely parameter perfectly with the given data. As we said, the AIC is the expected information loss:

$$AIC = E[I_{KL}(\theta^*, \hat{\theta}_k)] = E[A] + E[B]. \tag{6.22}$$

$B = (\theta_k^* - \hat{\theta}_k)' I_{yz} (\theta_k^* - \hat{\theta}_k)$ can be rewritten as $\sum_{i=0}^{k} I_{y_i z_i} (\theta_i^* - \hat{\theta}_i)^2$ which we can see is a χ^2 distribution with k degrees of freedom. Therefore

$$E[B] = k. \tag{6.23}$$

Finding E[A] is a little harder; we cannot use the same treatment as for E[B] since θ_k^* is of rank k while θ^* is of the higher rank of the unrestricted parameter space, K. We

therefore use the following theorem (first proved, as far as I know, in (152) but which can be seen more explicitly in (16)):
$-2\ln\frac{L(\theta_k^*|\underline{x})}{L(\theta^*|\underline{x})}$is asymptotically distributed as $\chi'^2_v(\delta)$, that is a non-central χ^2 distribution with $v = K - k$ degrees of freedom and non-centrality parameter

$$\delta = (\theta^* - \theta_k^*)' I_{yz} (\theta^* - \theta_k^*). \tag{6.24}$$

We can therefore say that

$$E[\chi'^2_v(\delta)] = \delta + v, \tag{6.25}$$

$$\delta = E[\chi'^2_v(\delta)] - v \tag{6.26}$$

$$= E\left[-2\ln\frac{L(\theta_k^*|\underline{x})}{L(\theta^*|\underline{x})}\right] - v \tag{6.27}$$

$$\approx -2\ln\frac{L(\hat{\theta}_k|\underline{x})}{L(\theta^*|\underline{x})} - v \tag{6.28}$$

$$= -2\ln L(\hat{\theta}_k|\underline{x}) + 2\ln L(\theta^*|\underline{x}) + k - K. \tag{6.29}$$

We therefore end up with the following expression for the AIC:

$$AIC = -2\ln L(\hat{\theta}_k|\underline{x}) + 2k + 2\ln L(\theta^*|\underline{x}) - K, \tag{6.30}$$

however, for a given data set the last two terms depend only on the parameters of the true distribution and not on the parameters of the model. Therefore, these terms are usually discarded since in model comparison they are irrelevant, leaving us with our final expression:

$$AIC = -2\ln L(\hat{\theta}_k|\underline{x}) + 2k. \tag{6.31}$$

6.4 Example AIC test using LAT data of 3C 273

In this section I will give a brief example to illustrate model selection using the AIC. A broken power law (BPL) and a log-parabola (LP), are fitted to roughly 1.5 years of LAT data of the blazar 3C 273. These models are non-nested and cannot be directly compared using a likelihood ratio test. We'll discuss more about the shape of these models and their physical motivation in the next chapter, for the moment they just serve as an example for model comparison.

The data and the 2 model fits are shown in Figure 6.2. After minimisation using the standard tool *gtlike*, the BPL model has a log-likelihood given the data of

$$L_{BPL} = -694057.8. \tag{6.32}$$

The LP model has a log-likelihood of

$$L_{LP} = -694059.6. \tag{6.33}$$

The BPL model has a larger log-likelihood and might therefore be thought to be the better description of the data. However, we should take the number of free parameters in the model into account using the AIC value of each model. The BPL model has 4 free parameters (normalisation constant, break energy and 2 spectral indices) while the LP has 3 free parameters (normalisation constant, spectral index and curvature parameter). Therefore we calculate the AIC values as

$$AIC_{BPL} = -2 \cdot 694057.8 + 2 \cdot 4 = 1388123.7 \tag{6.34}$$

$$AIC_{LP} = -2 \cdot 694059.6 + 2 \cdot 3 = 1388125.2. \tag{6.35}$$

We can see that the difference in AIC of the two models is

$$\Delta AIC_{BPL,LP} = 1.5, \tag{6.36}$$

so the difference between models is not significant: neither the BPL nor the LP model is a significantly better description of the data. Having introduced these concepts we can now move on to applying model comparison to LAT data.

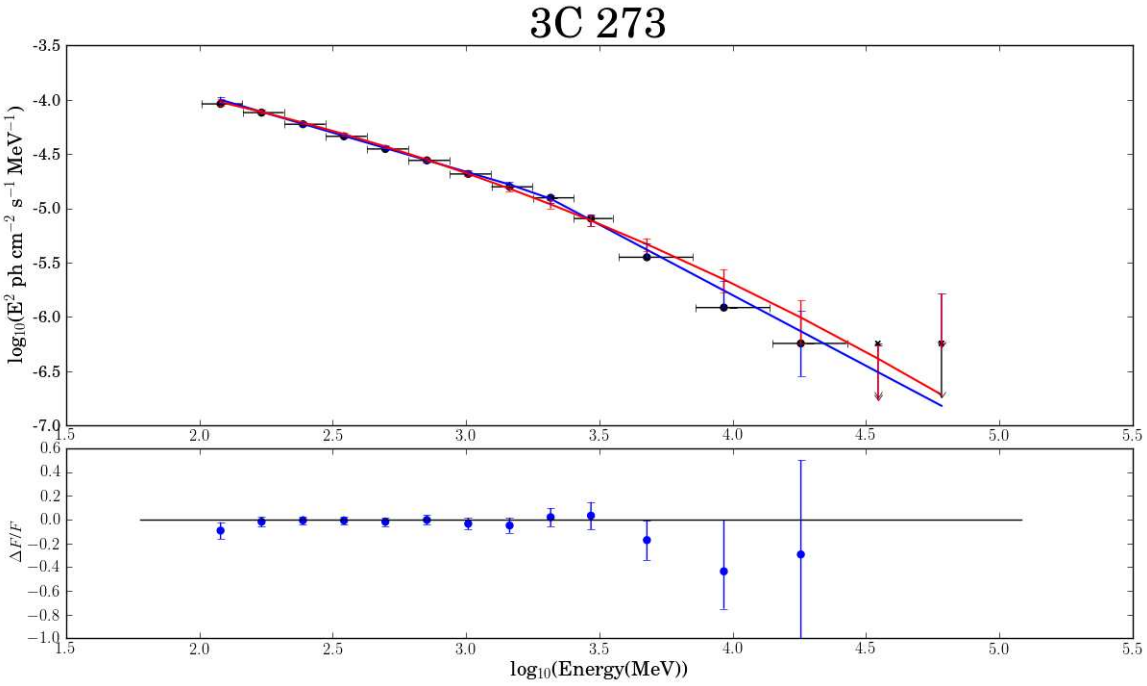

Figure 6.2: Black points are aperture photometry data for 3C 273. In blue is the broken power law model fitted to the data and red is the log-parabola model fitted to the data. Error bars on the models are 68% confidence intervals. Underneath are shown the residuals to the broken power law fit.

Chapter 7

Spectral Properties of Fermi blazars I

7.1 Introduction

In this chapter I shall present a study into the spectral shape of blazars using the *Fermi*-LAT. Firstly, I will provide the motivation for the study and the analysis methods used, then I will present the results and discuss them. For the following discussion it is necessary to define 3 spectral shapes: a simple power law (SPL), broken power law (BPL) and log-parabola (LP). I will simply give the mathematical definitions at this point, the motivation for SPL spectra of blazars was given in Chapter 3 and the physical motivation of BPL and LP spectra will be given in the following section.

An SPL is defined as

$$\frac{dN}{dE} = k\left(\frac{E}{E_0}\right)^{-\Gamma}, \tag{7.1}$$

where dN/dE is the differential photon flux as a function of photon energy, k is a normalisation constant, E_0 is a normalisation energy, which we fixed at 0.5 GeV for this study, and Γ is the spectral index.

A BPL, which describes a sudden change in the spectral index of a power law from Γ_1 to Γ_2 at a break energy E_b, is defined as

$$\frac{dN}{dE} = \left\{ \begin{array}{lll} k\left(\frac{E}{E_b}\right)^{-\Gamma_1} & \text{if} & E < E_b \\ k\left(\frac{E}{E_b}\right)^{-\Gamma_2} & \text{if} & E \geq E_b \end{array} \right\}. \tag{7.2}$$

Finally, an LP, which describes constant curvature across the spectrum, is defined as

$$\frac{dN}{dE} = k\left(\frac{E}{E_0}\right)^{-\Gamma-\beta\log(\frac{E}{E_0})}, \tag{7.3}$$

where β defines the amount of curvature and E_0 is again fixed at 0.5 GeV.

7.2 Spectral Shape of blazars in the *Fermi* energy regime

As we saw earlier, from EGRET observations it has been known for some time that blazar spectra can be reasonably well described by an SPL over several decades of energy in the HE regime. The launch of *Fermi*, with the LAT's improvement in effective area and energy resolution, allows a search for deviations from an SPL, for example curvature or sharp breaks. There are several scientific motivations for doing so. Testing emission models often involves fitting to multiwavelength data, and better fits to HE data allows for more accurate modelling. Understanding the spectral shape is also cruicial for extrapolation of HE spectra into the VHE regime, where the difference between the extrapolated and observed spectra can provide information on the amount of EBL absorption. Finally, as we shall see, specific models for the γ-ray emission mechanism or location can lead to testable features in the HE spectrum.

7.2.1 Spectral breaks and curvature

From observations published in 2009 (1) and 2010 (6), the *Fermi* team concluded that the spectra of FSRQs and LBLs deviated from SPL spectra. For several objects, including the bright FSRQ 3C 454.3, a BPL spectrum with a sharp break was a better description of the data than a smoothly curved LP spectrum.

As the authors noted, this result was somewhat surprising, for several reasons. The double-peak shape of the multiwavelength SED suggested a curved spectrum such as an LP might well have described the HE spectra. Observations in the X-ray waveband in particular had shown spectra well described by an LP (101) and from what we saw Chapter 3 we could well expect the Compton emission of this population of electrons to have the same shape. An LP spectrum could be adequately explained assuming leptons in the jet undergo stochastic acceleration processes whereby the probability for an electron to be accelerated at a shock front is less when the electron has more energy (see references (101), (150) and references therein).

On the other hand, a sharp break as described by a BPL was somewhat unexepected and hard to explain. In a leptonic scenario the spectral shape of the Compton emission is defined by both the spectrum of the low energy photons and the electrons that upscatter them. Simply having a BPL spectrum of electrons is not enough to produce a

BPL inverse Compton spectrum, in fact BPL electron spectra are quite common in the literature (e.g. (156)) due to high energy electrons escaping from the emission region. In the case of 3C 454.3, the authors did conclude that the break was likely due to the energy distribution of the emitting electrons however a later publication (61) pointed out that this scenario predicted a correlation between the spectral indices in the optical and γ-ray wavebands, which was not observed. We therefore explore several other possible causes of BPL spectra: the double-absorber model and the two component model.

7.2.2 Double-Absorber Model

Juri Poutanen and Boris Stern proposed (124) (hereafter PS10) that the observed spectral breaks could be due to absorption of γ-rays above the break energy by recombination line photons originating in the blazar's BLR. For such a mechanism to occur, the γ-ray emission region would need to be located within the radius of the BLR. PS10 used a simple photoionisation model of the BLR (93) and the resulting emission spectrum between 1 eV and 100 keV to calculate the opacity of the BLR to γ-rays as a function of energy. This emission spectrum saw 2 sharp jumps in intensity, the first at 13.6 eV due to He recombination and the second at 54.4 eV due to H recombination. These jumps in intensity lead to 2 corresponding increases in the opacity of the BLR to γ-rays at the points where the γ-rays had enough energy to produce e^-/e^+ pairs with the recombination line photons and the model is therefore called the 'double-absorber' model. These jumps in opacity occurred over 4-7 GeV and 19.2-30 GeV in the object's rest frame. A simplification in PS10 allowed these jumps to be treated as occurring at 4.8 GeV and 19.2 GeV.

We will now briefly show how the double-absorber model gives rise to breaks in the spectrum. As can be seen in PS10, where there are sharp jumps in opacity the optical depth can be approximated as

$$\tau_{\gamma\gamma} = \tau_{eff} \ln E, \tag{7.4}$$

where τ_{eff} is an effective optical depth, which is constant. Therefore if the intrinsic spectrum is an SPL which (neglecting the normalisation constant and normalisation energy for clarity) has the form

$$F(E) = E^{-\Gamma}, \tag{7.5}$$

then above the threshold of absorption the spectrum becomes

$$F(E) = E^{-\Gamma} e^{-\tau_{eff} \ln E}. \tag{7.6}$$

We can see that this leads to a change in spectral index by a couple of straightforward steps:

$$F(E) = E^{-\Gamma} \left(e^{\ln E}\right)^{-\tau_{eff}} \tag{7.7}$$

$$= E^{-\Gamma} E^{-\tau_{eff}} \tag{7.8}$$

$$= E^{-(\Gamma+\tau_{eff})}, \tag{7.9}$$

Therefore the double-absorber model predicts that γ-rays with an SPL spectrum that travel through the BLR will acquire 2 breaks, at energies around 4-7 GeV and 19.2-30 GeV. The conclusion of PS10 is that the observed spectra are well described by the double-absorber model, although as the authors note the fits using the double-absorber model are of the same quality as the BPL fits. In a subsequent paper (144), the authors concluded that the intrinsic spectrum of 3C 454.3 is an LP[1] with 2 breaks at these energies.

7.2.3 Two Component Model

Justin Finke and Charles Dermer (61) (hereafter FD10) fitted the SED of 3C 454.3 using a multi-component leptonic model (53) with the emission region within the radius of the BLR at a distance of ≈ 0.1 pc from the central black hole. They concluded that the observed spectrum could be explained if emission from both the accretion disc and BLR were fully considered. In this model, the emission above the break energy was due to inverse Compton scattering of photons that were emitted from the disc and reprocessed by the BLR. The reprocessed photons still have approximately the same energy with respect to the central black hole as when they were emitted from the disc. However, since the γ-ray emission region is within the radius of the BLR the reprocessed photons will now be scattered head on rather than approaching the emission region from behind. This geometric effect means that this population is scattered in the Klein-Nishina regime. In this model, the break energy should remain approximately stable in energy and exist

[1]The authors used a log-normal but noted that it is essentially the same as a LP but in a different representation.

at least over the timescale of several months, since the emission region would need to emerge from the BLR in order for the break to cease.

7.3 Data Analysis

In the rest of the chapter, I present the study. LAT data were analysed for 9 blazars which were selected in PS10 for their brightness in this waveband and their freedom from contaminating sources. This study was performed after PS10, meaning that more data had been collected for all of the objects. Additionally, the data analysis methods employed in this work offer several improvements over those of PS10, as detailed in subsection 7.3.4. The 9 objects analysed are shown in Table 7.1. The objects spectral shapes were investigated to determine if:

- The objects were best described by an SPL, BPL or LP.
- If the best fitting spectral shape for each model is stable or if it change over time and tested if the break energy of a BPL fit remains stable over time (which is a prediction of both the double-absorber model and to a lesser extent the two component model)
- If the spectra were consistent with the 2 energy breaks predicted by the double-absorber model.

7.3.1 Event Selection and Background Modelling

All photons that arrived within a 15° radius of the target and reconstructed to be event class 3 (diffuse) or better were examined using the the *Fermi* Science Tools v9r23p1 and the P6_V3_DIFFUSE version of the *Fermi*-LAT instrument response function (IRF) (14). Any photons received when *Fermi*'s zenith angle was $< 105^{\circ}$ were discarded to avoid $\gamma-$ray contamination from the Earth. An upper energy limit of $100\ \mathrm{GeV}$ was used. The lower energy limit was typically a few hundred MeV, but varied for reasons discussed in the following subsections.

The models constructed for use with *gtlike* incorporated point sources in the region of interest with parameters fixed to those in the *Fermi*-LAT 1 Year Catalog (4). Galactic and extragalactic emission were accounted for using the standard models, which are

gll_iem_v02 and isotropic_iem_v02 respectively[2], with the normalisations left as free parameters.

7.3.2 Model Comparison

For each object, the likelihood of the data coming from an SPL, BPL and LP model were calculated using the NEWMINUIT routine in *gtlike*. These 3 spectral shapes were then compared using an AIC test to determine which, if any, was a significantly better description of the data.

7.3.3 Truncating the energy range

Searching for a break energy, caused by an absorption feature or otherwise, can require performing an analysis only over a truncated energy range. This is because, from a priori knowledge of the SED's shape, over a wide enough energy range the HE spectrum will display curvature and this is especially true around the peak in the SED. Imagine trying to fit a BPL to a curved spectrum that also had a break caused by the onset of absorption (as in the case of (144)). The break energy found by the fit would try to describe both the actual break caused by absorption and the curvature in the spectrum. Therefore, if the curvature was great enough the break energy returned by the fit would not be the energy of the onset of absorption. In this way, interesting physics could be missed or misinterpreted.

It was therefore necessary to determine if the spectral curvature in our objects would be small enough to allow breaks to be correctly identified or if some truncation of the energy range would be needed. To this end Monte Carlo simulated observations were performed using *gtobssim* of an object with an LP spectrum of $\Gamma = 2.11$ and $\beta = 0.12$ which yields a peak energy of $\approx 250\ \mathrm{MeV}$. These parameters were chosen to match the greatest curvature found in the observational sample. An absorption feature was introduced to this spectrum corresponding to a change in spectral index of $\Delta\Gamma = 0.5$ at $1.8\ \mathrm{GeV}$ in the observer frame. If the peak energy was chosen as the low energy threshold for analysis, the correct break energy was identified correctly ($1.7 \pm 0.2\ \mathrm{GeV}$). However, if the low energy threshold was placed below the spectral peak, the break energy was frequently misidentified and in half of the simulations the estimated break energy was incorrect by

[2]http://fermi.gsfc.nasa.gov/ssc/data/access/lat/BackgroundModels.html

more than a standard error. Additionally, if the threshold energy was increased from the peak energy in $50\ \mathrm{MeV}$ steps the break energy identified remained stable but if the threshold energy was decreased from the peak energy the break energy varied widely (typically by more than a standard error between steps) demonstrating the degeneracy in trying to fit a BPL to the highly curved spectrum about the peak energy. The absorption feature was then removed from the simulated spectra. In this case a threshold of 50 or $100\ \mathrm{MeV}$ above the peak energy was sometimes needed to find a stable break.

There are 2 important points can be made from these simulations. Firstly, if there is a break in the spectrum it can be correctly identified provided the energy threshold is above the peak energy. Secondly, if the energy threshold is above the peak energy then the break energy will be stable if the threshold is increased by $50\ \mathrm{MeV}$. Therefore, for each object only photons above the peak energy were analysed. The spectral peaks for most objects in the sample had been previously estimated from multiwavelength data (5). However, any observational result has uncertainties and it was also possible that the peak energies had shifted with time. To address this, a BPL was fitted to the spectra of each object, first using the peak energy as the low energy threshold and then increasing this by $50\ \mathrm{MeV}$. If the break energies were not consistent the threshold was repeatedly increased by $50\ \mathrm{MeV}$ until a stable break energy was found. The truncated energy range found in this manner was then used throughout the study. In all cases the low energy threshold was well below the break energies predicted by the double-absorber model and so the truncation did not prevent the testing of this model in any case. Since only bright sources were examined in this study, the loss of photon data was not too detrimental, especially since the LAT's point spread function at low energies is relatively poor and thus the low energy range has a poorer signal-to-noise ratio. In the case of PKS 2022-07 the peak energy estimated in reference (5) was *not* used since it could not be estimated from multiwavelength data but was instead estimated using an emprical relationship between an object's spectral index and peak frequency:

$$\ln\left(\nu_{peak}\right) = -4.0 \cdot \Gamma + 3.16. \tag{7.10}$$

For this object all of the data above $100\ \mathrm{MeV}$ was fitted with an LP to get the inital estimate of the peak energy, which was determined as $290\ \mathrm{MeV}$.

7.3.4 Energy ranges for evaluating the DA model

As we saw, the double-absorber model predicts 2 breaks in the spectrum of an object, the first between 4-7 GeV and the second between 19.2-30 GeV. However, the standard *Fermi* analysis tool *gtlike* does not support such a spectral shape. In PS10 simplifications were made to the IRF and background modelling, and the double-broken-power law shape as well as a single-BPL were fitted to binned counts using a simple χ^2 fit. However, this approach degraded the performance of the fits and the uncertainties on the break energy of their BPL fits were on average 50% worse than those found using the standard analysis (6).

In order to use the standard *gtlike* tool, the data from each object were split it into a low energy range and a high energy range, each of which could be fitted with a BPL. The energy separating the 2 ranges was chosen as the middle of the 2 predicted breaks in the observer frame. First, the low energy range was fitted with a BPL and it was then checked whether the break was significant by testing it against an SPL null-hypothesis (which is straightforward to perform since the SPL is a special case of the BPL). The consistency of the observed break energy with that predicted by the double-absorber model (both 4.8 GeV and the wider 4-7 GeV range) was then tested. All of the data above the observed break energy were then taken to comprise the high energy set. These data were given a similar treatment: a BPL was fitted and the break's significance was tested against an SPL null-hypothesis and the energy tested for consistency with the predictions of the double-absorber model.

7.3.5 Epochs for analysing the stability

As discussed above, the double-absorber model and the two component model both make predictions regarding the stability of spectral shapes and features. More generally, if the spectral shape is determined by physical parameters that can vary on short timescales (injected electron spectrum, B-field strength, etc.) then it would be expected to vary with time. With this in mind, the data from each object were split into 2 equal time bins, epoch 1 and epoch 2, and these epochs were analysed seperately to find the spectral shape that best described them. The best spectral shapes of each epoch and the break energies of the BPL fits were compared to see if they were consistent between the

Table 7.1: Simple Power Law Fits

Object	Index Γ	ΔAIC_{min}
3C 454.3	2.485 ± 0.006	653.5
PKS 1502+106	2.41 ± 0.02	78.1
3C 279	2.41 ± 0.01	70.8
PKS 1510-08	2.48 ± 0.01	35.6
3C 273	2.76 ± 0.01	32.9
PKS 0454-234	2.34 ± 0.02	49.3
PKS 2022-07	2.52 ± 0.04	7.8
TXS 1520+319	2.42 ± 0.01	41.6
RGB J0920+446	2.35 ± 0.02	43.1

The best fitting parameters for simple power law fits to each object as described in Equation 7.1. ΔAIC_{min} is the difference in AIC between the simple power law fit to the object and the best fit out of simple power law, broken power law and log-parabola, a value of 0 indicating a simple power law is the best fit to the data and a value > 2 indicating either a broken power law or a log-parabola is a significantly better fit to the data.

2 epochs.

7.4 Results

7.4.1 Testing For Deviation from a Simple Power Law

The spectra of all of our sources show significant deviation from an SPL. Tables 7.1, 7.2, and 7.3 show the parameters of the best fit to each source using an SPL, BPL and LP fit respectively along with the results of the AIC test. For illustrative purposes, the fits for each source are shown along with aperture photometry data in Figures 7.1 - 7.3.

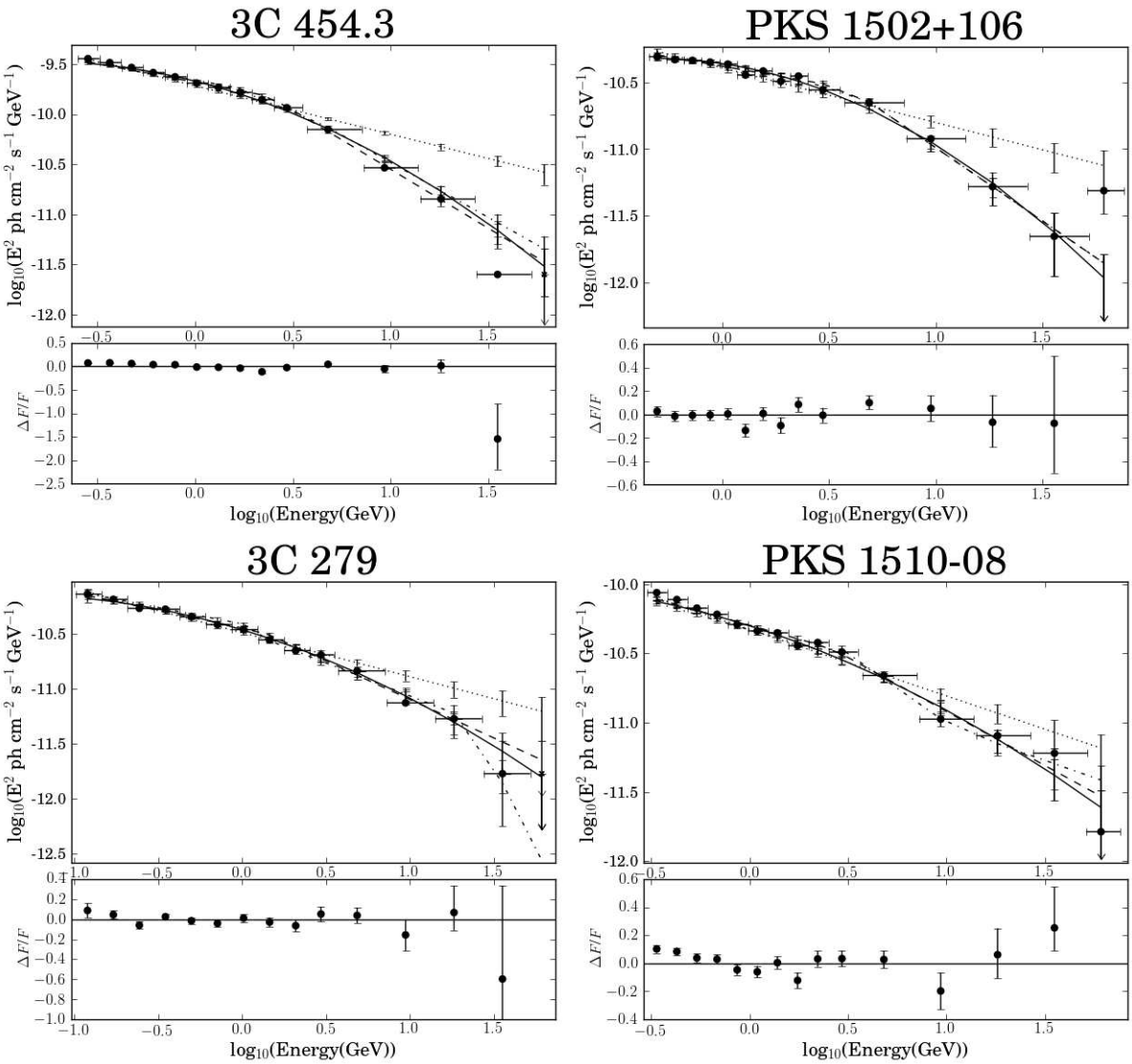

Figure 7.1: Aperture photometry data for each source along with the following spectral shapes from a maximum likelihood fit to the full dataset: simple power law (dotted), broken power law (dashed), log-parabola (solid), and double-absorber (dot-dashed). Error bars are 68% confidence intervals for each model, see (15). Residuals ((Observed Flux - Model Flux)/Observed Flux) for the best fitting spectral shape are shown underneath each plot. Energies are in the observer frame.

Table 7.2: Broken Power Law Fits

Object	Break Energy E_b (GeV)	Index1 Γ_1	Index 2 Γ_2	ΔAIC_{min}
3C 454.3	$4.5^{+0.2}_{-0.3}$	2.375 ± 0.007	3.18 ± 0.03	0
PKS 1502+106	$11.2^{+1.1}_{-0.8}$	2.28 ± 0.02	3.1 ± 0.1	2.6
3C 279	$2.1^{+0.2}_{-0.3}$	2.32 ± 0.02	2.70 ± 0.04	6.6
PKS 1510-08	$3.5^{+0.6}_{-0.5}$	2.40 ± 0.02	2.81 ± 0.06	0
3C 273	$2.2^{+0.2}_{-0.5}$	2.72 ± 0.02	3.4 ± 0.1	0
PKS 0454-234	$2.6^{+0.5}_{-0.4}$	2.12 ± 0.04	2.61 ± 0.05	1.8
PKS 2022-07	$4.0^{+1.8}_{-0.7}$	2.34 ± 0.07	2.8 ± 0.1	0
TXS 1520+319	$4.7^{+1.2}_{-0.6}$	2.36 ± 0.02	2.76 ± 0.06	0
RGB J0920+446	16^{+2}_{-5}	2.3 ± 0.1	3.6 ± 0.4	13.2

The best fitting parameters for broken power law fits to each object as described in Equation 7.2. E_b is in the object's rest frame. ΔAIC_{min} is the difference in AIC between the broken power law fit to the object and the best fit out of simple power law, broken power law and log-parabola, a value of 0 indicating a broken power law is the best fit to the data and a value > 2 indicating a log-parabola is a significantly better fit to the data.

7.4.2 Testing For Energy Breaks Caused By BLR Pair-Production

Splitting the dataset for each object into a low energy and high energy set allows the predictions of the double-absorber model to be tested . After splitting the data in this way, the results for BPL fits to each source and the significance of the improvement they offer over an SPL fit are shown in Tables 7.4 (low energy sets) and 7.5 (high energy sets). Plots of the likelihood of a BPL with a given break energy fitting the data are shown in Figures 7.4 (low energy sets) and 7.5 (high energy sets). The regions where the double-absorber model predicts breaks to occur are shown as shaded boxes.

When examining the low energy sets, in 7 of the 9 objects a BPL is found to be a better description than an SPL to $> 99\%$ significance. However, in most of the objects, the break energy does not lie within the energy region predicted by the double-absorber model.

Fits to the high energy set of most objects were not significantly improved by using

Table 7.3: Log-Parabola Fits

Object	Index Γ	Curvature β	ΔAIC_{min}
3C 454.3	2.307 ± 0.009	0.133 ± 0.006	12.8
PKS 1502+106	2.02 ± 0.04	0.16 ± 0.02	0
3C 279	2.36 ± 0.01	0.071 ± 0.009	0
PKS 1510-08	2.35 ± 0.03	0.07 ± 0.01	2.4
3C 273	2.76 ± 0.02	0.07 ± 0.01	1.5
PKS 0454-234	2.11 ± 0.04	0.12 ± 0.02	0
PKS 2022-07	2.27 ± 0.09	0.11 ± 0.04	0.4
TXS 1520+319	2.38 ± 0.01	0.05 ± 0.01	9.3
RGB J0920+446	2.26 ± 0.03	0.10 ± 0.02	0

The best fitting parameters for log-parabola fits to each object as described in Equation 7.3. ΔAIC_{min} is the difference in AIC between the log-parabola fit to the object and the best fit out of simple power law, broken power law and log-parabola, a value of 0 indicating a log-parabola is the best fit to the data and a value > 2 indicating a broken power law is a significantly better fit to the data.

a BPL. Of the 3 objects that do reject the SPL to $> 99\%$ significance, the break energy is again not found in the region predicted by the double-absorber model. It is worth noting that in PS10 evidence of absorption is found for 7 objects in which we found an SPL to be an adequate description.

7.4.3 Testing the Stability Of Spectra

5 of the 9 sources were best fitted by different spectral shapes in each epoch (i.e. the best fit changed from an LP to a BPL or vice versa), as shown in Table 7.6. For the BPL fits, the break energies in 6 sources were found to differ over the 2 epochs by more than a standard deviation, and in 3 sources they were found to differ by more than 2 standard deviations. This is more deviation than expected from statistical variation alone, but with a sample size of only 9 sources the evidence should be taken with caution.

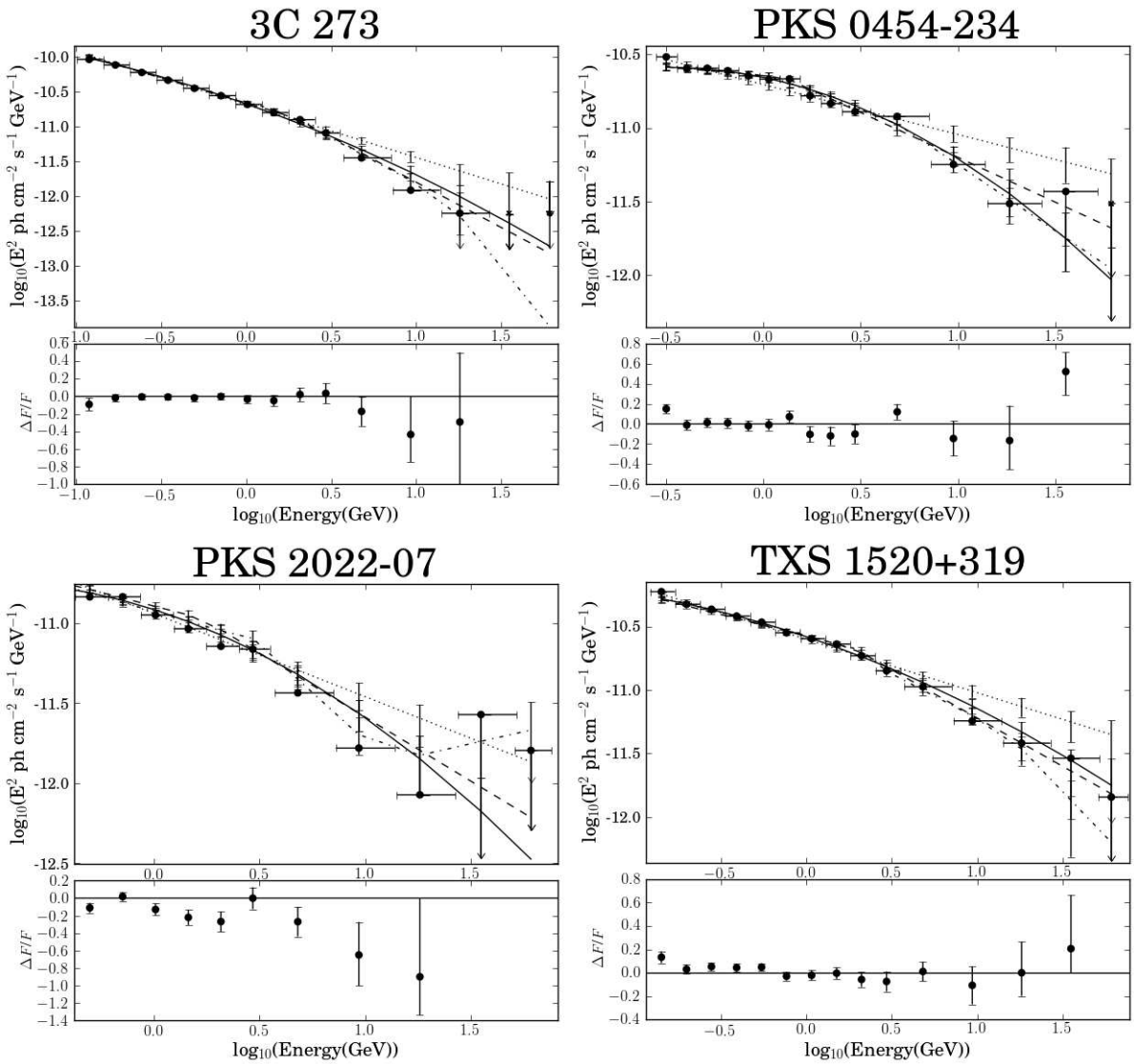

Figure 7.2: See caption of Figure 7.1.

7.5 Discussion

The double-absorber model predicts that a break should occur in the low energy set between 4 and 7 GeV. These results do not support this because although the fit to the spectra is in most cases significantly improved by introducing a break, the energy at which the break occurs generally does not fall in the predicted region. In the high energy set, the double-absorber model predicts that such a break should occur between 19 and 30 GeV. Again these results do not support this conclusion because fits to most objects were not significantly improved by introducing a break and in cases where they

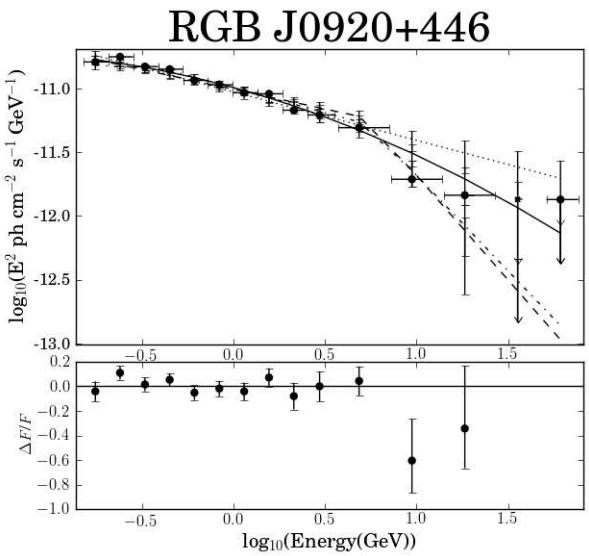

Figure 7.3: See caption of Figure 7.1.

Table 7.4: Spectral Properties of Objects over the Whole Time Period at Low Energy

Object	Min Energy	Peak $\log(\nu F_\nu)$ (GeV)	E_{break1} (GeV)	Index 1 Γ_1	Index 2 Γ_2	Sig over simple PL	4.8 GeV exclusion	4-7 GeV exclusion
3C 454.3	0.46	0.244	$3.3^{+0.2}_{-0.2}$	2.361±0.008	2.86±0.03	>99%	>99%	> 99%
PKS 1502+106	1.28	0.934	$2.8^{+0.6}_{-0.4}$	2.16±0.06	2.37±0.05	90%	86%	93%
3C 279	0.15	0.101	$1.6^{+0.3}_{-0.4}$	2.30±0.02	2.60±0.04	>99%	>99%	>99%
PKS 1510-08	0.41	0.112	$4.0^{+0.6}_{-1.0}$	2.41±0.02	2.9±0.1	>99%	76%	<1%
3C 273	0.12	0.005	$2.1^{+0.2}_{-0.7}$	2.70±0.02	3.4±0.1	>99%	>99%	>99%
PKS 0454-234	0.56	0.523	$2.1^{+0.3}_{-0.6}$	2.13±0.04	2.45±0.06	>99%	>99%	>99%
PKS 2022-07	0.24	0.693	6^{+1}_{-3}	2.38±0.06	3.1±0.4	83%	42%	<1%
TXS 1520+319	0.29	0.253	5^{+2}_{-1}	2.36±0.02	3.0±0.2	>99%	45%	<1%
RGB J0920+446	0.32	0.139	$1.3^{+0.2}_{-0.2}$	2.01±0.07	2.42±0.04	>99%	>99%	>99%

Table of results over the whole available time period in the energy region from Min Energy to 12 GeV. Values for peak $\log(\nu F_\nu)$ taken from Ref (5) except for PKS 2022-07 (see main text). E_{break1} is the value for the low energy spectral break which provided the best fit to the observed data. Γ_1 and Γ_2 are the photon spectral indices before and after the energy break respectively. Column 7 shows how significantly a broken power law improves the fit to the data compared with a simple power law. Columns 8 and 9 show the confidence level to which one can exclude energy breaks occurring at 4.8 GeV and in the $4-7$ GeV break region as predicted in PS10. All energies given in the object's rest frame.

Table 7.5: Spectral Properties of Objects over the Whole Time Period at High Energy

Object	Min Energy (GeV)	E_{break2} (GeV)	Index 3 Γ_3	Index 4 Γ_4	Sig over simple PL	19.2 GeV exclusion	19.2-30 GeV exclusion
3C 454.3	3.3	$7.3^{+1.9}_{-0.7}$	2.69±0.06	3.35±0.7	>99%	>99%	>99%
PKS 1502+106	2.8	12^{+4}_{-1}	2.36±0.05	3.1±0.1	>99%	94%	>99%
3C 279	1.6	35^{+1}_{-3}	2.6±0.2	>5	98%	94%	95%
PKS 1510-08	4.0	15^{+13}_{-5}	3.0±0.1	2.5±0.2	60%	40%	53%
3C 273	2.1	17^{+12}_{-5}	3.3±0.2	>5	52%	34%	47%
PKS 0454-234	2.1	10^{+2}_{-2}	2.50±0.07	2.9±0.2	87%	93%	99%
PKS 2022-07	6.0	31^{+9}_{-9}	3.2±0.2	1.7±0.5	90%	83%	11%
TXS 1520+319	5.0	40^{+10}_{-20}	2.7±0.1	3.4±0.6	47%	69%	63%
RGB J0920+446	1.3	17^{+3}_{-2}	2.39±0.04	3.5±0.3	>99%	53%	70%

Table of results over the whole available time period in the energy region after the first break. Min Energy is the lowest photon energy for inclusion. E_{break2} is the value for the high energy spectral break which provided the best fit to the observed data. Γ_3 and Γ_4 are the photon spectral indices before and after the energy break respectively. Column 6 shows how significantly a broken power law improves the fit to the data compared with a simple power law. Columns 7 and 8 show the confidence level to which one can exclude energy breaks occurring at 19.2 GeV and in the $19.2 - 30$ GeV break region as predicted in PS10. All energies given in the object's rest frame.

Table 7.6: Spectral Properties of Objects over different time periods.

Object	E_{break} (GeV)	ΔAIC$_{min}$	E_{break} (GeV)	ΔAIC$_{min}$	E_{break} (GeV)	ΔAIC$_{min}$
	No Time cut		Epoch 1		Epoch 2	
3C 454.3	$4.5^{+0.2}_{-0.3}$	0	$4.0^{+0.3}_{-0.3}$	0	$4.5^{+0.1}_{-0.1}$	0.32
PKS 1502+106	$11.2^{+1.1}_{-0.8}$	2.6	$10.7^{+1.8}_{-0.8}$	0.5	$2.3^{+0.4}_{-0.3}$	0
3C 729	$2.1^{+0.2}_{-0.3}$	6.6	$1.7^{+0.5}_{-0.1}$	6.1	$2.4^{+0.6}_{-0.8}$	2.9
PKS 1510-08	$3.5^{+0.6}_{-0.5}$	0	$3.1^{+0.8}_{-0.3}$	0	$3.9^{+0.5}_{-0.6}$	0
3C 273	$2.2^{+0.2}_{-0.5}$	0	$1.3^{+0.4}_{-0.2}$	8.9	$4.1^{+0.5}_{-0.5}$	0
PKS 0454-234	$2.6^{+0.5}_{-0.4}$	1.8	$3.3^{+0.3}_{-0.5}$	1.5	$1.4^{+0.2}_{-0.2}$	0
PKS 2022-07	$4.0^{+1.8}_{-0.7}$	0	$3.6^{+1.1}_{-0.9}$	0	$5.6^{+2.7}_{-0.9}$	0
TXS 1520+319	$4.7^{+1.2}_{-0.6}$	0	$4.4^{+2.2}_{-0.6}$	0.7	$4.4^{+2.0}_{-0.5}$	0
RGB J0920+446	16^{+2}_{-5}	0	$1.0^{+0.4}_{-0.1}$	0	$5.3^{+0.6}_{-1.2}$	0

Table of results found by splitting the data for each object into two equal time epochs. The most likely break energy for each object, in the object's rest frame, with no time cut and in each epoch individually is shown along with 68% confidence intervals and the difference from the AIC minimum, a value of 0 indicating a broken power law is the best fit to the data and a value > 2 indicating a log-parabola is a significantly better fit to the data.

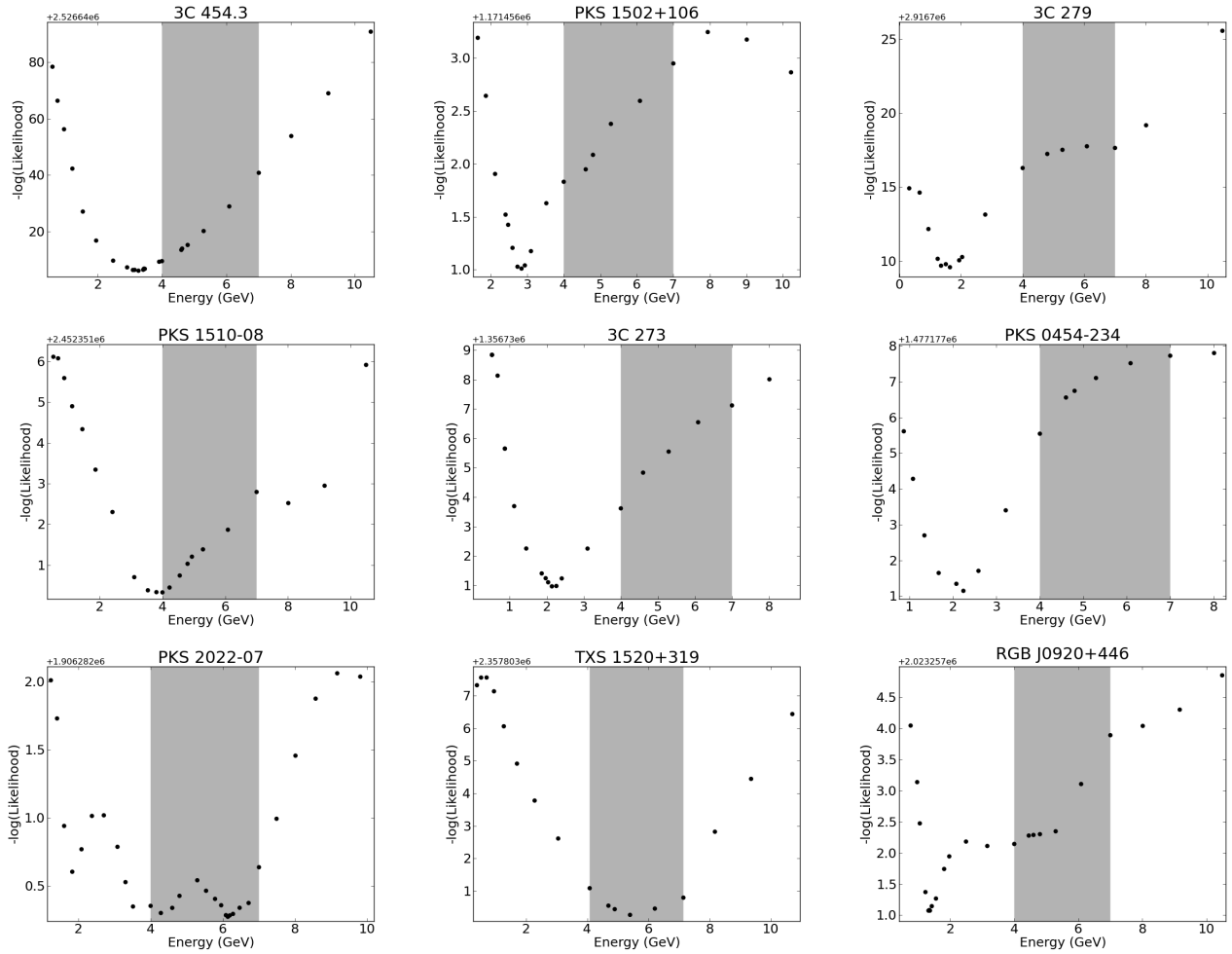

Figure 7.4: Plots of -log(Likelihood) against power law break energy, in the object's rest frame, for the low energy dataset of each object. The shaded box shows the region in which the double-absorber model predicts a spectral break to occur.

were the breaks did not fall within the predicted region. These conclusions also apply to the double-absorbed log-normal model presented in (144), since the Monte Carlo results presented earlier show that the break energies would still be identified correctly. For it to remain plausible that pair absoprtion with photons produced in the BLR have a significant effect on the HE γ-ray spectrum the photoionisation models used in PS10 would require significant modification. In several of the objects in our sample, a break at ~ 1 - $3\ \mathrm{GeV}$ is seen. To create such a break, a region with a high ionisation parameter line-like feature at ~ 70 - $110\ \mathrm{eV}$ that dominates over H and He lines would be needed. No such features could be found in the literature.

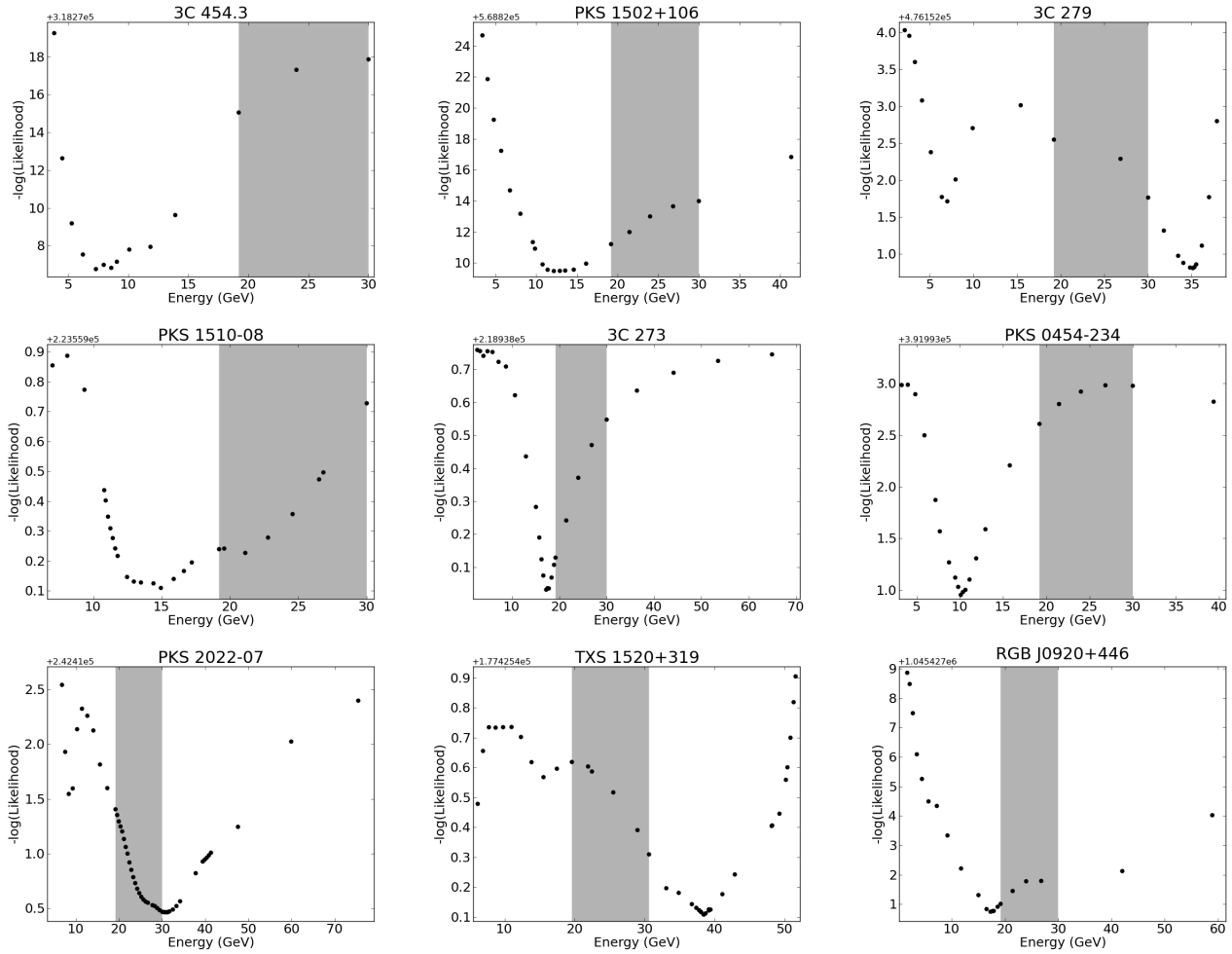

Figure 7.5: Plots of -log(Likelihood) against power law break energy, in the object's rest frame, for the high energy dataset of each object. The shaded box shows the region in which the double-absorber model predicts a spectral break to occur.

When examining all of the data (not splitting the dataset by energy or time), the spectra of all the sources deviate significantly from an SPL. However, without using physical motivation to prefer one model or the other, a BPL is not always a better description than an LP. An AIC test indicates 3 objects, PKS 1502+106, 3C 279, and RGB J0920+446, were described significantly better by an LP than a BPL, and PKS 0454-234 was described marginally better by an LP. It might be expected that an LP would be favoured for weaker sources since with the normalisation energy fixed, as it is here, the LP has one fewer degree of freedom than a BPL. However; these 4 sources were not the faintest in our sample, in fact 3C 279 had the second greatest flux. This suggests there is a genuine physical

difference in these objects.

For those objects that were better described by a BPL, the break appears between ~ 2 - 5 GeV in the source rest frame. The break energies determined in the low energy set and with no energy cut are consistent in all objects except 3C 454.3, PKS 1502+106, and RGB J0920+446, which may suggest the presence of curvature in the spectra of these objects as well as any break. The presence of curvature in the spectra of these objects is also supported by the fact that in each case a BPL fit to the high energy set was a significant improvement over an SPL.

5 of the 9 sources were not best fitted by the same spectral shape in both time epochs (i.e. the fit changes from an LP to a BPL or vice versa). There is weak evidence that the break energies of the BPL fits varies with time, suggesting that the primary cause of the break is intrinsic to the emission region. These observed changes in the spectra further disfavour the double-absorber model which predicts fixed break energies. The two component model could account for the change from a BPL to an LP shape between epochs if the emission region travelled up the jet beyond the radius of the BLR thereby removing the cause of the break. Likewise it could account for a change from an LP to a BPL shape if a new emission region was ejected from the central black hole, an event thought to cause flaring in the radio and γ-ray regimes (9). Only the behaviour of RGB J0920+446 cannot be explained with the two component model since it has a BPL spectrum in both epochs but the break energy changes dramatically from $1.0^{+0.4}_{-0.1}$ GeV in the first Epoch to $5.3^{+0.6}_{-1.2}$ GeV in the second. Alternatively, the changes in the spectral shape could be due to the distribution of the particles emitting the spectrum or it could be that when a spectrum with a given spectral shape and time-varying parameters is time-averaged it becomes best fitted by a different spectral shape, a hypothesis that we examine further in the next chapter.

In summary, the evidence disfavours the double-absorber model for bright *Fermi* FSRQs. The energy spectrum of γ-rays from bright FSRQ objects is sometimes better described by a log-parabola and sometimes by a power law with an energy break at a few GeV which varies with time. In order to investigate the causes of these features, a study presented in the next chapter extends the sample size, examines the spectra of BL Lac objects as well as FSRQs and examines the spectrum of 3C 454.3 on daily timescales.

Chapter 8

Spectral Properties of Fermi blazars II

8.1 Introduction

In this chapter I shall present a further study into the spectral shape of blazars using the *Fermi*-LAT. In some ways this study can be viewed as a continuation of the one presented in the previous chapter in that a sample of blazars was analysed in order to determine whether the best description of each object's spectrum was an SPL, BPL or LP. Descriptions of and motivations for these spectral shapes can be found in the preceding chapter, although in this study a normalisation energy of $E_0 = 1$ GeV was used for the SPL and LP. Since this study was carried out later it used the updated Pass7 LAT-IRF. It also extends the sample size and includes objects of the BL Lac class as well as FSRQs and studies the effect that nearby, confusing sources can have on the results. The results show that an LP is generally an adequate description of the an object's spectrum, especially when confusing sources are not expected to have a strong effect and BPL fits appear to arise as a result of source confusion. This conclusion is contrary to the one from the previous chapter. Further investigation shows that the discrepancy can be attributed to the change in the IRF between the studies. This study then goes on to probe the emission mechanisms of the bright blazar 3C 454.3 by constructing a light curve for this object. The results show that in its quiescent state, 3C 454.3 has a fairly stable spectrum that is well-described by an LP and that high flux states are likely caused by changes of parameters in the jet (as opposed to changes in an external photon field). Some high-flux blocks are well described by a BPL which is difficult to explain after ruling out the double-absorber and two component models described in the previous chapter.

8.2 Data Analysis

8.2.1 Event Selection

For each target, all photons with an energy between $100\ \mathrm{MeV}$ and $100\ \mathrm{GeV}$ and detected between MJD 54643 and MJD 56085 were analysed if they were reconstructed to originate from a 15° radius region of interest around the position of the source. These were analysed using the *Fermi* Science Tools v9r27p1 and the P7SOURCE_V6 version of the *Fermi*-LAT instrument response function (IRF) (14). Following standard practice,[1] it was required that events for analysis had been suitably reconstructed (event class 2 (diffuse) or better) and any photons which arrived while *Fermi*'s zenith angle was $< 100^\circ$ were discarded in order to avoid $\gamma-$ray contamination from the Earth.

Except where stated otherwise, throughout the study the isotropic and Galactic γ-ray emission were fitted using the iso_p7v6source and gal_2yearp7v6 models respectively[2] with the normalisations left as free parameters.

8.2.2 Sample selection

Owing to the LAT's continuous mode of observation, more data were available for this study than the previous one and therefore fainter objects could be included. All BL Lac and FSRQ objects from the *Fermi* 2-Year Point Source Catalog (2FGL) (114) were included in the initial sample if they had an average significance of 50 or more. This value is listed in the 2FGL and is derived from the likelihood ratio test statistic between $100\ \mathrm{MeV}$ and $100\ \mathrm{GeV}$. The chosen value selects sources roughly as significant above the background as the objects were in the previous study. Sources at Galactic latitude of 10° or less were not included in the study (to avoid contamination from the Milky Way). This gave a sample of 15 BL Lacs and 27 FSRQs.

The point spread function of the LAT is as large as 3° at $100\ \mathrm{MeV}$ (114) and this has the potential to cause a significant amount of confusion between sources. This was more of a concern than in the previous study as fainter objects were now being included and therefore some objects may not be very bright compared to their neighbours.

The model selection entailed fitting an SPL, BPL and LP to each object and determin-

[1] http://fermi.gsfc.nasa.gov/ssc/data/analysis/scitools/likelihood_tutorial.html
[2] http://fermi.gsfc.nasa.gov/ssc/data/access/lat/BackgroundModels.html

ing which (if any) of these was the best description. Therefore it was necessary to be confident that for each target object the simplest of these models, namely the SPL, could be fitted free from confusion. If this could not be done it suggested that noise was having a significant effect on the fit.

To this end confusion Monte Carlo simulations were run using the standard tool *gtobssim*. For each of the target sources, an input model was created which included the target source and all point sources in the 2FGL within 3°. The target source was modelled as an SPL with the best fit values from the 2FGL. The confusing sources were each modelled as an SPL with values selected randomly from a normal distribution about their 2FGL values.

This input model was then used to generate simulated events equivalent to an observation spanning MJD 54643 to MJD 56085. This simulated observation was then analysed using a binned analysis in *gtlike* with the parameters of the target source left free and the parameters of the confusing sources fixed to their 2FGL values.

This method was repeated 100 times and in each simulation it was recorded whether or not the input value of the target source's spectral index was included in the 68% confidence interval of the estimated value. If it was, then the simulation was deemed a 'success'. If no source confusion occurs then each object should have a 68% success rate in its 100 simulation observations with some random error. Therefore, the mean success rate of a clean sample of objects should be 68%. Objects which suffered from source confusion would be expected to have a success rate below 68% and therefore drag the average of a sample down.

Once the simulations for all of the target sources were complete, the target source with the lowest success rate was repeatedly removed until the mean success rate of the sample was 68%. The remaining sources constituted the 'clean' sample while those that were removed constituted the 'unclean' sample. The clean sample consisted of 5 BL Lacs and 15 FSRQs and the unclean sample consisted of 10 BL Lacs and 12 FSRQs. These samples are listed in Table 8.1 along with the 2FGL significance and success value of each source.

8.2.3 Model Comparison

As in the previous study, for each object the likelihoods of the data coming from SPL, BPL and LP models were each calculated using the NEWMINUIT routine in *gtlike*. These 3 spectral shapes were then compared using an AIC test to determine which, if any, was a significantly better description of the data. A binned analysis was used and all sources in the 2FGL within 15° of the target were included with their parameters fixed to their 2FGL values.

8.2.4 Truncation of the energy range

In order to find a suitable energy range, energy truncation was applied. The method for this was very similar to that described in the previous chapter, with a few small differences. Initially, data for each object over the whole energy range was fitted with an LP. The Compton Peak energy, E_P, was then estimated as

$$E_p = E_0 e^{(2-\Gamma)/2\beta}, \tag{8.1}$$

(see, e.g. (101), but note that the logarithms in this study are being taken to base e rather than base 10). Since BL Lacs were included in this study, some objects might have high spectral peaks, above the energy range being tested and with more significant curvature towards the high end of the energy range. For this reason, if an initial LP fit to the spectrum of an object revealed the Compton peak energy to be above the high energy threshold of $100\ \mathrm{GeV}$ the stability of the fit was tested by reducing the high energy threshold (rather than increasing the low energy threshold as described in the previous chapter). For this study $100\ \mathrm{MeV}$ steps were used (rather than $50\ \mathrm{MeV}$) for expediency, since work between the two studies had showed this step size to be more than adequate.

8.2.5 Light curve analysis

A daily light curve was created for the brightest object in the sample, 3C 453.3 (2FGL J2253.9+1609), in the energy range $100\ \mathrm{MeV}$ to $100\ \mathrm{GeV}$. The daily time bins were then grouped into blocks of consistent flux using the Bayesian blocks technique. Identifying blocks of consistent flux is important because different emission mechanisms may be in effect during e.g. the stages of rising and falling flux.

Table 8.1: List of objects

Clean Sample			Unclean Sample		
Object Name	σ	Success	Object Name	σ	Success
BL Lacs			BL Lacs		
J0428.6-3756	105	62%	J0222.6+4302	59	7.3%
J0538.8-4405	164	76%	J0238.7+1637	92	54%
J0721.9+7120	115	77%	J0449.4-4350	66	12%
J2158.8-3013	104	64%	J0818.2+4223	51	61%
J2202.8+4216	59	48%	J1015.1+4925	54	48%
			J1104.4+3812	131	38%
FSRQs			J1427.0+2347	64	58%
J0136.9+4751	52%	67%	J1542.9+6129	52	59%
J0403.9-3604	67	69%	J1555.7+1111	69	0%
J0457.0-2325	126	66%	J1653.9+3945	55	0%
J0730.2-1141	93	67%			
J0920.9+4441	76	68%	FSRQs		
J0957.7+5522	75	65%	J0108.6+0135	60	50%
J1159.5+2914	52	67%	J0442.7-0017	51	58%
J1224.9+2122	182	71%	J0719.3+3306	52	53%
J1229.1+0202	140	61%	J0725.3+1426	58	61%
J1256.1-0547	148	73%	J0808.2-0750	71	36%
J1457.4-3540	66	66%	J1246.7-2546	57	51%
J1512.8-0906	202	74%	J1312.8+4828	67	61%
J1522.1+3144	131	70%	J1428.0-4206	68	60%
J1849.4+6706	60	68%	J1504.3+1029	116	61%
J2253.9+1609	339	65%	J1635.2+3810	76	16%
			J2025.6-0736	63	57%
			J2025.6-0736	63	57%
	$<\sigma>$	68%		$<\sigma>$	45%

σ is the average significance in the 2FGL (see (114)). Success refers to the success rate of finding the correct input spectral index in Monte Carlo simulations, with 68% being the statistical expectation for a source with no confusion, see full text for details.

Details of the Bayesian blocks technique can be found in Ref (135), but I will outline the method here. The algorithm breaks the light curve into blocks that are likely to have constant flux. Moreover, it does so in a very computationally efficient way (if we had f segments in our light curve then there are 2^f ways of partitioning it). Briefly, we start with the values of the daily flux bins from the light curve. Scargle et al. give a fitness function for any block of these flux bins if we assume the underlying spectrum is constant. This fitness function for a block is given as $F(R)$. The numerical value for F is found using a likelihood technique, and the larger the value of $F(R)$ for a given R, the greater the likelihood of the data in R coming from the same underlying spectrum.

Let us say that we have a list of daily bins $i = 1, 2, 3, ...f$. We want to find the optimal way of partitioning up these bins into blocks such that each block has a constant flux. We start by considering only the first bin, $i_{max} = 1$. In this case, there is only one bin and so only one way to partition the data.

If we consider $i_{max} = 2$ then the fitness function $F(1, 2)$ will tell us that either it is optimal for the bin $i = 2$ to be placed in a block with $i = 1$ or for the 2 bins to be in separate blocks, depending on whether

$$F(1) + F(2) > F(1 + 2) \ . \tag{8.2}$$

If we consider $i_{max} = 3$ then $F(1, 2, 3)$ will tell us if it it is optimal for bin $i = 3$ to be placed in a block with bins $i = 1, 2$, or to be placed in a block with only bin $i = 2$, or to be placed in block on its own, based on the maximum of

$$\begin{aligned} &F(1,2) + F(3), \\ &F(1) + F(2,3), \\ &F(1,2,3). \end{aligned} \tag{8.3}$$

If we consider $i_{max} = 4$ we need to find the maximum of

$$\begin{aligned} &F(1,2,3) + F(4), \\ &F(1,2) + F(3,4), \\ &F(1) + F(2,3,4), \\ &F(1,2,3,4). \end{aligned} \tag{8.4}$$

Generically for $i_{max} = x$ we need to find the maximum of

$$F(1, ...N - 1) + F(N, ...x), \tag{8.5}$$

for $N = 0 \rightarrow x$. Once this is calculated for the whole set ($i_{max} = f$), if we store the value for $F(1, ...N)$ each time then we know the best way to split the bins into two blocks. The partition should occur for the value of N which returns the maximum value of F. We then have our two blocks:

$$F(1, ...N - 1), \tag{8.6}$$

and

$$F(N, ...f). \tag{8.7}$$

What if we want to subdivide the partitions into smaller blocks? We would need to find the optimal way to partition each of the two blocks that we have by calculating F for each possible sub-partition. But for our first block these values have already been calculated. For example, assume that the first partition was made for $N = 5$, then

$$F(1, ...N - 1) = F(1, 2, 3, 4), \tag{8.8}$$

which we can see above has already been calculated. This process can be repeated until the optimal way of partitioning up the data has been found.

After this method was applied to the light curve of 3C 454.3, each block in a high flux state was examined to see if it was best described by an SPL, BPL or LP. A high flux was defined as as $> 5 \times 10^{-6}$ ph cm^{-2} s^{-1}. This threshold was required to distinguish between BPL and LP spectra on daily timescales. The method for analysing each block was the same as described in Section 8.2.3 but using an unbinned *Fermi* analysis, which was computationally feasible on these smaller data sets. All of the data from the quiescent blocks (which were defined as having flux $\leq$ the average flux plus one standard deviation) were also analysed together and the result was compared to the high flux blocks.

8.3 Results

8.3.1 Searching for breaks and curvature

The results of searching for breaks and curvature are shown in Tables 8.2 and 8.3. Of the 5 BL Lacs in the clean sample, 3 were described significantly better by an LP and 2 showed significant deviation from an SPL, but in these cases distinguishing between

a BPL and an LP was not possible. Of the 15 FSRQs in the clean sample, 11 were described significantly better by an LP, 1 object was best described by an SPL and 3 showed significant deviation from an SPL but distinguishing between a BPL and an LP was not possible. The single object in our clean sample that was best described by an SPL was 4C +55.17 (2FGLJ0957.7+5522) which was found to have a spectrum of $\frac{dN}{dE} = (1.9 \pm 0.4) \times 10^{-11} \left(\frac{E}{10^3 \text{ MeV}}\right)^{-2.33 \pm 0.09}$ ph cm^{-2} s^{-1} MeV^{-1}.

Table 8.2: AIC results for the clean sample

Object Name	$\Delta AIC_{min,SPL}$	$\Delta AIC_{min,BPL}$	$\Delta AIC_{min,LP}$
BL Lacs			
J0428.6-3756	13.5	0.6	0.0
J0538.8-4405	86.8	2.9	0.0
J0721.9+7120	35.4	2.8	0.0
J2158.8-3013	14.7	1.8	0.0
J2202.8+4216	51.0	2.3	0.0
FSRQs			
J0136.9+4751	19.9	1.7	0.0
J0403.9-3604	138.7	13.6	0.0
J0457.0-2325	248.6	22.8	0.0
J0730.2-1141	24.9	4.6	0.0
J0920.9+4441	25.4	0.0	1.7
J0957.7+5522	0.0	3.0	1.8
J1159.5+2914	40.3	2.7	0.0
J1224.9+2122	82.8	10.1	0.0
J1229.1+0202	25.7	0.0	0.1
J1256.1-0547	85.8	5.5	0.0
J1457.4-3540	20.7	3.5	0.0
J1512.8-0906	213.7	13.3	0.0
J1522.1+3144	109.5	4.0	0.0
J1849.4+6706	39.9	6.0	0.0
J2253.9+1609	487.9	37.5	0.0

$\Delta AIC_{min,s}$ is the difference in AIC value between a model s and the best model for that source. A value of 0 indicates the best description of the data and values > 2 indicate a description is significantly worse than one of the others tested.

Table 8.3: AIC results for the unclean sample

Object Name	$\Delta AIC_{min,SPL}$	$\Delta AIC_{min,BPL}$	$\Delta AIC_{min,LP}$
BL Lacs			
J0222.6+4302	3.4	0.0	5.4
J0238.7+1637	22.7	2.6	0.0
J0449.4-4350	2.9	0.0	0.2
J0818.2+4223	23.4	3.6	0.0
J1015.1+4925	15.6	1.1	0.0
J1104.4+3812	9.2	0.6	0.0
J1427.0+2347	15.7	2.1	0.0
J1542.9+6129	0.9	1.4	0.0
J1555.7+1111	11.5	0.0	0.3
J1653.9+3945	9.8	0.0	4.8
FSRQs			
J0108.6+0135	39.5	5.7	0.0
J0442.7-0017	4.6	1.4	0.0
J0719.3+3306	8.3	0.0	0.1
J0725.3+1426	9.8	1.8	0.0
J0808.2-0750	16.9	0.0	2.0
J1246.7-2546	91.5	10.4	0.0
J1312.8+4828	7.8	3.0	0.0
J1428.0-4206	73.6	7.7	0.0
J1504.3+1029	94.7	8.2	0.0
J1635.2+3810	112.8	14.8	0.0
J2025.6-0736	71.6	2.0	0.0
J2056.2-4715	55.4	1.1	0.0

$\Delta AIC_{min,s}$ is the difference in AIC value between a model s and the best model for that source. A value of 0 indicates the best description of the data and values > 2 indicate a description is significantly worse than one of the others tested.

In the clean sample, more than half the objects were described significantly better by an LP than an SPL or a BPL, and all the sources are consistent with the hypothesis of an LP spectrum (i.e. neither an SPL or a BPL were a significantly better description than an LP). Given that LP fits seemed ubiquitous and this spectral shape is capable of describing the area around the peak energy of the SED, a further analysis was run on the clean sample using an LP description over the entire, untruncated, energy range. The results of these fits are shown in Table 8.4. For the 10 objects that required the use of a truncated energy range in the earlier analysis, 8 showed a value of Γ consistent at the 1σ confidence level with that found using the whole energy range and 4 were consistent in the value of β. Among the values that did not agree there was roughly equal scatter in the values found using the whole energy range above and below the values found using the truncated energy range. This suggests that no bias is introduced in the values for Γ and β by truncating the energy range, although using the whole energy range of course includes more data and is therefore preferred. Both BL Lacs and FSRQs show a wide range of values for Γ and β. However, T-tests determined that, compared to BL Lacs, FSRQs have significantly softer spectral indices (Γ), less curvature (β) and lower Compton peak energies (E_P) with p-values of 0.002, 0.01 and 0.04 respectively. These results are qualitatively consistent with the differences between the spectral parameters of BL Lacs and FSRQs in the literature. With a p-value of 0.41, the difference in the maximum value of the SED, $\log E_P F(E_P)$, found for BL Lacs and FSRQs in the clean sample was not significant, which is most likely a selection bias where only objects above a certain brightness are included.

Of the 10 BL Lacs in the unclean sample, 3 were described significantly better by an LP, 2 were described significantly better by a BPL, 4 showed significant deviation from an SPL but distinguishing between a BPL and an LP was not possible, and 1 object showed no significant deviation from an SPL. Of the 12 FSRQs in the unclean sample, 7 were described significantly better by an LP, 1 was described significantly better by a BPL, and 4 showed significant deviation from an SPL but distinguishing between a BPL and an LP was not possible.

The unclean sample contained the only sources that were identified as having BPL spectra, and a higher incidence of sources where BPL and LP fits could not be distinguished from one another. Caution should be exercised when working with sample sizes

Table 8.4: Values for log-parabola fits to the clean sample in the energy range 100 MeV to 100 GeV

Object Name	Normalisation Constant	Spectral Index	Curvature Parameter
	10^{-11} ph cm^{-2} s^{-1} MeV^{-1}	Γ	β
BL Lacs			
J0428.6-3756	2.1 ± 0.2	1.7 ± 0.1	0.16 ± 0.04
J0538.8-4405	3.98 ± 0.05	2.06 ± 0.01	0.069 ± 0.008
J0721.9+7120	2.50 ± 0.04	1.97 ± 0.03	0.09 ± 0.01
J2158.8-3013	1.97 ± 0.04	1.82 ± 0.01	0.027 ± 0.007
J2202.8+4216	2.16 ± 0.04	2.26 ± 0.01	0.061 ± 0.009
FSRQs			
J0136.9+4751	0.74 ± 0.03	2.34 ± 0.03	0.08 ± 0.02
J0403.9-3604	1.14 ± 0.03	2.69 ± 0.03	0.18 ± 0.02
J0457.0-2325	2.71 ± 0.04	2.27 ± 0.01	0.126 ± 0.009
J0730.2-1141	2.52 ± 0.05	2.35 ± 0.02	0.06 ± 0.01
J0920.9+4441	0.92 ± 0.03	2.37 ± 0.03	0.10 ± 0.02
J0957.7+5522	1.4 ± 0.9	2.1 ± 0.6	0.1 ± 0.1
J1159.5+2914	1.10 ± 0.03	2.27 ± 0.02	0.08 ± 0.01
J1224.9+2122	3.60 ± 0.05	2.34 ± 0.01	0.054 ± 0.006
J1229.1+0202	1.82 ± 0.04	2.82 ± 0.02	0.09 ± 0.02
J1256.1-0547	3.14 ± 0.05	2.42 ± 0.01	0.066 ± 0.008
J1457.4-3540	1.04 ± 0.04	2.38 ± 0.03	0.10 ± 0.02
J1512.8-0906	6.49 ± 0.06	2.447 ± 0.009	0.070 ± 0.005
J1522.1+3144	2.82 ± 0.04	2.42 ± 0.01	0.074 ± 0.008
J1849.4+6706	0.79 ± 0.03	2.20 ± 0.03	0.11 ± 0.02
J2253.9+1609	17.5 ± 0.1	2.475 ± 0.007	0.132 ± 0.007

this small, but it seems probable that BPL fits can be favoured as a result of source confusion. This conclusion is supported by the particularly high likelihood of the sources with BPL fits suffering source confusion in Monte Carlo simulations (see Table 8.1). The BPL model has 1 more free parameter than the LP model, and so it would not be expected that a BPL would be found to be a better description of fainter objects simply because the photon numbers are worse, in fact the opposite is true. We shall return to this topic in the next subsection.

The results from this study can be quickly compared to those in the 2FGL. Since the work for the 2FGL was carried out at an earlier date, less data was available and therefore we can see the effect of accumulating more data for the sources. Of the 20 objects which were reported in the 2FGL as having LP spectra, 10 had values for β that were consistent at the 1σ level with the values found for those objects in this work using longer observation times. The values in the 2FGL that were not consistent scattered equally above and below the values found in this work. This suggests that once enough data have been collected for a source to identify curvature in the spectrum this value does not then change simply by collecting more data, e.g. the spectra do not appear as having more curvature as more data are collected.

8.3.2 Exploring the effects of Source Confusion

In the previous subsection, it was concluded that BPL fits probably became favoured as a result of source confusion. In order to explore this hypothesis further, Monte Carlo simulations using *gtobssim* were performed. The source chosen for this simulation was 3C 66A (2FGLJ0222.6+4302). This source had one of the lowest success rates for correctly identifying the input parameters of an SPL in the initial Monte Carlo simulations (see Section 8.2.2) and was found observationally to be best described by a BPL (see Table 8.3).

In order to see if a BPL fit could erroneously be favoured, the following simulated observation, equivalent to the dates MJD 54643 to MJD 56085, was performed. The input spectrum for the target was an LP. The parameters used were the SPL parameters from the 2FGL but with a modest curvature of $\beta = 0.1$ (see Table 8.4). As before, confusing sources in the 2FGL within 3° were included. There were 2 such objects: 2FGLJ0218.1+4233, which is 0.96° from the target with an integrated flux 19% the strength of the target; and 2FGLJ0230.8+4031, which is 2.9° from the target with an inte-

grated flux 5% the strength of the target. Again, as before, these objects were given SPL spectra drawn from a normal distribution about their 2FGL values.

After the observation was performed, a model was fitted using *gtlike*. Isotropic emission was included as normal, and the confusing sources were modelled as SPL and fixed to their 2FGL values. The target source was modelled alternately as an LP and a BPL with free parameters. The difference in AIC for the LP fit and the BPL fit was then calculated. This simulated observation was repeated 60 times. In all 60 cases, the BPL fit was found to be a better description than the LP fit. In only 1 case was the BPL found to be a significantly better fit ($\Delta_{AIC} > 2$).

The simulations were then repeated 45 times, but allowing the flux normalisations and spectral indices of the confusion sources to vary in the fits. The results were the same as before, with the BPL being a better fit in 42 cases and significantly better in 1 case. This rules out BPL fits being favoured as a result of fixing too many of the parameters in the fitting.

These simulations suggest that BPL fits can indeed be erroneously favoured over LP fits due to source confusion. It is interesting that in the simulations the difference in significance between the fits is not usually significant. The fact several objects in the observational study still favoured BPL fits significantly could have several explanations: there could be a small break in either the spectrum of the target object or the spectrum of 1 or more confusing objects; there could be curvature in the spectrum of 1 or more confusing objects which further disrupts the fit; there could be additional, faint point sources not in the 2FGL which further disrupt the fit; additional confusion with Galactic or isotropic emission could occur as the actual emission will not be perfectly modelled, as the simulated emission is; or the significance of some of the BPL fits could occur due to statistical chance.

8.3.3 The Effect of the Instrument Response Function

In the clean sample there are 3 FSRQ objects, 3C 454.3, PKS 1510-08, and TXS 1520+319, which show discrepancies with the results of the study in the previous chapter. In this study they were found to be described significantly better by an LP but in the previous study they were described significantly better by a BPL. It seems that there are 3 possible explanations for this:

Table 8.5: Comparison of spectral fits using different instrument response functions.

Object Name	$\Delta AIC_{LP,BPL}$ using $P6\_V3$	Change when using $P6\_V11$	Change when using $P7\_V6$
J0457.0-2325	1.8	3.6	5.6
J0920.9+4441	13.2	-11.1	-1.3
J1229.1+0202	-1.5	-3.9	18.0
J1256.1-0547	6.6	-7.7	-3.5
J1504.3+1029	2.6	-6.0	-0.3
J1512.8-0906	-2.4	-2.6	4.9
J1522.1+3144	-9.2	-2.6	13.9
J2025.6-0736	-0.4	0.5	2.3
J2253.9+1609	-12.8	-16.0	65.7

The second column gives the difference in AIC values when fitting the spectrum with a Broken Power Law and a Log-Parabola using the P6_V3 IRF. A positive value shows that LP was favoured and a negative value indicates a BPL was favoured. The third and fourth columns show how this value changes using the P6_V11 and P7_V6 IRFs respectively. A positive value shows that an LP fit is better than when using P6_V3 IRF and a negative value shows that a BPL fit is better than when using P6_V3 IRF.

- By including more data the time-averaged spectra become log-parabolic.
- The difference is due to using an unbinned analysis in the previous study and a binned analysis in this work.
- The difference is due to using the P6_V3_DIFFUSE IRF in the previous study and the newer P7SOURCE_V6 IRF in this work.

To determine which explanation was more likely, binned and unbinned analyses were run for the objects in question using the time and energy cuts of the previous study and using the P6_V3_DIFFUSE, P6_V11_DIFFUSE and P7SOURCE_V6 IRFs along with the appropriate and isotropic and Galactic emission models. The results showed that the decision to use a binned or unbinned analysis did not affect the result but that analyses

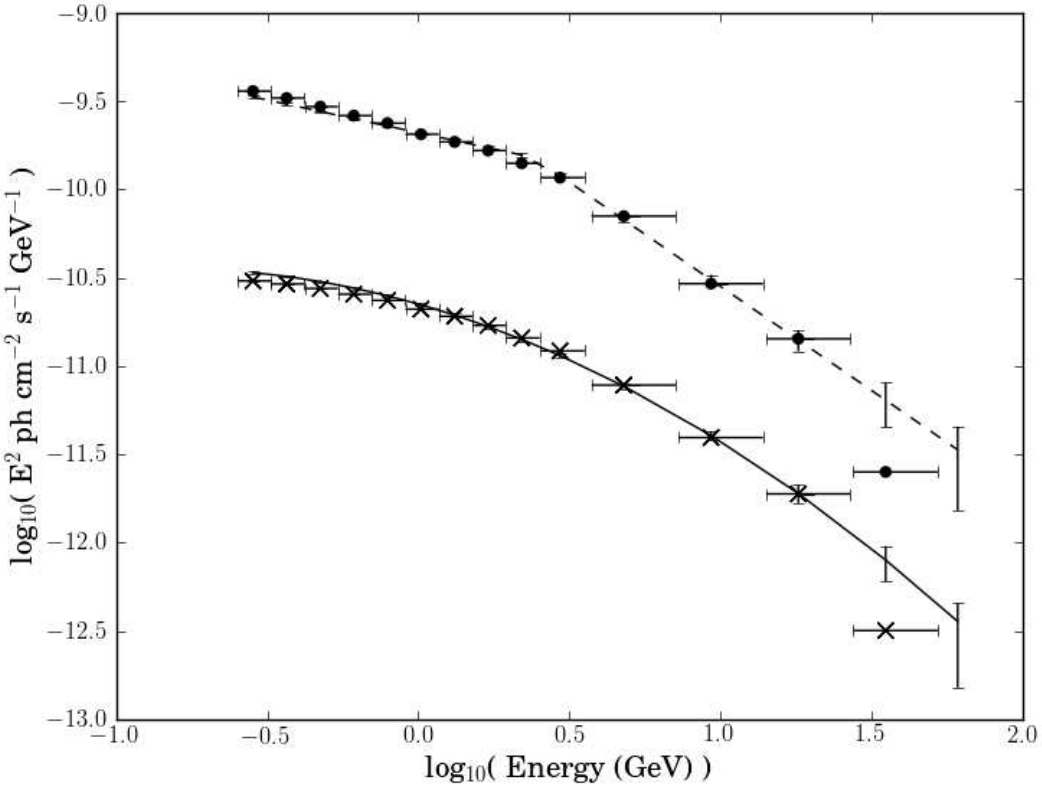

Figure 8.1: Aperture photometry results from 2FGLJ2253.9+1609 (3C 454.3) for illustrative purposes. The data points are taken using small, 1° regions of interest around the source, relying on this to keep the signal to noise high rather than modelling the background. Circles are results obtained using P6_V3_DIFFUSE IRF and crosses are results obtained using P7SOURCE_V6. In each case the best fitting model is displayed along side the data. Each model has 68% confidence level error bars for the energies of each data point, see (15). The P7 data and model have been divided by an arbitrary factor of 10 for clarity.

using both the P6_V3_DIFFUSE and P6_V11_DIFFUSE IRFs identified all 3 sources as having BPL descriptions while using P7SOURCE_V6 identified the sources having LP descriptions. It is clear from this that the differences between the Pass6 and Pass7 IRFs (see (14)) have a significant effect in determining the spectrum of an object.

To explore the effect on a slightly larger sample of objects, unbinned analyses were then performed for all of the objects from the previous study using the time and energy cuts from that work and using the P6_V11_DIFFUSE and P7SOURCE_V6 IRFs (analyses

using P6_V3_DIFFUSE having already been presented in the previous chapter). Ideally a larger sample would be used but doing so would be problematic. P6_V3 data are only available up to MJD 55707 and this is only enough time to distinguish detailed spectral shapes in very bright objects such as the ones used here. For each object, the value for $\Delta AIC_{LP,BPL}$ found using P6_V3_DIFFUSE is shown in Table 8.5 along with the *change* in this value using P6_V11_DIFFUSE and P7SOURCE_V6. As can be seen, using P6_V11_DIFFUSE, the AIC value for most objects finds a BPL to be a better description compared to the LP than in P6_V3_DIFFUSE, although some objects still favour an LP. Going from P6_V3_DIFFUSE to P7SOURCE_V6, some objects favour an LP more strongly and some a BPL more strongly, with those favouring an LP more strongly generally seeing a larger effect. For illustrative purposes, the results of the aperture photometry analysis of 2FGLJ2253.9+1609 (3C 454.3) over the time period used in Paper I, analysed using Pass6 and Pass7 IRFs, along with the best models from the unbinned analyses, are shown in Figure 8.1.

It seems clear that the choice of IRF can alter which spectral shape is favoured. However, there does not appear to be a systematic bias towards finding either BPL or LP spectra when the IRF is updated from Pass6 to Pass7. It may well be that whether an LP fit becomes more or less favoured for a given object (compared to a BPL fit) depends upon the energy of that object's spectral peak. As stated previously, using the Pass7 IRF, which is the most recent IRF and hopefully the most accurate, an LP is an adequate description for all objects in the clean sample and in most cases is significantly preferred over a BPL.

8.3.4 Light curve analysis of 3C 454.3

Spectral shapes in the light curve of 3C 454.3 and other prominent objects

As shown in Figures 8.2 and 8.3, the light curve of 3C 454.3 has 3 prominent states of high flux. The spectral behaviour in these 3 states does not appear to be consistent. The high states around MJD 55150 and MJD 55300 were significantly better described by LPs at their peaks, with BPL blocks on either side of the peaks. However, the high state around MJD 55530 was significantly better described by a BPL at its peak, with a roughly even number of BPL and LP blocks on either side. In total, only 2 blocks were described

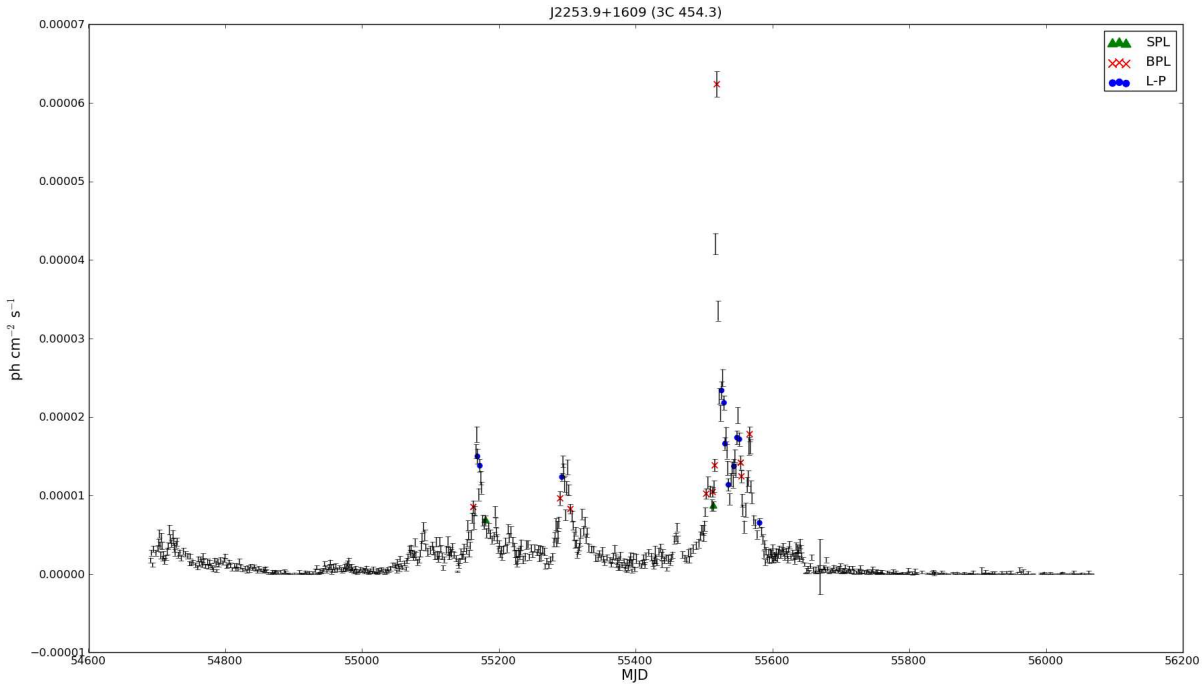

Figure 8.2: The light curve of 2FGLJ2253.9+1609 (3C 454.3). The symbols indicate Bayesian blocks which are significantly better described by simple power law (triangles), broken power law (crosses), and log-parabola (circles) models. Blocks with no symbol saw no significant deviation between models. The high states between MJD 55150 and MJD 55300 are best described by log-parabolas at their peaks, but the high state at MJD 55500 is best described by a broken power law at its peak. Zoomed in sections are shown in the following figure.

significantly better by an SPL.

3 other bright objects from the sample, PKS 1510-08 (2FGLJ1512.8-0906), 3C 273 (2FGLJ1229.1+0202) and 4C 21.35 (2FGLJ1229.1+0202), were also selected for light curve analyses using the same methodology. The results are shown in Figures 8.4 - 8.6. Unfortunately, for each object, only in a small number of blocks does one spectral shape provide a significantly better description of the spectrum than the other spectral shapes. This is understandable since the objects are a factor of 10 or more dimmer than 3C 454.3. However, it can be seen that several blocks in the light curve of PKS 1510-08 are significantly better described by a BPL, demonstrating that the appearance of BPL blocks in

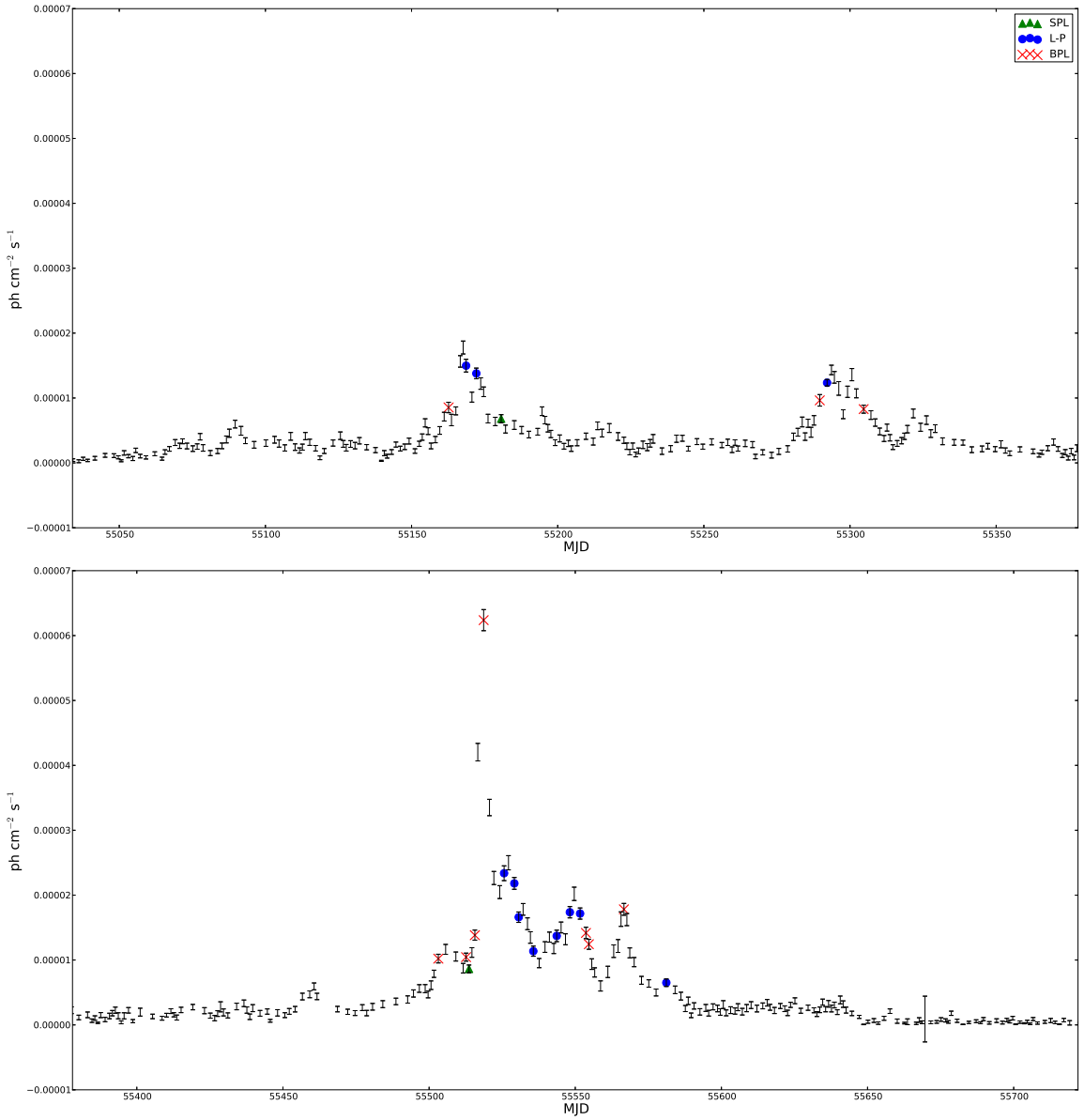

Figure 8.3: A zoom in on the parts of the light curve of 2FGLJ2253.9+1609 (3C 454.3) where periods of time containing blocks that have with significant deviation between the different spectral fits. The symbols indicate Bayesian blocks which are significantly better described by simple power law (triangles), broken power law (crosses), and log-parabola (circles) models. Blocks with no symbol saw no significant deviation between models.

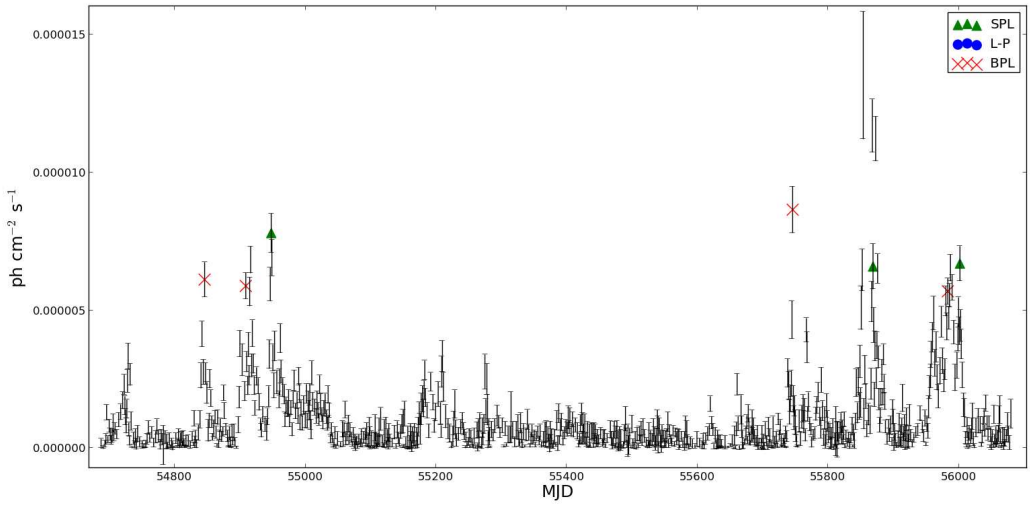

Figure 8.4: Light curve of PKS 1510-08 (2FGLJ1512.8-0906). The symbols indicate Bayesian blocks which are significantly better described by simple power law (triangles), broken power law (crosses), and log-parabola (circles) models. Blocks with no symbol saw no significant deviation between models.

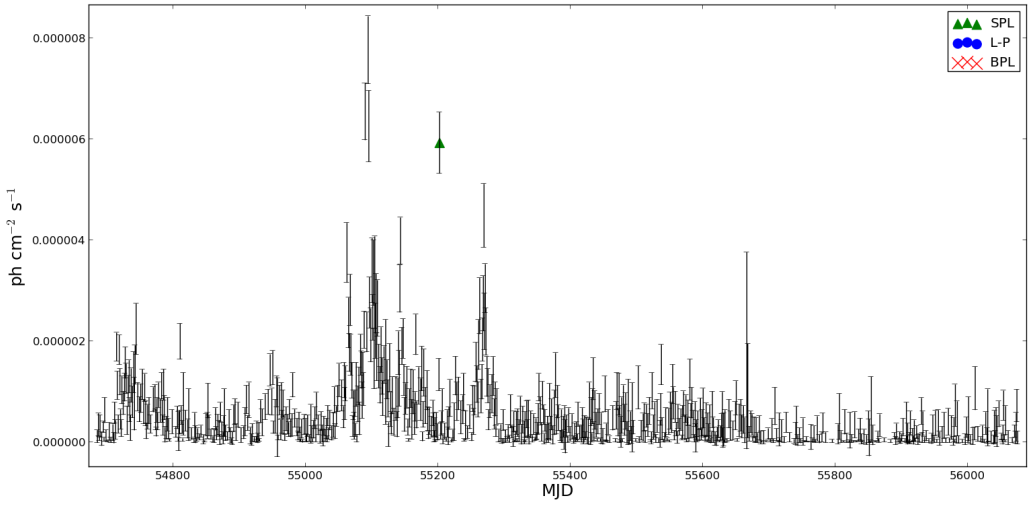

Figure 8.5: Light curve of 3C 273 (2FGLJ1229.1+0202). The symbols indicate Bayesian blocks which are significantly better described by simple power law (triangles), broken power law (crosses), and log-parabola (circles) models. Blocks with no symbol saw no significant deviation between models.

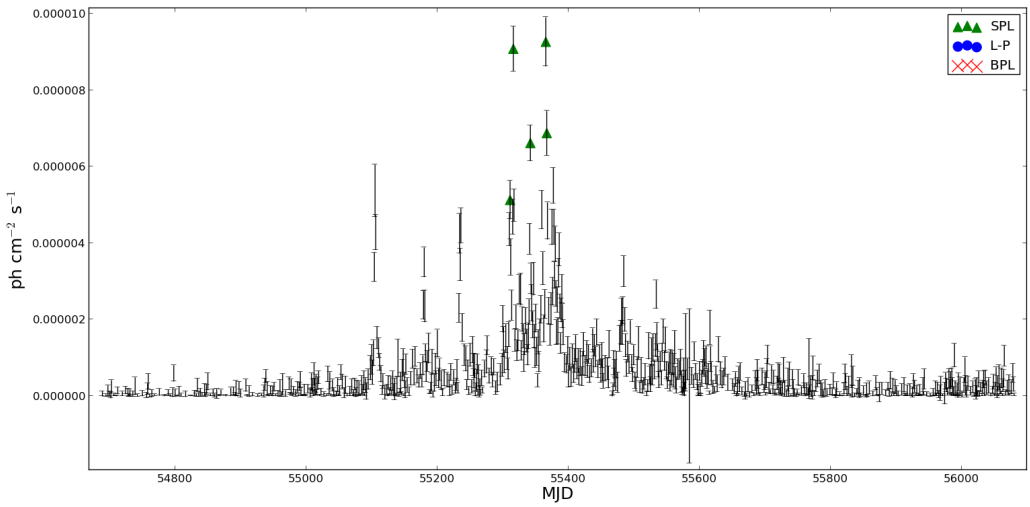

Figure 8.6: Light curve of 4C 21.35 (2FGLJ1229.1+0202). The symbols indicate Bayesian blocks which are significantly better described by simple power law (triangles), broken power law (crosses), and log-parabola (circles) models. Blocks with no symbol saw no significant deviation between models.

3C 454.3 is not unique. This result is consistent with the more detailed study of the light curve of the object by Anthony Brown (43). A more detailed study of the light curve of 3C 273 (2FGLJ1229.1+0202) by Bindu Rani et al. (129) is also in agreement with the results presented here. (Some care should be given comparing the significance of the difference in fits between different spectral shapes in these studies and in the current work as different methods were used in each case.)

Cause of flux increases

By analysing together the data from all of the quiescent blocks it was found that the quiescent state was significantly better described by an LP than a BPL, with $\Delta AIC_{LP,BPL} = 19$. The parameters of the LP fit are shown in Table 8.6 and give $E_P = 109 \pm 14$ MeV. Comparing these values with those in Table 8.4 we can see that the quiescent and time-averaged values for β were consistent, while Γ was slightly harder when the higher flux states were included. The values of Γ, β, and E_P in the individual blocks of quiescent flux were then compared to the values found analysing all of these blocks together. At the 1σ level the value of Γ agreed in 59% of blocks, the value of β agreed in 64% of blocks,

Table 8.6: Log-Parabola Fit to the Quiescent State of 3C 454.3

Normalisation Constant	Index	Curvature
10^{-11} ph cm^{-2} s^{-1} MeV^{-1}	Γ	β
8.6 ± 0.1	2.59 ± 0.01	0.133 ± 0.007

and the value of E_P agreed in 63% of blocks. This suggests that when in its quiescent state 3C 454.3 has a fairly stable spectrum.

We now move on to ask what could cause the observed increases in the flux from the quiescent state. As has been shown (40), changes in the mean energy or energy density of an external photon field do not lead to changes in the bolometric Compton luminosity. However, such changes in the external photon field *do* cause the Compton peak energy to change and this could cause the luminosity that *Fermi* measures to increase if the peak shifted further into *Fermi*'s energy range. Because there is a large difference between the quiescent value and the time-averaged value of the normalisation constant, k, this scenario seems unlikely and changes in the external photon field are therefore disfavoured as the cause of the observed high flux states in the light curve. In an SSC scenario, an increase in the source's B-field could drive an increase in flux and would also increase the value of β (150). This scenario is also disfavoured by our results since β is very consistent between its quiescent value and its time-averaged value.

Additional information can be drawn from the value of the Compton peak energy, E_P. The LP fit to the quiescent state had $E_P = 109 \pm 14$ MeV, which is lower than the time-averaged value of $E_P = 165 \pm 16$ MeV at the 2.6σ significance level. If E_P does indeed increase along with flux then this could be explained by an increase in the Lorentz factor of the emission region (in an SSC scenario) or a change in the population of the electrons in the emission region (in either an EC or an SSC scenario), such as an increase in the acceleration rate. On the other hand, if the difference is purely statistical and E_P remains constant as the flux increases, this could be explained if the emission was EC in origin and flux increases were driven by increases in the Lorentz factor.

To investigate further, for each block in a high flux state we determined E_P from the parameters of the LP fit and compared these high flux values of E_P to the quiescent value. The results are shown in Figure 8.7. No trend in the value for E_P with flux was

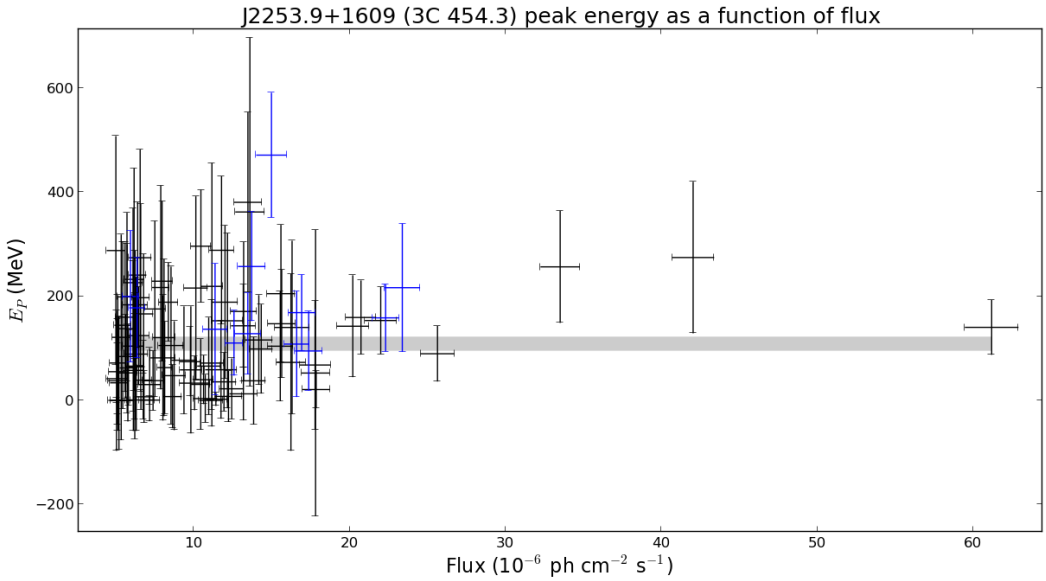

Figure 8.7: Peak energy as a function of flux for 2FGLJ2253.9+1609 (3C 454.3). Data points are shown for all blocks in a high flux state. The shaded band shows the 68% confidence interval for the peak energy in the quiescent state. Blocks best described by an LP are shown in blue.

apparent in the flaring blocks however there are appreciable uncertainties in the data points. The uncertainties are primarily statistical and due to the low photon numbers in each block but the estimated values for E_P should not be systematically biased to higher or lower energies than their true values. The high flux values of E_P scatter roughly equally above and below the quiescent value of E_P, but on average those scattering above deviate from the quiescent value by a greater amount than those scattering below (91 MeV as opposed to 60 MeV). A T-test was performed see if the mean value of E_P from the high flux blocks is consistent with the value of E_P in the quiescent state. The test returned a p-value of 0.14 which suggests that the mean value of E_P in the high flux states is not seen to deviate significantly from the quiescent value, with a roughly 15% probability of occurring by chance.

One way to improve the quality of the data is to include only high flux blocks where the spectrum was significantly better described by an LP. When this is *not* the case, the value of E_P returned by an LP fit is not expected to be physically meaningful: if an LP is not a significant improvement over an SPL then there is a high chance that the LP is

being fitted to noise and if an LP is not a significant improvement over a BPL then the LP is being fitted (poorly) to an additional spectral feature.

When only high flux blocks well-described by an LP are included, a T-test returns a p-value of 0.02 that the values of E_P in the high flux blocks are consistent with the value of E_P in the quiescent state. Although the statistical significance is borderline, this suggests that E_P increases along with flux. The main constraint on the power of this test is the small number of high flux blocks which are included: only 12. Therefore the question should be revisited after more high flux states have been observed.

The cause of spectral breaks

The fact that some blocks in the light curve of 3C 454.3 are significantly better described by BPL is very intriguing. One explanation might be that there is an additional, bright component whose emission is superimposed over the quiescent emission. To test this, all 14 blocks that were best described by BPL spectra were examined to see if they were well described by such a model. The quiescent component was modeled using the parameters found by analysing all of the quiescent blocks together. The additional component was first modelled as an SPL with free parameters and then as an LP with free parameters. In both cases, the difference in AIC showed the BPL model to be a significantly better description than a model with an additional component, so this hypothesis is rejected.

Next it was investigated whether the break energies for blocks best described by a BPL were consistent with the double-absorber model (124). To recap briefly, this model predicts a break at 4.8 GeV in an object's rest frame spectrum due to pair absorption of γ-rays above this energy with low-energy photons from Helium recombination. Such a result would indicate the emission region was within the radius of the BLR. This model was strongly disfavoured in the previous study but it is worth re-testing in the context of high flux periods where a different emission region may be at work than during the quiescent state. Since the double-absorber model also predicts a second break at higher energies which would affect fitting a BPL to the spectrum, to test for a 4.8 GeV break it was necessary to make a high energy cut at 6.5 GeV in the observer frame, as discussed in the previous chapter. The break energies for each block, along with the exclusion confidence of a break at 4.8 GeV, are shown in Table 8.7. In 12 of the 14 blocks which

Table 8.7: Break energies for blocks in the light curve of 2FGLJ2253.9+1609 (3C 454.3) that were best described by a broken power law, and the exclusion confidence of a 4.8 GeV break, as predicted by the double-absorber model (124).

Block start (MJD)	Block Length (Days)	Break Energy (GeV)	4.8 GeV Exclusion Confidence
55089	3	$4.1^{+0.7}_{-0.3}$	65%
55158	2	$4.1^{+1.2}_{-0.6}$	59%
55163	1	4^{+2}_{-2}	53%
55215	2	3^{+1}_{-1}	76%
55289	3	$0.4^{+0.2}_{-0.2}$	84%
55304	3	$1.2^{+0.2}_{-0.3}$	>99%
55459	2	7^{+2}_{-1}	79%
55499	1	$3.2^{+0.7}_{-1.3}$	93%
55503	1	$2.8^{+0.6}_{-0.7}$	83%
55512	1	$5^{+\infty}_{-\infty}$	<1%
55516	2	$5.2^{+1.0}_{-0.8}$	31%
55518	1	$2.1^{+0.7}_{-0.8}$	97%
55555	3	$1.0^{+0.3}_{-0.2}$	>99%
55567	1	$0.6^{+0.2}_{-0.2}$	86%

favoured a BPL spectrum, the break energy predicted by the double-absorber model was excluded with 50% confidence or greater. Although it is worth noting that in 1 case the break appeared where predicted by the double-absorber model, given the total number of trials there is no evidence to favour the double-absorber model and the emission region can be constrained as outside the radius of the BLR.

Likewise, the two component model (61) seemed unable to explain the appearance of BPL blocks. This model predicts an approximately stable break energy and, as can be seen in Table 8.7, the observed break energies display considerable variation.

8.4 Discussion

In this study, 15 BL Lacs and 27 FSRQs were analysed for evidence of curvature or breaks in their spectra. For each source Monte Carlo simulations were performed to determine if confusion with nearby sources was likely to affect the model-fitting procedure. Given the simulation results, 5 BL Lacs and 15 FSRQs were selected from the initial sample to form a clean sample, expected to be free of confusion effects, while the remaining 10 BL Lacs and 12 FSRQs made up an unclean sample.

Within the clean sample, an LP fit was a significantly better description of the data in over half the objects and was an adequate description for the remainder (i.e. neither the SPL nor the BPL were significantly better). Within the unclean sample, there were 3 objects for which a BPL was a significantly better description, roughly half of the objects were significantly better described by an LP, and half showed significant deviation from an SPL but distinguishing between an LP and a BPL was not possible.

The sample sizes being worked with here are fairly small, and some caution should therefore be exercised, but it appears that an LP fit is ubiquitous in the clean sample whereas the unclean sample contains the only objects best fit by BPL spectra and has a higher proportion of objects where distinguishing between an LP and a BPL is not possible. Because of this, it appears that BPL fits result from source confusion. This conclusion was further supported by Monte Carlo simulations using *gtobssim* which showed that a target source with an input LP spectrum could be identified as a BPL spectrum when confusing sources were included.

This conclusion is at odds with previous work, both presented in the preceding chapter and elsewhere in the literature (e.g. (6)), where several bright, clean blazar sources were identified as having BPL spectra. 3 sources, 3C 454.3, PKS 1510-08 and TXS 1520+319, were in the previous chapter identified as having BPL spectra but identified in this study as having LP spectra. Further investigation suggested that the cause of this discrepancy was updating from the P6_V3_DIFFUSE IRF to the P7SOURCE_V6 IRF. In other words, the choice of instrument response function can affect which spectral shape is favoured in a fit. There does not appear to be a systematic bias that makes all fits 'more curved' with the newer Pass7 IRF, but it is telling that now all objects in the clean sample are adequately described by an LP. This is a fairly important result; although people work-

ing in the field can only utilise what is available to them at the time, current work often relies on older work done with older IRFs without analysing the data afresh. This means that several works published after the Pass7 IRF was made available still work on the assumption that a source or sources have BPL spectra, when this is unlikely to be the case (e.g. (105), (47), (129)) and this may alter some of the conclusions of these works.

Further analysis was performed on the FSRQ 3C 454.3, the brightest object in our sample, to try and shed light on the emission processes in this object. Light curve analysis showed that 3C 454.3 appears to have a fairly stable spectrum and is well-described by an LP. By comparing the parameters found by fitting an LP to the quiescent state with those found by fitting to the whole dataset we can constrain the cause of the flux increases. Changes in an external photon field (in an EC scenario) do *not* alter the bolometric luminosity of the Compton emission (40), but do cause the Compton peak energy, E_P to change. Changes in an external photon field therefore could cause the observed luminosity to brighten if E_P shifted further into the LAT's energy range. However, this mechanism was disfavoured since the results showed a significant change in the normalisation constant, k, which suggests that the bolometric luminosity was changing. Similarly, we can rule out changes in the B-field (in an SSC scenario) as the cause of flux increases since such a scenario would lead to an increase in curvature (150) which is not seen.

At the 2.6σ level, E_P appears to increase when high flux states are included in the fit. If E_P does increase along with flux then this indicates that high flux states are caused by an increase in the Lorentz factor of the emission region (in an SSC scenario) or by changes in the population of electrons in the emission region (in either an EC or an SSC scenario) such as an increase in the acceleration rate. Alternatively, if the difference in E_P is purely statistical and the Compton peak energy does not alter with flux then this can be explained if the additional flux is EC in origin and the Lorentz factor of the emission region is increasing.

To investigate further, the value of E_P was found individually for each block with a high flux ($> 5 \times 10^{-6}$ ph cm^{-2} s^{-1}). These values were then compared to the quiescent value of E_P. The high flux values scattered in equal numbers above and below the quiescent value, but those values above the quiescent value tended to deviate further. A T-test to determine if the high flux values of E_P had the same mean as the quiescent value

of E_P returned a p-value of 0.14, i.e. there is a small difference but it is not statistically significant, with a roughly 15% chance that such a deviation could occur by chance.

One further way to improve the data is to look at only those high flux blocks which were described significantly better by an LP, in these cases we can be fairly confident that the value of E_P is meaningful and not the result of fitting noise or other spectral features. A T-test on these values showed a borderline statistical significance with a p-value of 0.02, i.e. there is about a 2% chance that the mean value of E_P in the high flux blocks was consistent with the quiescent value. The biggest constraint in this test was the low number of blocks that were significantly better described by an LP: there were only 12. As it stands, the evidence suggests that the high flux states are caused by an increase in the Lorentz factor of the emission region (in an SSC scenario) or by changes in the population of electrons in the emission region (in either an EC or an SSC scenario), with only a few percent chance that the observed discrepancies occurred by chance. As more high flux states are observed it should be possible to make a more definitive statement either way.

Roughly a dozen blocks in high flux states were best-described by a BPL. The appearance such blocks is intriguing and difficult to explain. The energy of the breaks generally excluded the double-absorber model (124) to a high confidence, suggesting that the emission region was outside the radius of the BLR. The two component model (61) did not seem able to explain the observed BPL spectra either, since this model predicted an approximately stable break energy whilst the break energies showed large variation.

Chapter 9

Photon-axion mixing within the jets of AGN and prospects for detection

9.1 Introduction

As we saw in Chapter 5, VHE γ-ray observations of distant AGN generally result in higher fluxes and harder spectra than expected, resulting in some tension with the level of the extragalactic background light (EBL). If hypothetical axions or axion-like particles (ALPs) were to exist, this tension could be relieved since the oscillation of photons to ALPs would mitigate the effects of EBL absorption and lead to softer inferred intrinsic AGN spectra. In this chapter a research study is presented where the effect of photon-ALP mixing on observed spectra is considered, including the photon-ALP mixing that would occur within AGN jets. Simulated observations of 3 AGN were performed with the CTA to determine its prospects for detecting the signatures of photon-ALP mixing on the spectra. It is concluded that prospects for CTA detecting these signatures or else setting limits on the ALP parameter space are quite promising. The prospects are improved if photon-ALP mixing within the jet is properly considered and it is concluded that the best target for observations is PKS 2155-304.

As we saw in Chapter 5, it was noted several times in the literature that a proportion of the emitted γ-rays may oscillate into ALPs in the B-field surrounding an extragalactic source and these particles would no longer be attenuated by the EBL as they propagate through intergalactic space. A proportion of the ALPs could then oscillate back into γ-

rays in the Milky Way's B-field and in this way provide a boost to the measured γ-ray spectrum. It is not always taken into account that if γ-rays can oscillate into ALPs in the B-field surrounding the source then they must also be subject to oscillations into ALPs *within* the source, since the plasma jet in which γ-ray emission originates is universally accepted to have a B-field. Photon-ALP mixing within the source was considered by Sánchez-Conde et al. (134). However, only the B-field of the small (≤ 0.3 pc) region around the γ-ray emission region was considered, and not the B-field of the rest of the jet through which the γ-rays must propagate. Photon-ALP mixing within an AGN jet was also discussed briefly by Hochmuth and Sigl (77), who considered conversion within a slightly larger (parsec scale) region with a homogeneous B-field. Tavecchio et al. (146) considered mixing in a jet of length 6.7 kpc as a model for the FSRQ PKS 1222+216 and Mena & Razzaque (105) consider mixing in the jet of this object and one other FSRQ object assuming a jet length of 3.2 kpc in each case.

In this project, photon-ALP mixing through jets ranging in length between 0.1 kpc and 100 kpc is considered, with a B-field throughout that decreases steadily from a maximum value at the γ-ray emission region and has random orientations for different cells. Propagation of an initial beam of γ-ray photons through AGN jets of various sizes was simulated and the emitted spectrum was calculated. Simulated observations were then performed to determine how probable it is for the effects of photon-ALP mixing to be observed, both in the case where mixing occurs in the jet and where mixing occurs only outside the jet.

9.2 AGN Jets

By definition, blazars are viewed at a small angle to the jet. While the beaming effects of looking down the jet can create very bright sources it makes determining the jet size and emission region of individual sources difficult. Some inferences can be made from VLBI observations of nearby AGN viewed at large angles to the jet, as we saw in Chapter 4. For Fanaroff-Riley I type galaxies, collimated jets of a few kpc are common (143) and jets of several hundred kpc are known (39). The γ-ray emission region appears to be located relatively close to the base of the jet, at distances < 200 pc (see (49) for VLBI observations and (147) for arguments from GeV energy observations of FSRQ type blazars). This

suggests that, in general, the distance from the emission region to the termination of the jet ΔZ is > 1 kpc. Disruption of the jet close to its base means that ΔZ could be significantly smaller in some objects, although there is less chance of this being the case in brighter objects (39). These considerations lead us to consider several values of ΔZ in this work: 0.1, 1, 10 and 100 kpc.

9.2.1 Modelling

In this subsection we consider propagation of γ-rays through a jet with oscillation to ALPs along its length. The γ-ray spectrum is based on the measurement of the BL Lac object 1ES 1101-232 and the underlying physical parameters are based on the subsequent modelling (23). At the emission region the electron density was therefore $K_0 = 900\,\mathrm{cm}^{-3}$ and B-field strength was $B_0 = 1$ G, which is consistent with the average value for the B-field found for the emission region of γ-ray loud BL Lacs in the study by Ghisellini et al. (68). The γ-ray flux F at energy E_γ is therefore given by

$$F(E_\gamma) = 5.6 \times 10^{-13} \left(\frac{E_\gamma}{1\ \mathrm{TeV}}\right)^{-2.94}\ \mathrm{ph\ cm^{-2}\ s^{-1}\ TeV^{-1}}, \tag{9.1}$$

where $1\,\mathrm{MeV} \leq \mathrm{E}_\gamma \leq 10\,\mathrm{TeV}$. This is a considerable extrapolation from the measurement (23), but this is not important for our current purposes where we wish only to test the effects of photon-ALP oscillation over a wide energy range and are not too concerned about the actual spectral shape at this stage. The extrapolation below a few tens of GeV would be below the sensitivity threshold for CTA, but was included in the modelling of the jet as effects in this range could be detected by other instruments e.g. the LAT.

The jet model used in this project was based loosely on the fundamental model presented by Blandford and Königl (37). The jet was assumed to have a constant opening angle $\phi = 0.1°$ relating the jet radius R to distance from the base of the jet Z as follows:

$$R(Z) = \phi \cdot Z. \tag{9.2}$$

The γ-ray emission region was set at a distance $Z_0 = 1$ pc from the base of the jet and the jet terminated at a distance $Z_{max} = Z_0 + \Delta Z$ where ΔZ was taken as 0.1, 1, 10 and 100 kpc. The electron density and the B-field strength at the emission region, K_0 and B_0, were the maximum values for these parameters. Magnetic energy and particle number

were conserved as Z increases and the jet widens such that

$$K(Z) = K_0 \left(\frac{Z_0}{Z}\right)^2, \tag{9.3}$$

$$B(Z) = B_0 \left(\frac{Z_0}{Z}\right). \tag{9.4}$$

Following Sánchez-Conde et al. (134) the coherence length of the B-field (the distance over which the direction of the B-field is constant) was taken to be 3×10^{-3} pc. Beginning with a pure photon beam with 20 energy bins, evenly spaced on a logarithmic scale, the fraction of photons oscillating into ALPs and vice versa was calculated when travelling over cells of one coherence length.

This jet model, although simplistic, covered all the salient points for this project. That is, the γ-rays were emitted relatively close to the base of the jet and must propagate large distances and many coherence lengths of a B-field of changing strength. As discussed later, the conclusions of this work should not be affected if the γ-ray emission region has a larger B-field or particle density than its surroundings, such as for blob-in-jet (86) or magnetic reconnection (99) scenarios.

9.3 Photon ALP mixing

9.3.1 Mixing Equations

Following (79), the ALP coupling constant is taken as $g = 5 \times 10^{-11}$ GeV^{-1} and the ALP mass as $m_a = 1 \times 10^{-8}$ eV, which are within the constraints determined by the CAST experiment (26).The equations for photon-ALP mixing were given at the end of Chapter 5, but it is worthwhile summarising them here. The probability for a phooton of energy E_γ to convert to an ALP or vice versa is given as

$$P_0 = 2 \left(\frac{\Delta_B}{\Delta_{osc}}\right)^2 \sin^2 \left(\frac{\Delta_{osc} \cdot s}{2}\right). \tag{9.5}$$

where

$$\Delta_B = 7.6 \times 10^{-2} \left(\frac{g}{5 \times 10^{-11}\ \mathrm{GeV}^{-1}}\right) \left(\frac{B_T}{10^{-6}\ \mathrm{G}}\right)\ \mathrm{kpc}^{-1}, \tag{9.6}$$

$$\Delta_{osc} = \Big((\Delta_{CM} + \Delta_{pl} - \Delta_a)^2 + 4\Delta_B^2 \Big)^{\frac{1}{2}}\ \mathrm{kpc}^{-1}, \tag{9.7}$$

$$\Delta_{CM} = -4 \times 10^{-6} \left(\frac{B_T}{10^{-6}\ \mathrm{G}} \right)^2 \left(\frac{E_\gamma}{\mathrm{TeV}} \right)\ \mathrm{kpc}^{-1}, \tag{9.8}$$

$$\Delta_{pl} = 1.1 \times 10^{-10} \left(\frac{E_\gamma}{\mathrm{TeV}} \right)^{-1} \left(\frac{K}{10^{-3}\ \mathrm{cm}^{-3}} \right)\ \mathrm{kpc}^{-1}, \tag{9.9}$$

$$\Delta_a = 7.8 \times 10^{-3} \left(\frac{m_a}{10^{-8}\ \mathrm{eV}} \right)^2 \left(\frac{E_\gamma}{\mathrm{TeV}} \right)^{-1}\ \mathrm{kpc}^{1}. \tag{9.10}$$

For the values relevant to this work, Faraday rotation effects can be neglected (65). When $P_0 \simeq 1$, photon-ALP conversion is saturated, since for every photon converting into an ALP there is also an ALP converting to a photon. Over energies where this strong mixing occurs, the intrinsic spectral shape is unaltered but the photon flux will drop by $\frac{1}{3}$ due to their conversion to axions (for an unpolarised photon beam as is assumed here).

We can see from Equation 9.5 that there are two conditions to be met for strong photon-ALP mixing to take place. The first condition is that the argument of the $\sin^2$ term is non-negligible,

$$\frac{\Delta_{osc} \cdot s}{2} \gg 0. \tag{9.11}$$

Δ_{osc} can only be consistently small if the strength of the B-field is small[1]. In this case,

$$\Delta_{osc} \simeq \sqrt{(\Delta_{pl} - \Delta_a)^2}. \tag{9.12}$$

Δ_{pl} is a function of the electron density which, unless ΔZ is very small, varies over several orders of magnitude. Δ_a on the other hand is a function only of the ALP mass (which is fixed) and photon energy. For this work, $1\ \mathrm{MeV} \leq \mathrm{E}_\gamma \leq 10\ \mathrm{TeV}$ which leads to $3 \times 10^{11} \leq \Delta_a \leq 3 \times 10^{17}\ \mathrm{kpc}^{-1}$. Given the coherence path length adopted in this work of $s = 3 \times 10^{-3}\ \mathrm{pc}$, Equation 9.11 is easily satisfied for much of the jet.

The second condition for strong mixing is

$$2 \left(\frac{\Delta_B}{\Delta_{osc}} \right)^2 \simeq 1, \tag{9.13}$$

Δ_B is dependent on the strength of the B-field and Δ_{osc} is dependent on both this and the electron density. Unless ΔZ is very small, these quantities vary over orders of magnitude through the jet, and for much of the jet Equation 9.13 will be satisfied.

At the very highest values of photon energy, E_γ, the Cotton-Mouton term described in Equation 9.8 becomes important. Unless B_T is small, $\Delta_{CM} \gg \Delta_B$ and will dominate

[1]It is of course small if B_T is small solely due to the angle of photon propagation with respect to the B-field, but on average this will not be the case.

Δ_{osc}, meaning that Equation 9.13 will no longer be satisfied. If ΔZ is small, conservation of magnetic energy dictates that B_T is generally large and so photon-ALP mixing is suppressed at high energies.

As pointed out in Ref (28), it can be useful to define a critical energy

$$E_c = \frac{5 \times 10^{-2} |m_a^2 - \omega_{pl}^2|}{(10^{-8}\ \mathrm{eV})^2} \left(\frac{10^{-6}\ \mathrm{G}}{B_T}\right) \left(\frac{5 \times 10^{-11}\ \mathrm{GeV}^{-1}}{g}\right)\ \mathrm{TeV}, \tag{9.14}$$

where $\omega_{pl} = -2E\Delta_{pl}$. This allows us to rewrite Equation 9.5 as

$$P_0 = \frac{1}{1 + \left(\frac{E_c}{E}\right)^2} \sin^2\left(\frac{\Delta_{osc} \cdot s}{2}\right). \tag{9.15}$$

From this we can see that below E_c there is little photon-ALP oscillation and above E_c there is potentially significant photon-ALP oscillation, a fact we shall refer to later.

9.3.2 Mixing within AGN jets

At this stage we are ready to examine the output of the models described in Section 9.2.1. It was found that due to the large number of cells ($> 1 \times 10^4$) the random orientations of the B-field in each cell had negligible effects on the results. Figures 9.1 and 9.2 show the intrinsic and emitted spectra for AGN with different values of ΔZ and Figure 9.3 shows the probabilities of photons of various energies converting into an ALP at least once, as function of distance from the emission region. As expected from the discussion in Section 9.3.1, strong photon-ALP mixing occurs for large ranges of E_γ, altering the photon flux but leaving the spectral shape the same, until Cotton-Mouton effects suppress mixing at high energies. It was found that for $\Delta Z = 0.1\ \mathrm{kpc}$ Cotton-Mouton suppression occurs at $\approx 1.7\ \mathrm{TeV}$ resulting in a boost in the photon flux above this energy. For larger values of ΔZ, Cotton- Mouton suppression occurs at such high energies that the effect is negligible over the energy range considered in this study. Since no change in the spectral shape is seen below $E(\gamma) \approx 1.7\ \mathrm{TeV}$ instruments operating below this energy, e.g. the LAT, would not be expected to detect any effects due to photon-ALP mixing within the jet for the ALP parameters assumed here.

Before moving on we should note that when considering propagation over many coherence lengths, as we are here, the conversions should properly be treated as a 3-dimensional problem. Relative to the direction of propagation, the photons can have 2 directions of polarisation. As we saw, photon-ALP oscillation is only dependent on the

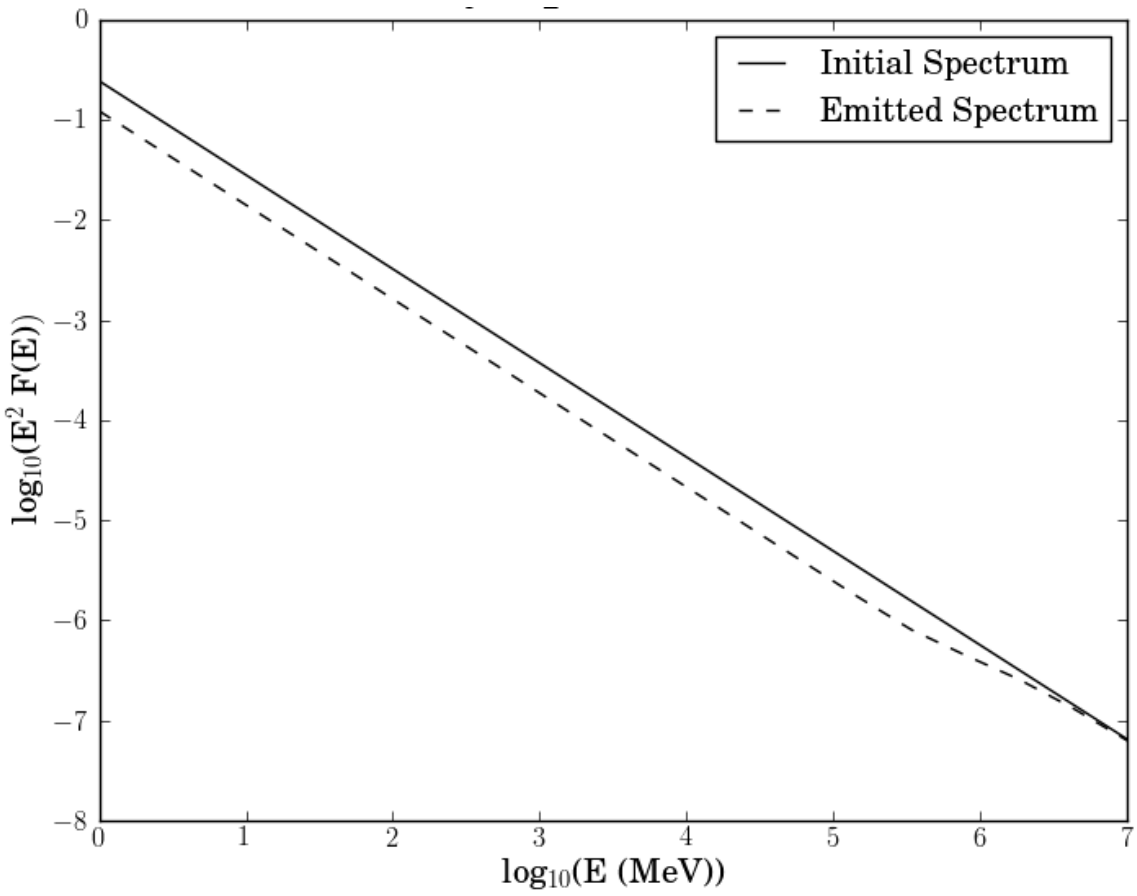

Figure 9.1: The intrinsic photon spectrum before any mixing with ALPs and the emitted photon spectrum after travelling 0.1 kpc from the emission region while undergoing mixing with ALPs. F is the flux as a function of E in arbitrary units.

transverse strength of the B-field so each polarisation state interacts separately. The axion field comprises the third degree of freedom. In this work the the polarisation of photons was neglected, and the equations in Section 9.3.1 are derived from a 2-dimensional treatment. This will limit the accuracy of the results, but since the photon-ALP mixing probability is close to unity when outside the Cotton-Mouton regime and close to zero when inside, with a very sharp transition, it will not affect the conclusions. Even if this were not the case, it would be expected that the results would be correct to within an order of magnitude, which is adequate given the larger uncertainties being dealt with such as the ALP mass and the length of the AGN jet.

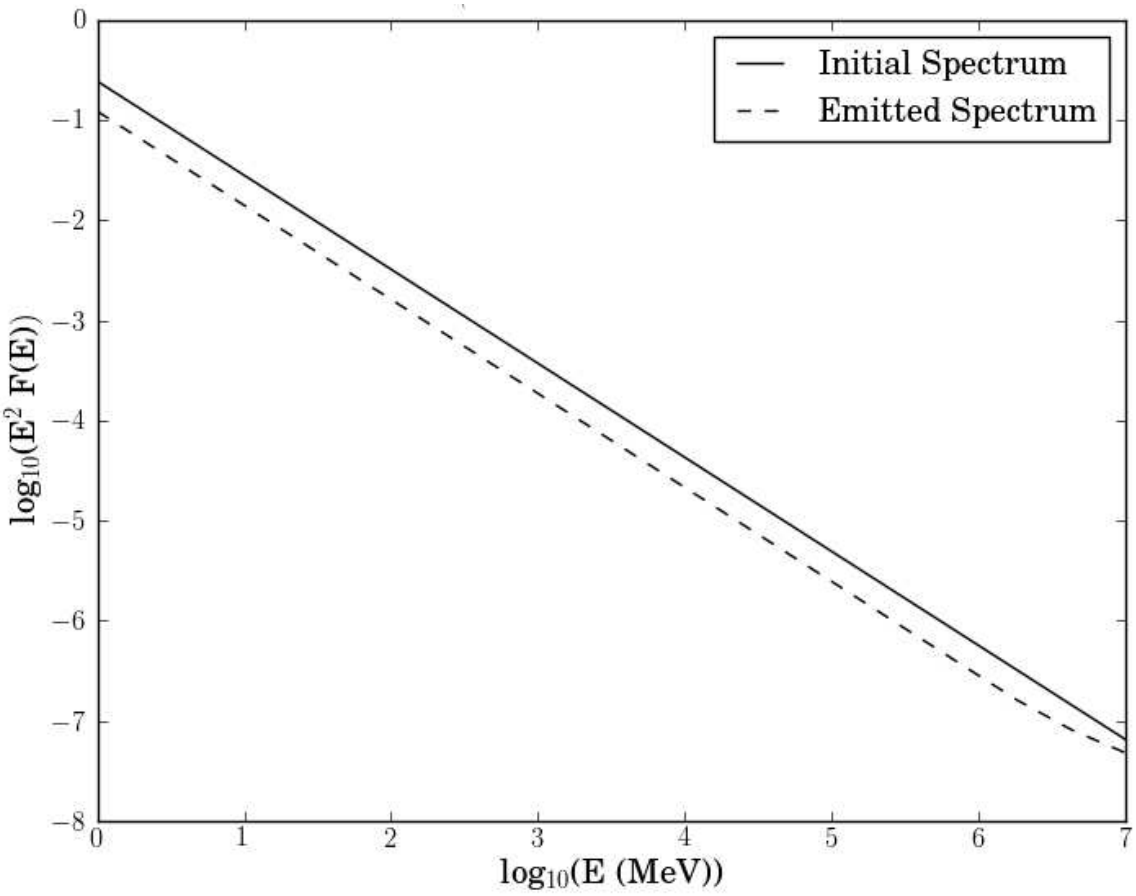

Figure 9.2: The intrinsic photon spectrum before any mixing with ALPs and the emitted photon spectrum after travelling 1 kpc from the emission region while undergoing mixing with ALPs. F is the flux as a function of E in arbitrary units.

9.4 Prospects for observing photon-ALP mixing effects

9.4.1 The Cherenkov Telescope Array

The exact telescope layout for CTA is as yet undecided and several proposed layouts have been characterised through extensive Monte Carlo design studies including calculating the effective area for numerous energy bins (36). In this work observations were simulated using the results for the proposed layout E for the Southern array (123), which contains 4 large (≈ 24 m primary mirror diameter) size telescopes, 23 medium (≈ 12 m) size telescopes, and 32 small ($\approx$ 4-7 m) size telescopes.

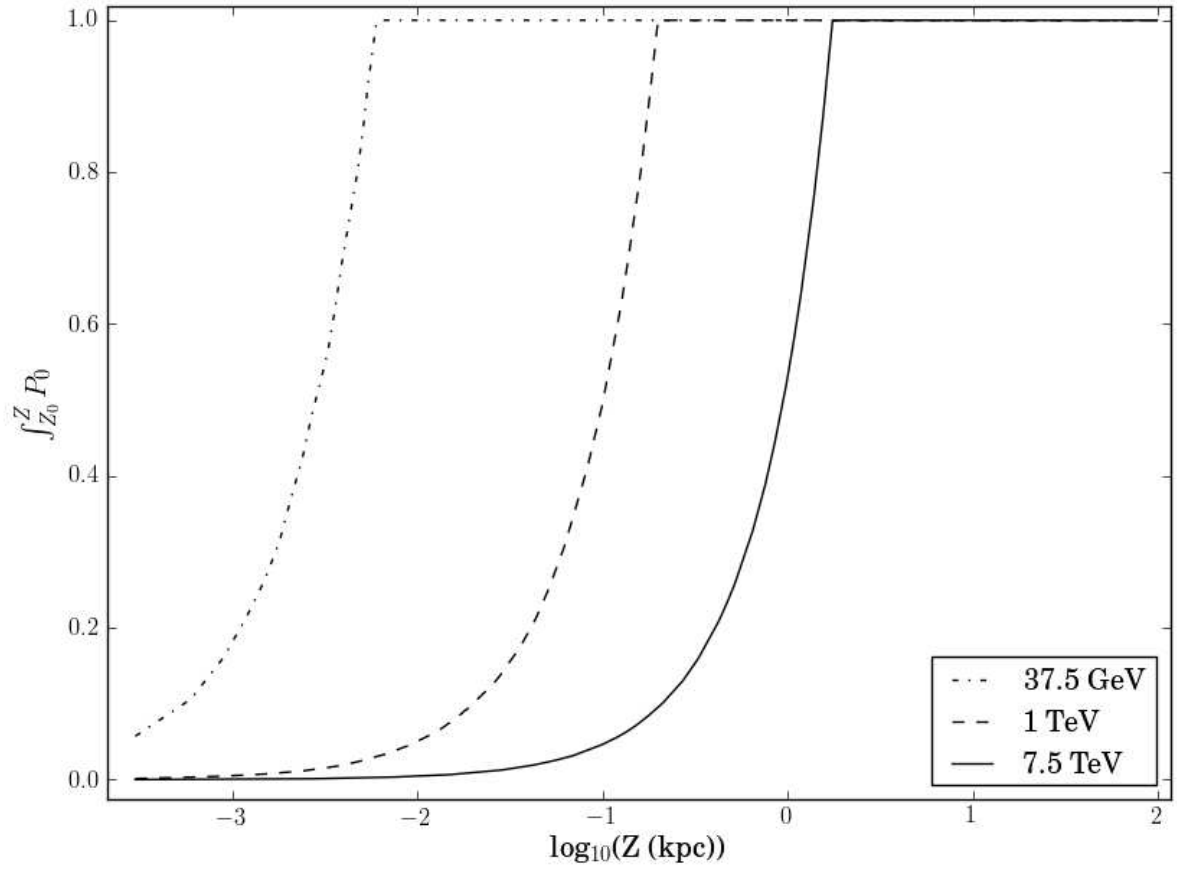

Figure 9.3: The probability for (from left to right) a photon of 37.5 GeV, 1 TeV and 7.5 TeV converting into an axion at least once as a function of distance from the emission region.

9.4.2 Target Objects

For this study, 3 blazars were chosen for simulated observations which are listed in Table 9.1 along with their spectral parameters. The spectrum of each object has the form

$$F(E_\gamma) = k \left(\frac{E_\gamma}{E_0} \right)^{-\Gamma}, \tag{9.16}$$

where k is the flux constant, E_0 is the flux normalisation and Γ is the spectral index.

All 3 objects reside within a galaxy cluster and so, neglecting any conversion within the jet, it is expected that a fraction of roughly 0.3 of the photons convert into ALPs before traversing the IGM (79). If there is conversion within the jet then a total fraction of ~ 0.4 photons convert to ALPs before crossing the IGM ($\frac{1}{3}$ of photons convert to ALPs within the jet, 0.3 of these convert back into photons in the B-field of the cluster, and 0.3 of the remaining $\frac{2}{3}$ of photons convert to ALPs). Both scenarios were considered in this

project.

The first object is 1ES 1101-232. At redshift $z = 0.186$ it is relatively distant by the standards of VHE sources but is also observed to be relatively bright (23). Observations also show that it has a hard spectral index which leads to reasonable photon numbers at the highest energies where EBL absorption is highest and therefore any mitigation of the absorption is most easily spotted.

The second object considered is PKS 2005-489. This object was chosen primarily because with a redshift of $z = 0.071$ it is one of the closest blazars seen at VHE in the Southern hemisphere and this makes the effects of the EBL on the spectrum less model-dependent as we shall see in the following subsection. Also, from Figure 4 of (10), it can be seen that there is a slight rise in flux at a few TeV. This might be construed as evidence of a flux boost from the onset of Cotton-Mouton suppression, although with current observations the effect is not statistically significant, and a simple power law fit to the data provides an adequate χ^2.

The third object considered is PKS 2155-304, at $z = 0.117$, basing the spectrum on parameters in the quiescent state (8). This object was chosen as it is one of the brightest blazars at TeV energies.

The fraction of ALPs that reconvert in the Milky Way depends upon the line of sight from Earth to the object. Estimates for the fraction of photon-ALP conversion in the Milky Way's B-field using the model of Jansson & Farrar (82) for each object are shown in Table 9.1. A very low fraction of 0.05, consistent with the lower estimate B-field model of Pshirkov et al. (126) was also used. As we saw earlier, photon-ALP oscillation is only non-negligible above a certain critical energy. Under the model of Jansson and Farrar (82), this energy is quite low. In the case of PKS 2005-489 and PKS 2155-304 it is $0.016\ \mathrm{TeV}$ and $0.019\ \mathrm{TeV}$ respectively, below the energy threshold of CTA, and for 1ES 1101-232 it is $0.045\ \mathrm{TeV}$ and only the lowest energy bin of the effective area would be below the critical energy. Since in practice this region would be subject to quite poor energy resolution this bin was also treated as also being above the critical energy. For the model of Pshirkov et al. (126), with the low value of B-field, the critical energy was calculated to be $0.2\ \mathrm{TeV}$.

Table 9.1: Target objects for simulations.

Object Name	Redshift	Flux Constant $\mathrm{ph\ cm^{-2}\ s^{-1}\ TeV^{-1}}$	Flux Normalisation TeV	Spectral Index (Γ)	Reconversion Frac[a]	Ref
1ES 1101-232	0.186	5.6×10^{-13}	1	2.94	0.25	(23)
PKS 2155-304	0.117	1.9×10^{-12}	1	3.53	0.60	(8)[b]
PKS 2005-489	0.071	1.4×10^{-11}	0.4	3.20	0.70	(10)

[a]Reconversion of ALPs to photons in the Milky Way B-field assuming the model of Jansson & Farrar (82).

[b]Quiescent State

9.4.3 EBL models

As we saw in Chapter 5, EBL absorption can have significant effects on a spectrum, especially at high redshifts, so the choice of EBL model used could prove important. This project made use of 2 models of the EBL. The first was that of Kneiske and Dole (88) which aims to provide a lower limit for the level of the EBL. In this model certain tracers for star formation such as *Lyman-*α emission were used to infer the level of star formation as a function of redshift. From this the EBL level was computed by fitting star formation models to the inferred lower limits.

The second model used is that of Franceschini, Rodighiero and Vaccari (63) which provides a more typical estimate than the lower limit model. In this model the EBL level was estimated by taking galaxy counts and attaching to each object an appropriate multiwavelength spectrum based on the galaxy type (e.g. AGN, starburst). These spectra were modelled on local observations and evolved backwards to the appropriate redshift following a simple phenomenological model.

Both models agree with the consensus that there are 2 peaks in the spectrum of EBL intensity, one at $\sim 1\ \mu\mathrm{m}$ and another at $\sim 100\ \mu\mathrm{m}$. However, there are significant differences between the models which become particularly apparent at high energies. The optical depths of these two EBL models as a function of energy, at the redshift of 1ES 1101-232, are shown in Figure 9.4.

9.4.4 Simulated Observations

We now proceed to see how probable it is that CTA will be able to detect changes in the spectra of the target objects due to photon-ALP oscillation. From our discussion so far,

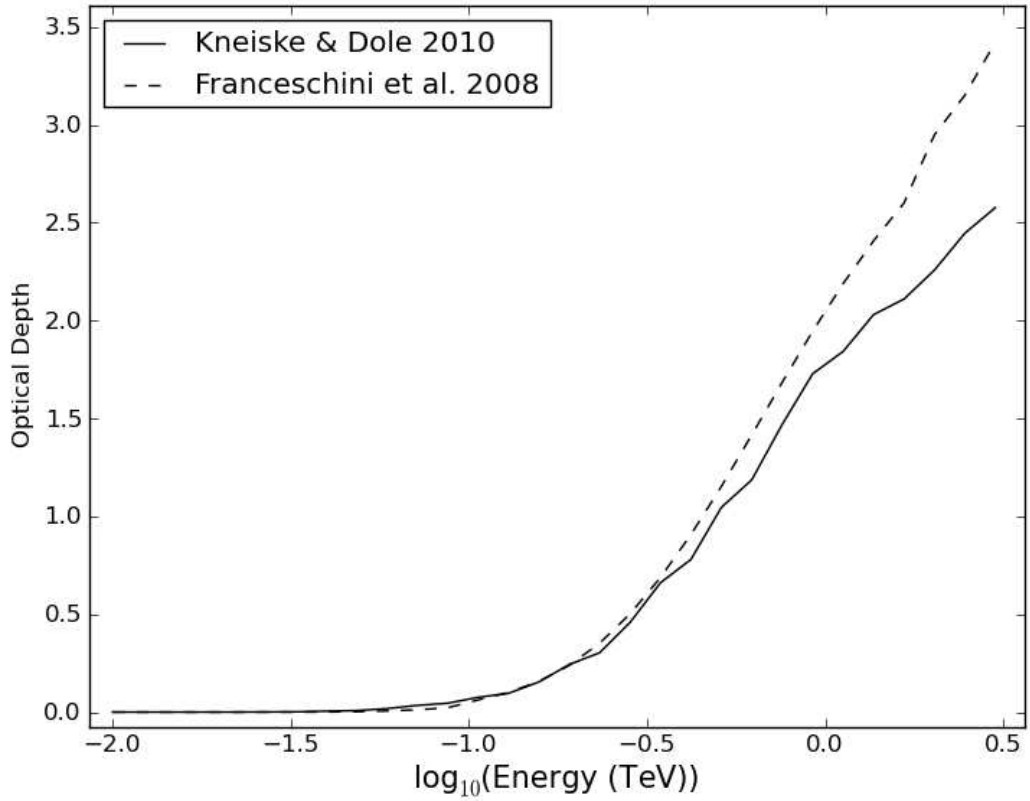

Figure 9.4: Comparison of optical depths for the two EBL models used in this paper as a function of energy. These results are for the redshift of 1ES 1101-232, z=0.186.

we know that the way in which the spectral shape of an object is altered by photon-ALP oscillation depends on several factors, namely: the value of ΔZ, the shape of the EBL, the structure of the Milky Way's B-field, and whether photon-ALP oscillation occurs in the jet.

For each target 1000 observations with CTA were simulated using the effective area curve calculated via Monte Carlo simulations of the proposed layout Array E, described in Ref (36). In order to test the relevant factors the following cases were considered:

- The case where Cotton-Mouton suppression is important ($\Delta Z = 0.1$ kpc, leading to a flux boost at 1.7 TeV).
- The case where Cotton-Mouton suppression is not important.
- The case where there is no photon-ALP conversion within the jet at all.

Both EBL and Milky Way B-field models discussed in the previous sub-sections were

considered for each case. For each scenario the intrinsic spectral parameters of the source were altered such that the measured spectrum would be consistent with current observations. This was done by altering the flux constant and spectral index of the intrinsic spectrum so that a fit to the spectrum after EBL effects returned the values quoted in Table 9.1, within errors.

For each simulation 50 hours of observation and a signal-free background 'OFF' region (or regions) 10 times larger than the signal 'ON' region were assumed. (Background events are assumed to be cosmic rays with spectra based on measurements from several instruments, see Sections 7.1 and 8.1 of (36).) A simulated observation was performed as follows:

- The photon flux from the emission region was calculated for each energy bin.
- To represent photon-ALP mixing within the jet and in the magnetic field surrounding the object, a fraction of this flux was converted into an ALP flux. The fraction was based on the particular scenario: 0.4 if there is conversion within the jet, 0.3 if not, and no conversion in energy bins suppressed by Cotton-Mouton effects.
- EBL absorption was applied to the photon flux based on the particular scenario, representing the beam crossing intergalactic space.
- A fraction of photons was converted into ALPs in the Milky Way magnetic field based on the particular scenario, as shown in Table 9.2. These particles were then discarded from the simulation. A fraction of the ALP flux was then converted to photons and added to the photon flux.
- The number of events in the ON region was determined by drawing both the source events and the background events from Poisson distributions about their expected values.
- The number of events in the OFF region(s) was determined by drawing events from a Poisson distribution about the expected value. This value was then used to calculate the expected number of background events in the ON region, based on the difference in size between the ON and OFF regions.
- The expected number of background events was subtracted from the number of

recorded events in the ON region in order to estimate the number of events from the source. This was then converted into an energy flux.

- In order to ensure a decent signal-to-noise ratio, at least 5 estimated source events were required in a bin for it to be analysed.

The simulated spectrum was then fitted with 2 models. In the first model, ALPs were not included and the flux normalisation and spectral index were the only free parameters. In the second model, the fraction of photons converting to ALPs before traversing the IGM was also a free parameter. In each case, both the generating model and the fitted model used the same EBL model, Milky Way B-field model and, where appropriate, Cotton-Mouton suppression.

To see if including ALPs in the model significantly improved the fit, the likelihood of each model, given the simulated data, was calculated and compared using an AIC test. Some examples of simulated spectra which are fitted significantly better by a model with ALPs (compared to a model without ALPs) are shown in Figures 9.5 - 9.8.

Table 9.2 shows the percentage of the 1000 simulations for which there is a detection of significant effects in the spectrum due to photon-ALP mixing, i.e. including ALPs in the model provides a significant improvement to fitting the measured spectrum compared to not including them. From here on I shall refer to a significant detection of photon-ALP mixing effects as the detection of a 'signature'.

The model of the Milky Way's B-field is a larger influence on the results than the EBL model, although both are important. With the Milky Way B-field model of Jansson and Farrar (82) prospects for detecting a signature are very good with $> 60\%$ chance for all 3 objects. Including the effects of photon-ALP mixing within the jet typically adds 5-10% chance to the prospects of detecting a signature. If the jet is assumed to be short, $\Delta Z = 0.1$ kpc, the flux boost due to Cotton-Mouton suppression typically adds 30% or more to the chances of detecting a signature.

As can be seen, PKS 2155-304 is the most promising target, presumably due to its brightness. Even with the more pessimistic Milky Way model in which only a fraction of 0.05 of ALPs reconvert, detection prospects are always above 50%. An example of a detection of a signature in one of the more pessimistic scenarios (high EBL absorption but pessimistic Milky Way model, no ALP conversion within the jet and no Cotton-Mouton suppresion boost) is shown in Figure 9.5. As expected, the difference between

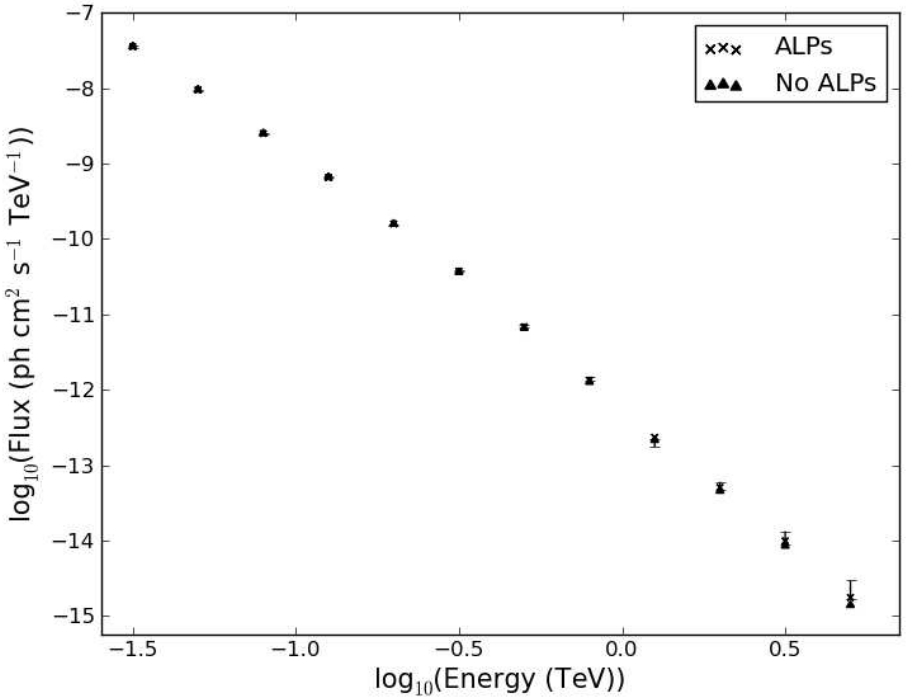

Figure 9.5: Example of a simulated spectrum of PKS 2155-304 where the effect of photon-ALP mixing is significant. Error bars indicate the 1σ statistical uncertainty on the measured photon flux in each energy bin. EBL model used is that of Franceschini, Rodighiero & Vaccari (63), with mixing occurring in the B-field of the host galaxy cluster and using the pessimistic Milky Way B-field level. A model including ALPs fitted to the data is shown with crosses and a model with no ALPs fitted to the data is shown with triangles.

the 2 model fits is most pronounced at the high energy part of the spectrum, shown in detail in Figure 9.6, where the model with no ALPs suffers more severe absorption with the EBL.

For 1ES 1101-232 the detection prospects are still good, again over 50% in all the scenarios considered here. An example of a spectrum with a a significant detection of a signature is shown in Figure 9.7 (low EBL absorption, ALP conversion within the jet and no Cotton-Mouton supression boost). Again, most of the deviation between the different fits is seen in the high energy part of the spectrum.

PKS 2005-489 shows a wider variation in the prospects for detecting a signature. Prospects are as low as 11% in the most pessimistic scenario, but there is a 100% chance

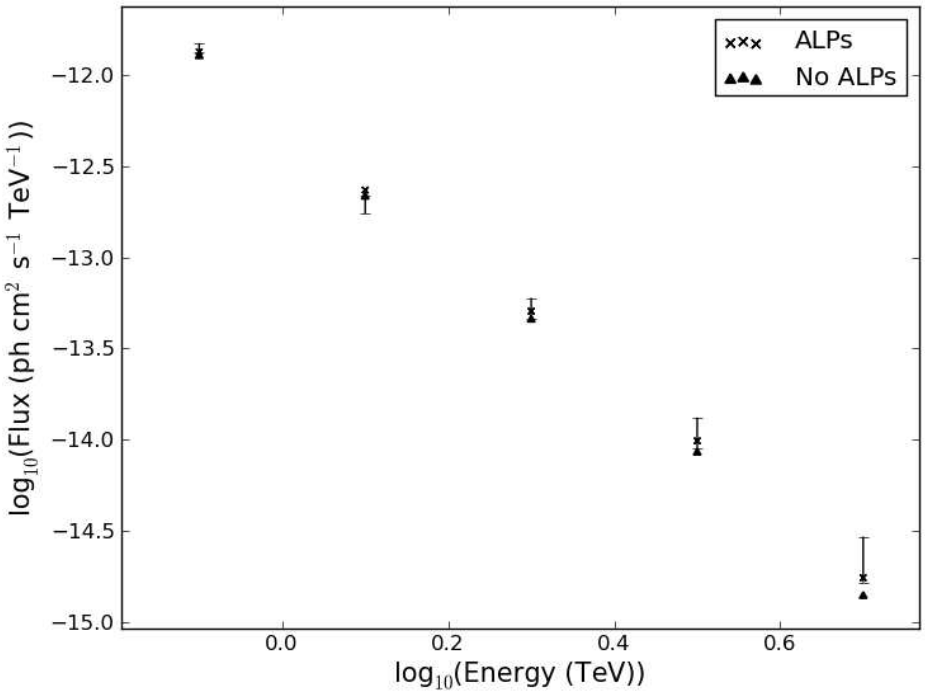

Figure 9.6: Detail of the high energy part of Figure 9.5.

of detecting a signature if $\Delta Z = 0.1$ kpc. This can be understood when we consider the object's relative closeness, in which case the additional γ-rays produced at the highest energies do not suffer much absorption from the EBL. This can be seen in Figure 9.8, where an example of a spectrum is shown where Cotton-Mouton supression occurs at 1.7 TeV in the object rest frame. This is seen as a corresponding flux boost in the final 3 energy bins which the model without ALPs cannot fit, leading to a significant detection of the signature.

9.5 Discussion

If the hypothetical axions or axion-like particles (ALPs) exist, then photon-ALP oscillation would be possible in the presence of a B-field. This study considered the conversion of γ-ray photons to ALPs in the B-field of AGN jets and in the B-field external to AGN jets. The probability of CTA detecting the signature of photon-ALP mixing was then calculated for 3 objects: 1ES 1101-232, PKS 2155-304, and PKS 2005-489. Such signatures can

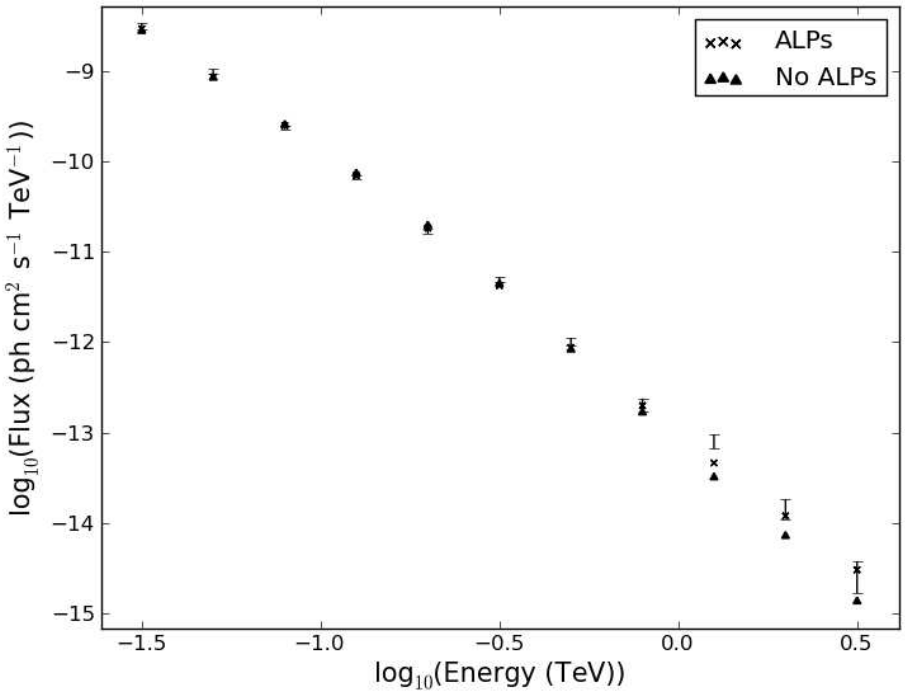

Figure 9.7: Example of a simulated spectrum of 1ES 1101-232 where the effect of photon-ALP mixing is significant. Error bars indicate the 1σ statistical uncertainty on the measured photon flux in each energy bin. EBL model used is that of Kneiske & Dole (88), with mixing occurring in the jet and in the B-field of the host galaxy cluster and using the Milky Way B-field model of Jansson & Farrar (82). A model including ALPs fitted to the data is shown with crosses and a model with no ALPs fitted to the data is shown with triangles.

be due to changes in the emitted spectra caused by photon-ALP mixing within the jet as well as ALPs mitigating the absorption effects of low energy extragalactic background light (EBL) photons on γ-rays. The prospects for detecting the signature of photon-ALP mixing in the spectra of an object vary between 11% and 100% depending upon assumptions in the EBL model, the Milky Way B-field model, and the length of the jet. The assumptions about the Milky Way B-field model appear to have a bigger impact on the results than the assumptions about the EBL model, although both are important. The most consistently promising target is PKS 2155-304, which suggests that observations should target relatively bright, nearby objects as well as distant hard-spectrum sources.

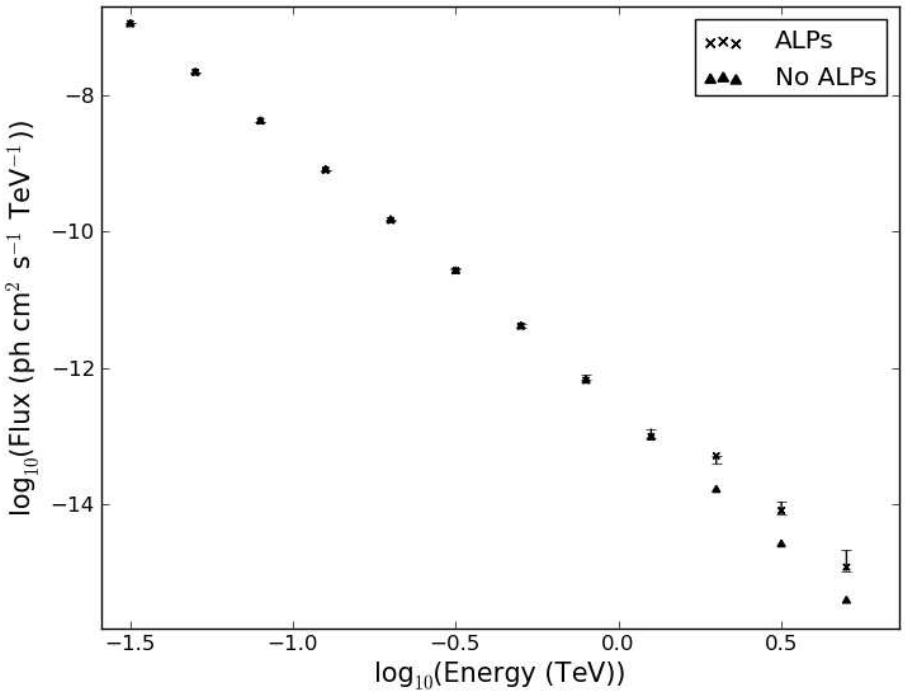

Figure 9.8: Example of a simulated spectrum of PKS 2005-489 where the effect of photon-ALP mixing is significant. Error bars indicate the 1σ statistical uncertainty on the measured photon flux in each energy bin. EBL model used is that of Franceschini, Rodighiero & Vaccari (63), with mixing occurring in the jet and in the B-field of the host galaxy cluster and using the pessimistic Milky Way B-field level. A model including ALPs fitted to the data is shown with crosses and a model with no ALPs fitted to the data is shown with triangles.

Throughout this work an ALP mass 10^{-8} eV and coupling constant of 5×10^{-11} GeV^{-1} have been assumed. In the jet model used, photons are initially emitted near the base of the jet and propagate up to the jet termination. The jet conserves particle (electron) number and magnetic energy as it widens, which means that the particle density and B-field strength decrease with distance from the emission region.

It is found that, in general, due to the wide range of particle densities and B-field strengths the photon beam passes through as it travels up the jet, the effects of photon-ALP mixing preserve the spectral index of the γ-ray spectrum. Including the effects of photon-ALP mixing within the jet typically provide an additional 5-10% chance of de-

Table 9.2: Percentage of simulations where including photon-ALP conversion in the model fitted to the measured spectrum is a significant improvement.

		Kneiske & Dole			Francheshini et al.		
Object	Reconversion	Conv	No Conv	$\Delta Z =$	Conv	No Conv	$\Delta Z =$
Name	Fraction	in Jet	in Jet	0.1 kpc	in Jet	in Jet	0.1 kpc
1ES 1101-232	0.25	81%	73%	86%	93%	88%	79%
	0.05	54%	54%	96%	63%	61%	84%
PKS 2155-304	0.60	100%	100%	100%	100%	100%	100%
	0.05	76%	65%	100%	68%	54%	100%
PKS 2005-489	0.70	71%	60%	100%	91%	84%	100%
	0.05	15%	11%	100%	25%	19%	100%

tecting a signature, compared with assuming that photon-ALP mixing occurs only outside the jet, e.g. in the B-field of the host galaxy cluster. It also means that γ-rays emitted from blazars not hosted within a galaxy cluster will undergo photon-ALP mixing and may produce detectable signatures.

If the emission region is close to the termination of the jet, $\Delta Z = 0.1$ kpc, then the prospects for detecting a signature see a large increase, especially in PKS 2005-489. This is due to a sudden jump in γ-ray flux where Cotton-Mouton suppression occurs at around 1.7 TeV in the object's rest frame. This suggests a search strategy of looking at relatively nearby blazars where these additional γ-rays do not suffer much absorption with the EBL. However, in general ΔZ would be expected to be much larger than 0.1 kpc. Furthermore, Cotton-Mouton suppression could reasonably be assumed to occur at higher energies where photon numbers are poorer even if $\Delta Z \leq 0.1$ kpc. If the γ-ray emission originated in a small region close to the termination of the jet, for example due to magnetic reconnection, the B-field strength immediately outside the emission region might be small. Similarly, even if the jet is disrupted close to the central black hole causing a small ΔZ, small B-field strengths may be encountered in the disrupted material beyond the termination of the jet. In these cases the lower B-field strengths would push the Cotton-Mouton suppression to higher energies.

Other effects not considered here may degrade the prospects of detecting a signature, although not dramatically. Firstly, the CTA's energy resolution will not be perfect, caus-

ing a smearing of the flux boost at high energies, which was not included in these simulations. Secondly, the spectra of the objects were treated as simple power laws when in reality they may have curvature. This would lower the flux at higher energies but again this would not be expected to have a large effect on the results, especially taking into account the range of spectral parameters considered in this study.

As well as the 3 targets considered in this study, several other promising targets exist such as PKS 0301-243, 3C 279 and PKS 1424+240. There are no compelling a priori reasons to assume that the EBL should be at its lower limits across a wide range of wavelengths or to assume that no photon-ALP mixing would occur within the jet. Therefore, if ALPs exist with the parameters assumed here, signatures are expected to be seen in the spectra of several objects. Conversely, if the effects are not seen, limits can be placed on the ALP parameter space.

Chapter 10

Summary and Look Forward

This thesis is concerned with the physics that can be learnt from studying the γ-ray spectra of blazars. Chapter 1 provided an overview of the field of γ-ray astronomy and the related field of cosmic ray astronomy. This started with a brief history of the fields including past and present telescopes based on Earth and in orbit. Particular attention was given to the space-based *Fermi*-LAT, currently the leading space-based instrument which was used extensively in research presented in this thesis. The number and type of different γ-ray sources were also discussed and we saw that several hundred blazars have been detected by the LAT and that these observations are complemented by those of ground-based telescopes which operate at higher energies. A brief discussion was then given of CTA, a next generation ground-based telescope currently in its preparatory phase.

Chapter 2 covered the instruments and techniques of the field in more detail. This began with a discussion of the LAT and the principle of pair-production on which it operates. The LAT data analysis techniques relevant to this thesis were then covered: in particular how to perform likelihood analyses to measure the spectra of target sources and how Monte Carlo simulated observations can be performed. Next the principle of Cherenkov radiation or Cherenkov light was discussed. This is the light generated when a charged particle moves through a dielectric medium with speed greater than the speed of light in that medium. When a VHE γ-ray is incident upon the atmosphere fast moving particles are created which generate a brief pulse of Cherenkov light. This Cherenkov light can be used by ground-based γ-ray telescopes in order to detect incident γ-rays. However, we see that hadronic cosmic rays also produce Cherenkov light and distinguishing γ-ray events above this background requires imaging the Cherenkov light pools. Often this imaging is done stereoscopically, i.e. with more than one tele-

scope in operation. This not only improves γ/hadron separation but also improves the source's localisation as photon arrival points can be triangulated between telescopes. This chapter concluded with a more detailed look at CTA.

Chapter 3 covered the physics necessary to this thesis of how particles are accelerated and emit radiation. This began with a discussion of diffusive shock acceleration, a mechanism thought to explain how particles are accelerated in AGN jets and how the particles acquire a power law energy spectrum. Then the Thomson cross section of the electron was derived and this was then used to explain how energetic electrons can upscatter photons into the γ-ray regime. Next we saw how cyclotron radiation is produced by charged particles in a B-field by treating the particles as quantum harmonic oscillators and this treatment was generalised to the synchrotron radiation produced when the source is moving at relativistic speeds. Finally, a brief discussion was given on how π particles could produce γ-rays through their decays.

Chapter 4 started with a discussion of the structure of AGN and the Unified Model, which explains how similar objects can appear very different in observations if viewed from different angles. We saw that if the density of low energy photons in the γ-ray emission region is too high then it would become opaque to γ-rays through pair absorption and this sets an upper limit on the size of the emission region. A lower limit can be inferred from the observed variability timescales of the γ-ray luminosity. These led to the conclusion that the emission region is probably on the order of 10^{-4} pc. Where this is located within the kpc scale jets is uncertain, but observations and modelling suggest that it is within about 200 pc of the central black hole. Different γ-ray emission mechanisms within AGN jets have been proposed. One common idea is that the energetic electron inverse Compton upscatter low energy photons into γ-rays. These low energy seed photons could be synchrotron emission from the electrons in the jet, known as the synchrotron self-Compton scenario. Upscattered seed photons from outside the jet, known as external Compton emission, could contribute or even dominate the γ-ray emission. Alternatively, we see that γ-ray emission from the jet could be the result of synchrotron radiation of hadronic protons and mesonic μ particles and the decay product of π particles.

In Chapter 5, the EBL was introduced. This is the diffuse light present throughout the universe. It is important to this thesis because γ-rays can pair produce with the EBL,

annihilating both photons. This means that the universe has an optical depth to γ-rays with IR-UV EBL photons dominating this process. However, we saw that there is some tension between the level of EBL inferred through modelling and the relatively small amount of absorption inferred in VHE γ-ray spectra. The hypothetical axion particle was then discussed as a solution to this problem: photons couple to axions in the presence of a B-field and so γ-rays could convert into axions or axion-like particles (ALPs) at the source and thereby cross intergalactic space unabsorbed before reconverting to γ-rays at the Milky Way.

In Chapter 6, a brief introduction was given to the use of information theory in model comparison. The AIC was introduced as a measure of how well a model describes a given set of data and an example was given applying this to LAT observations of the blazar 3C 273.

Chapters 7 and 8 covered 2 research projects into the spectral properties of bright LAT-detected blazars. In the first study, 9 FSRQ objects were studied and a mixture of log-parabolic (LP) and broken power law (BPL) spectra were found. The break energies were used to test the double-absorber model which posits that 2 breaks should appear in the γ-ray spectra if the emission region is within the radius of the broad-line region (BLR). This theory is disfavoured in this work as the cause of the breaks due to the energy and stability of the breaks not matching predictions. The second study made use of an extended sample of both FSRQ and BL Lac type objects. It concluded that LP is an adequate description of almost all objects in the sample and BPL fits appeared to be caused by confusion with nearby sources. This conclusion is in contrast to the previous study, and after further investigation it was concluded that the discrepancy is due to updating the instrument response function between the studies. This suggests that several previously published works concluding that blazars have BPL spectra may be in error. A light curve analysis was also performed for the bright FSRQ 3C 454.3. In its quiescent state, this object appears to have a stable spectrum well-described by an LP. When in high flux states, the spectrum was sometimes well-described by an LP and sometimes by a BPL. Again, the double-absorber model was disfavoured as the cause of the breaks, constraining the emission region to be outside of the BLR. From the change in spectral parameters it was concluded that the high flux states are caused by an increase in the Lorentz factor of the emission region (in an SSC scenario) or by changes in the

population of electrons in the emission region (in either an EC or an SSC scenario). As the LAT continues to collect more data and observe more high flux states, the prospect of pinning down the exact emission mechanism becomes a plausible goal. As we saw, the choice of IRF can potentially alter the spectral shape inferred; the release of the Pass 8 IRF at some point in the future may alter or confirm the current conclusions depending on how well results agree with those of the current Pass 7 IRF.

Finally, in Chapter 9, a study was presented in photon-ALP mixing within AGN jets. The effect that such mixing would have on the emitted γ-ray spectrum was calculated. It was seen that in the right conditions a sudden jump in flux at a few TeV could occur. The prospects for detecting the effects of ALPs with CTA were calculated through simulated observations. As well as the emitted spectrum being altered by mixing with ALPS, absorption of γ-rays by the EBL would be expected to be mitigated, as seen in Chapter 5. It was concluded that CTA will have a good chance to either observe the effects of ALPS or to set limits on the allowed mass and coupling constant of ALPs. PKS 2155-304 was shown to be a particularly promising target which means a strategy of observing nearby, bright objects with good photon statistics should be considered as well as observing more distant, hard-spectrum sources (where the distance means that EBL absorption is stronger and any mitigation potentially more apparent). CTA is set to dominate γ-ray astronomy for the coming decades and the instrument is hoped to bring in many important results. It is particularly exciting to look forward to the contribution of CTA to fundamental physics through the study of photon-ALP mixing within astrophysical sources.

Bibliography

[1] A. A. Abdo et al. Early *FERMI* gamma-ray space telescope observations of the quasar 3C 454.3. *ApJ*, 699:817–823, 2009.

[2] A. A. Abdo et al. *Fermi*/Large Area telescope bright gamma-ray source list. *ApJS*, 183:46–66, 2009.

[3] A. A. Abdo et al. The Fermi high-lattitude survey: Source count distributions and the origin of the extragalactic diffuse background. *ApJ*, 720:435–453, 2010.

[4] A. A. Abdo et al. Fermi Large Aea Telescope first source catalog. *ApJS*, 188:405–436, 2010.

[5] A. A. Abdo et al. The spectral energy distribution of Fermi bright blazars. *ApJ*, 716:30–70, 2010.

[6] A. A. Abdo et al. Spectral properties of bright Fermi-detected blazars in the gamma-ray band. *ApJ*, 710:1271–1285, 2010.

[7] A. A. Abdo et al. The second Fermi Large Area Telescope catalog of gamma-ray pulsars. *ApJS*, 208:17–78, 2013.

[8] A. Abramowski et al. VHE gamma-ray emission of PKS 2155-304: spectral and temporal variability. *A&A*, 520:A83, 2010.

[9] V. A. Acciari et al. Radio imaging of the Very-High-Energy gamma-ray emission region in the central engine of a radio galaxy. *Science*, 325:444–448, 2009.

[10] F. Acero et al. PKS 2005-489 at VHE: four years of monitoring with HESS and simultaneous multi-wavelength observations. *A&A*, 511:A52, 2010.

[11] B. S. Acharya et al. Introducing the CTA concept. *Astroparticle Physics*, 43:3–18, 2013.

[12] A. Achterberg et al. First year performance of the IceCube neutrino telescope. *Astroparticle Physics*, 26:155–173, 2006.

[13] A. Ackermann et al. The imprint of the extragalactic background light in the gamma-ray spectra of blazars. *Science*, 338:1190–1192, 2012.

[14] M. Ackermann et al. The Fermi Large Area Telescope on orbit: Event classification, instrument response functions, and calibration. *ApJS*, 203:4–74, 2012.

[15] R. Aggarwal and A. Caldwell. Error bars for distributions of numbers of events. *European Physical Journal Plus*, 127:1–8, 2012.

[16] C. Agostinelli and M. Markatou. Test of hypotheses based on the weighted likelihood methodology. *Statistica Sinica*, 11:499–514, 2001.

[17] F. Aharonian. TeV gamma rays from BL Lac objects due to synchrotron radiation of extremely high energy protons. *New Astronomy*, 5:377–395, 2000.

[18] F. Aharonian et al. The energy spectrum of TeV gamma rays from the Crab nebula as measured by the HEGRA system of Imaging Air Cerenkov Telescopes. *ApJ*, 539:317–324, 2000.

[19] F. Aharonian et al. Evidence for TeV gamma ray emission from cassiopeia a. *A&A*, 370:112–120, 2001.

[20] F. Aharonian et al. Is the giant radio galaxy M87 a TeV gamma-ray emitter? *A&A*, 403:L1–L5, 2003.

[21] F. Aharonian et al. A low level of extragalactic background light as revealed by γ-rays from blazars. *Nature*, 440:1018–2021, 2006.

[22] F. Aharonian et al. Observations of the Crab nebular with HESS. *A&A*, 457:899–915, 2006.

[23] F. Aharonian et al. Detection of VHE gamma-ray emission from the distant blazar 1ES 1101-232 with HESS and broadband characterisation. *A&A*, 470:475–489, 2007.

[24] W. Aharonian et al. Comparison of techniques to reconstruct VHE gamma-ray showers from multiple stereoscopic Cherenkov images. *Astroparticle Physics*, 12:135–143, 1999.

[25] H. Akaike. Information theory and an extension of the maximum likelihood principle. *Second international symposium on information theory*, pages 267–281, 1973.

[26] S. Andriamonje. An improved limit on the axion photon coupling from the CAST experiment. *JCAP*, 04(2007):10, 2007.

[27] A. De Angelis, O. Mansutti, M. Persic, and M. Roncadelli. Photon propagation and the VHE gamma-ray spectra of blazars: how transparent is really the universe? *MNRAS*, 394:L21–L25, 2009.

[28] A. De Angelis, O. Mansutti, and M. Roncadelli. Axion-like particles, cosmic magnetic fields and gamma-ray astrophysics. *Phys Lett B*, 659:847–855, 2008.

[29] T. Arlen et al. Rapid TeV gamma-ray flaring of BL Lacertae. *ApJ*, 762:92–105, 2013.

[30] A. M. Atoyan and C. D. Dermer. Neutral beams from blazar jets. *ApJ*, 586:79–96, 2003.

[31] A. M. Atoyan and C. D. Dermer. Neutrinos and gamma-rays of hadronic origin from AGN jets. *New Astronomy Reviews*, 48:381–386, 2004.

[32] W. B. Atwood et al. The Large Area Telescope on the Fermi gamma-ray space telescope mission. *ApJ*, 697:1071–1102, 2009.

[33] M. V. Barkov, F. A. Aharonian, S. V. Bogovalov, S. R. Kelner, and D. Khangulyan. Rapid TeV variability in blazars as a result of jet-star interaction. *ApJ*, 749:119–134, 2012.

[34] A. R. Bell. The acceleration of cosmic rays in shock fronts i. *MNRAS*, 182:147–156, 1978.

[35] J. M. Benade. Cosmic ray expedition to south-eastern Ladakh. *Urusvati Journal*, 3:17–20, 1933.

[36] K. Bernlöhr et al. Monte Carlo design studies for the Cherenkov Telescope Array. *Astroparticle Physics*, 43:171–188, 2013.

[37] R. D. Blandford and A. Königl. Relatavistic jets as compact radio sources. *ApJ*, 232:34–48, 1979.

[38] G. R. Blumenthal and R. J. Gould. The acceleration of cosmic rays in shock fronts I. *Reviews of Modern Physics*, 42:237–270, 1970.

[39] K. M. Blundell and S. Rawlings. The optically powerful quasar E1821+643 is associated with a 300 kiloparsec-scale FR i radio structure. *ApJ*, 562:L5–L8, 2001.

[40] M. Böttcher. The synchrotron peak shift during high-energy flares of blazars. *ApJ*, 515:L21–L24, 1999.

[41] M. Böttcher. Models for the spectral energy distributions and variability of blazars. *arXiv*, 1006.5048v1, 2010.

[42] A. H. Bridle, D. H. Gough, C. J. Lonsdale, J. O. Burns, and R. A. Lang. Deep VLA imaging of twelve extended 3CR quasars. *ApJ*, 108:766–820, 1994.

[43] A. M. Brown. Locating the gamma-ray emission region of the flat spectrum radio quasar PKS 1510-089. *MNRAS*, 431:823–835, 2013.

[44] P. Brun and D. Wouters. Reply to comment on "Irregularity in gamma ray source spectra as a signature of axionlike particles". *arXiv*, 1305:4098v1, 2013.

[45] C. G. Callan, R. F. Dashen, and D. J. Gross. The structure of the gauge theory vacuum. *Physics Letters*, 63B:334–340, 1976.

[46] J.-M. Casandjian and I. A. Grenier. A revised catalogue of EGRET gamma-ray sources. *Astronomy & Astrophysics*, 489:849–883, 2008.

[47] M. Cerruti, C. D. Dermer, B. Lott, C. Boisson, and A. Zech. Gamma-ray blazars near equipartition and the origin of the GeV spectral break in 3C 454.3. *ApJ*, 771:L4–L8, 2013.

[48] P.M. Chadwick et al. PKS 2155-304 - a source of vhe gamma-rays. *Astroparticle Physics*, 11:145–148, 1999.

[49] C. C. Cheung, D. E. Harris, and Ł. Stawarz. Superluminal radio features in the M87 jet and the site of flaring TeV gamma-ray emission. *ApJ*, 663:L65–L68, 2007.

[50] P. Colin et al. Performance of the MAGIC telescopes in stereoscopic mode. *Proceedings of 31st ICRC*, 2009.

[51] A. H. Compton. What is light? *Journal oF Chemical Education*, 7:2769–2787, 1930.

[52] A. H. Compton. An attempt to analyse cosmic rays. *Proceedings of the Physical Society*, 47:747–773, 1935.

[53] C. D. Dermer, J. D. Finke, H. Krug, and M. Böttcher. Gamma-ray studies of blazars: Synchro-Compton analysis of flat spectrum radio quasars. *ApJ*, 692:32–46, 2009.

[54] A. Domínguez et al. Extragalactic background light inferred from AEGIS galaxy-SED-type fractions. *MNRAS*, 410:2556–2678, 2011.

[55] E. Dwek and R. G. Ardent. A tentative detection of the cosmic infrared background at 3.5 micrometers from *Cobe*/DIRBE observations. *ApJ*, 508:L9–L12, 1998.

[56] E. Dwek and F. Krennrich. The extragalactic background light and the gamma-ray opacity of the universe. *Astroparticle Physics*, 43:112 – 133, 2013.

[57] M. Elitzur. On the unification of Active Galactic Nuclei. *ApJ*, 747:L33–L35, 2012.

[58] A. Eungwanichayapant and F. Aharonian. Very High Energy gamma rays from $e^{\pm}$ pair halos. *International Journal of Modern Physics D*, 18:911–927, 2009.

[59] A. S. Eve. On the radioactive matter in the earth and the atmosphere. *Philisophical Magazine*, 12:189–200, 1906.

[60] D. J. Fegan. Gamma/hadron seperation at TeV energies. *J. Phys. G.*, 23:1013–1060, 1997.

[61] J. D. Finke, S. Razzaque, and C. D. Dermer. Modeling the extragalactic background light from stars and dust. *ApJs*, 712:238–249, 2010.

[62] G. Fossati, L. Maraschi, A. Celotti, A. Comastri, and G. Ghisellini. A unifying view of the spectral energy distributions of blazars. *MNRAS*, 299:433–448, 1998.

[63] A. Franceschini, G. Rodighiero, and M. Vaccari. Extragalactic optical-infrared background radiation, its time evolution and the cosmic photon-photon opacity. *A&A*, 487:837–852, 2008.

[64] W. Galbraith and J. V. Jelley. Light pulses from the night sky associated with cosmic rays. *Nature*, 171:349–350, 1953.

[65] A. K. Ganguly, P. Jain, and S. Mandal. Photon and axion oscillation in a magnetized medium: A general treatment. *Phys Rev D*, 79:11501, 2009.

[66] N. M. Gerasimova, A. I. Nikishov, and I. L. Rosenthal. Interation of nuclei and photons of high energies with a thermal radiation in the universe. *Journal of the Physical Society of Japan.*, 17:Suppl. A–III, 1962.

[67] G. Ghisellini. Radiative processes in high energy astrophysics. *arXiv*, 1202.5949, 2012.

[68] G. Ghisellini et al. General physical properties of bright Fermi blazars. *MNRAS*, 402:497–518, 2010.

[69] G. Ghisellini, F. Tavecchio, and M. Chiaberge. Structured jets in TeV BL Lac objects and radiogalaxies. *A&A*, 432:401–410, 2009.

[70] D. Giannios, D. A. Uzdensky, and M. C. Begelman. Fast TeV variability in blazars: jets in a jet. *MNRAS*, 395:L29–33, 2009.

[71] P. Giommi et al. A simplified view of blazars: clearing the for around long-standing selection effects. *MNRAS*, 420:2899–2911, 2012.

[72] A. Gockell. Luftelektrische messungen bei einer ballonfahrt. *Bulletin de la Société Fribourgeoise des Sciences Naturelles*, 19:20–28, 1911.

[73] D. Griffiths. *Introduction to Elementary Particles*. John Wiley and Sons, 1987.

[74] M. J. Hardcastle. Jets, plumes and hotspots in the wide-angle tail source 3C 130. *MNRAS*, 298:569–576, 1998.

[75] R. C. Hartman et al. The third catalog of High-Energy gamma-ray sources. *ApJS*, 123:79–202, 1999.

[76] M. G. Hauser and E. Dwek. The cosmic infrared background: Measurements and implications. *Ann Rev of Astron and Astrophys*, 39:249–307, 2001.

[77] K. A. Hochmuth and G. Sigl. Effects of axion-photon mixing on gamma-ray spectra from magnetized astrophysical sources. *Phys Rev D*, 76:123011, 2007.

[78] J. Holder et al. Status of the VERITAS observatory. *AIP Conf. Proceedings*, 1085:657–660, 2008.

[79] D. Horns et al. Hardening of TeV gamma spectrum of active galactic nuclei in galaxy clusters by conversions of photons into axionlike particles. *Phys Rev D*, 86:075024, 2012.

[80] D. Horns and M. Meyer. Indications for a pair-production anomaly from the propagation of VHE gamma-rays. *JCAP*, 02(2012):33, 2012.

[81] W.-Y. P. Hwang and B-Q. Ma. Neutrons and antiprotons in ultrahigh-energy cosmic rays. *The European Physical Journal A*, 25:467–471, 2005.

[82] R. Jansson and G. R. Farrar. A new model of the galactic magnetic field. *ApJ*, 757:14–26, 2012.

[83] M. H. Jones and R .J. A. Lambourne, editors. *An Introduction to Galaxies and Cosmology*. Cambridge University Press, 2003.

[84] S. Kaspi et al. Measurement of the broad line region in two bright quasars. *ApJ*, 471:L75–L78, 1996.

[85] K. Katarzyński. Hard MeV-GeV spectra of blazars. *A&A*, 537:A47, 2011.

[86] K. Katarzyński, H. Sol, and A. Kus. The multifrequency emission of Mrk 501. from radio to TeV gamma-rays. *A&A*, 367:809–825, 2001.

[87] O. Klein and Y. Nishina. Simplified formulae of quantum cyclotron radiation. *The Oskar Klein Memorial Lectures*, 2:113–129, 1994.

[88] T. M. Kneiske and H. Dole. A lower-limit flux for the extragalactic background light. *A&A*, 515:A19, 2010.

[89] T. M. Kneiske, K. Mannheim, and D. H. Hartmann. Implications of cosmological gamma-ray absorption I. Evolution of the metagalactic radiation field. *A&A*, 386:1–11, 2002.

[90] A. A. Komar, editor. *Classical and Quantum Effects in Electrodynamics*. Nova Science Publishers, 1988.

[91] F. Krayzel et al. Improved sensitivity of H.E.S.S.-II through the fifth telescope focus system. *arXiv*, 1307.6461, 2013.

[92] S. Kullback and R. A. Leibler. On information and sufficiency. *Annals of Mathematical Statistics*, 22:79–86, 1951.

[93] A. Laor, F. Fiore, M. Elvis, B. J. Wilkes, and J. C. McDowell. The soft X-ray properties of a complete sample of optically selected quasars II. final results. *ApJ*, 477:93–113, 1997.

[94] E. Lefa, F. M. Riegger, and F. Aharonian. Formation of very hard gamma-ray spectra of blazars in leptonic models. *ApJ*, 740:64–73, 2011.

[95] J.-P. Lenain. *PhD Thesis*. PhD thesis, Observatoire de Paris, Meudon, 2002.

[96] F. Lewis, A. Butler, and L. Gilbert. A unified approach to model selection using the likelihood ratio test. *Methods in Ecology and Evolution*, 2:155–162, 2011.

[97] M. L. Lister et al. Gamma-ray and parsec-scale jet properties of a complete sample of blazars from the Mojave program. *ApJ*, 742:27–62, 2011.

[98] D Lynden-Bell. Galactic nuclei as collapsed old quasars. *Nature*, 223:690–694, 1969.

[99] Y. Lyubarsky. A new mechanism for dissipation of alternating fields in Poynting-dominated outflows. *ApJ*, 725:L234–L238, 2010.

[100] R. MacKenzie. Path integral methods and applications. *arXiv*, quant-ph/00004090v1, 2000.

[101] E. Massaro, M. Perri, P. Giommi, and R. Nesci. Log-parabolic spectra and particle acceleration in the BL Lac object Mkn 421: Spectral analysis of the complete BeppoSAX wide band X-ray data set. *A&A*, 413:489–503, 2004.

[102] A. Mastichiadis and J. G. Kirk. Variability in the synchrotron self-compton model of blazar emission. *A&A*, 320:19–25, 1997.

[103] J. E. McEnery et al. Scientific implications of the modified observing strategy of the Fermi Gamma-ray Space Telescope. *AAS Meeting*, 224:149.16, 20.

[104] C. Meegan et al. The Fermi Gamma-Ray Burst Monitor. *ApJ*, 702:791–804, 2009.

[105] O. Mena and S. Razzaque. Hints of an axion-like particle mixing in the GeV gamma-ray blazar data? *JCAP*, 11:023, 2013.

[106] M. Meyer, M. Raue, D. Mazin, and D. Horns. Limits on the extragalactic background light in the *Fermi* era. *A&A*, 542:A59, 2012.

[107] R. A. Millikan. High frequency rays of cosmic origin. *Proc. N.A.S.*, 12:48–55, 1926.

[108] A Mücke and M. Pohl. On the contribution of unresolved blazars to the extragalactic gamma ray background. *ASP Conference Series: BL Lac Phenomenon*, 159:217–220, 1999.

[109] A Mücke and R. J. Protheroe. A proton synchrotron blazar model for flaring in Markarian 501. *Astroparticle Physics*, 15:121–136, 2001.

[110] A Mücke, R. J. Protheroe, R. Engel, J. P. Rachen, and T. Stanev. BL Lac objects in the synchrotron proton blazar model. *Astroparticle Physics*, 18:593–613, 2002.

[111] A Mücke, J. P. Rachen, R. Engel, R. J. Protheroe, and T. Stanev. Photohadronic processes in astrophysical environments. *Publ. Astron. Soc. Aust.*, 16:160–166, 1999.

[112] Y. I. Neshpor et al. Blazar 3C 66A: Another extragalactic source of ultra-high-energy gamma-ray photons. *Astronomy Letters*, 24:134–138, 1998.

[113] Y. I. Neshpor et al. BL Lac: A new ultrahigh-energy gamma-ray source. *Astronomy Reports*, 45:249–254, 2001.

[114] P. L. Nolan et al. Fermi Large Area Telescope second source catalog. *ApJS*, 199:31–77, 2012.

[115] M. R. Orr, F. Krennrich, and E. Dwek. Strong new constraints on the extragalactic background light in the near-to mid-infrared. *ApJ*, 733:77–93, 2011.

[116] S. P. O'Sullivan and D. C. Gabuzda. Magnetic field strength and spectral distribution of six parsec-scale active galactic nuclei jets. *MNRAS*, 400:26–42, 2009.

[117] R. M. Otis. *The Source of the Penetrating Radiation Found in the Earth's Atmosphere*. PhD thesis, Cal Tech, 1924.

[118] S. J. Otis. *PhD Thesis*. PhD thesis, Durham University, 2002.

[119] R. D. Peccei and H. R. Quinn. Constraints imposed by CP conservation in the presence of psuedoparticles. *Phys Rev D*, 16:1791–1797, 1977.

[120] R. D. Peccei and H. R. Quinn. CP conservation in the presence of pseudoparticles. *Phys Rev Lett*, 38:1440–1443, 1977.

[121] R. A. Perley, A. G. Willis, and J.S. Scott. The structure of radio jets in 3C449. *Nature*, 281:437–342, 1979.

[122] D. Petry et al. Multiwavelength observations of Markarian 501 during the 1997 high state. *ApJ*, 536:742–755, 2000.

[123] F. Di Pierro et al. Performance studies of the CTA observatory. *Proc. of 32nd Int. Cosmic Ray Conference.*, 2011.

[124] J. Poutanen and B. Stern. GeV breaks in blazars as a result of gamma-ray abosprtion within the broad-line region. *ApJ*, 717:L118–L121, 2010.

[125] G. D. Şentürk, M. Errando, M. Böttcher, and R. Mukherjee. Gamma-ray observational properties of TeV detected blazars. *ApJ*, 764:119–137, 2013.

[126] M. S. Pshirkov et al. Deriving the global structure of the galactic magnetic field from Faraday rotation measures of extragalactic sources. *ApJ*, 738:192–205, 2011.

[127] R. E. Pudritz, M. J. Hardcastle, and D. C. Gabuzda. Magnetic fields in astrophysical jets: From launch to termination. *Space Science Reviews*, 169:27–72, 2012.

[128] G. Raffelt and L. Stodolsky. Mixing of the photon with low-mass particles. *Phys Rev D*, 37:1237–1249, 1988.

[129] B. Rani, B. Lott, T. P. Krichbaum, L. Furhmann, and J. A. Zensus. Constraining the location of rapid gamma-ray flares in the flat spectrum radio quasar 3C 273. *A&A*, 557:A71, 2013.

[130] M. J. Rees. The M87 jet - internal shocks in a plasma beam. *MNRAS*, 184:61–65, 1978.

[131] M. Renaud et al. Supernova remnants and pulsar wind nebulae in the Cherenkov Telescope Array era. *Memorie della Societa Astronomica Italiana*, 72:726–730, 2011.

[132] A. Ringwald. Searching for axions and ALPs from string theory. *Journal of Physics: Conference Series*, 485:012013, 2014.

[133] S. Sahu, B. Zhang, and N. Fraija. Hadronic origin of TeV gamma rays and ultrahigh energy cosmic rays from Centaurus A. *Phys Rev D*, 85:043012, 2012.

[134] M. A. Sánchez-Conde et al. Hints of the existence of Axion-Like-Particles from the gamma-ray spectra of cosmological sources. *Phys Rev D*, 79:123511, 2009.

[135] J. D. Scargle, J. P. Norris, B. Jackson, and J. Chiang. Studies in astronomical time series analysis. VI. Bayesian block representations. *ApJ*, 764:167–192, 2013.

[136] R. Schlickeiser, M Böttcher, and U. Menzler. Combined synchrotron and nonlinear synchrotron self-compton cooling of relativistic electrons. *A&A*, 519:A9, 2010.

[137] P. Schneider, editor. *Extragalactic Astronomy and Cosmology*. Springer, 2006.

[138] C. E. Shannon. A mathematical theory of communication. *Bell System Technical Journal*, 27:379–423, 1948.

[139] M. Simet, D. Hooper, and P. Serpico. Milky way as a kiloparsec-scale axionscope. *Phys Rev D*, 77:063001, 2008.

[140] J. A. Simpson. Elemental and isotropic composition of the galactic cosmic rays. *Ann. Rev. Nucl. Part. Sci.*, 33:323–381, 1983.

[141] A. Sokolov, A. P. Marscher, and I. M. McHardy. Synchrotron self-compton model for rapid nonthermal flares in blazars with frequency dependent time lags. *ApJ*, 613:725–746, 2004.

[142] B. B. Srivastava. *Fundamentals of Nuclear Physics*. Rastogi Publications, 2006.

[143] Ł. Stawarz, M. Sikora, and M. Ostrowski. High-energy gamma rays from FR I jets. *ApJ*, 597:186–201, 2003.

[144] B. E. Stern and J. Poutanen. Variation in the gamma opacity by the He II Lyman continuum constrains the location of the gamma-ray emission region in the blazar 3C 454.3. *MNRAS*, 417:L11–L15, 2011.

[145] M. Tavani et al. The AGILE mission. *Astronomy and Astrophysics*, 502:995–1013, 2009.

[146] F. Tavecchio et al. Evidence for an axion-like particle from PKS 1222 + 216? *Phys Rev D*, 86:085036, 2012.

[147] F. Tavecchio et al. The far emission region of the gamma-ray blazar PKS B1424-418. *MNRAS*, 435:L24–L28, 2013.

[148] F. Tavecchio, G. Ghisellini, G. Ghirlanda, L. Costamante, and A. Franceschini. The hard TeV spectrum of 1ES 0229+200: new clues from *Swift*. *MNRAS*, 399:L59–L63, 2009.

[149] A. Tchekhovskoy, R. Narayan, and J. C. McKinney. Black hole spin and the radio loud/quiet dichotomy of Active Galactic Nuclei. *ApJ*, 711:50–63, 2010.

[150] A. Tramacere, E. Massaro, and A. M. Taylor. Stochastic acceleration and the evolution of spectral distributions in synchro-self-Compton sources: a self consistent modeling of blazar's flares. *ApJ*, 739:66–82, 2011.

[151] P. Ubertini et al. IBIS: The imager on-board INTEGRAL. *A&A*, 411:L131 – L139, 2003.

[152] A. Wald. Tests of statistical hypotheses concerning several parameters when the number of observations is large. *Second international symposium on information theory*, 54:426–482, 1943.

[153] S. Weinberg. New light boson. *Phys Rev Lett*, 40:223–226, 1978.

[154] D. G. Wentzel. Cosmic-ray propagation in the galaxy: Collective effects. *Annual Review of Astronomy and Astrophysics*, 12:71–96, 1974.

[155] F. Wilczek. Problem of strong P and T invariance in the presence of instantons. *Phys Rev Lett*, 40:279–282, 1978.

[156] D. Yan, H. Zend, and L. Zhang. Estimates of emission-region locations of Fermi flat-spectrum radio quasars. *PASJ*, 64:2933–2942, 2012.

[157] R. Yan and M. R. Blanton. Are LINERs AGN? *American Astronomical Society Meeting*, 219:403.7, 2012.

[158] J. You, J. Chen, J. Deng, and Y. Xu. Simplified formulae of quantum cyclotron radiation. *Physics Letters A*, 232:376–372, 1997.

[159] M. Zacharias and R. Schlickeiser. Synchrotron lightcurves of blazars in a time-dependent synchrotron-self compton cooling scenario. *ApJ*, 777:109–110, 2013.